Analytical and Numerical Studies of Dark Matter Halos

A THESIS
SUBMITTED TO THE FACULTY OF THE GRADUATE SCHOOL
OF THE UNIVERSITY OF MINNESOTA
BY

Crystal Gayle Austin

IN PARTIAL FULFILLMENT OF THE REQUIREMENTS
FOR THE DEGREE OF
Doctor Of Philosophy

December, 2008

Analytical and Numerical Studies of Dark Matter Halos

by Crystal Gayle Austin

ABSTRACT

This dissertation focuses on the evolution and structure of dark matter halos of galaxies, groups and clusters of galaxies. I explore the dependence of the final halo's properties on the initial conditions and the physical processes that guide the halo to equilibrium, with special focus on the power-law nature of the ρ/σ^3 profile, where ρ is the density profile and σ is the velocity dispersion profile. As the astronomy community does not yet fully understand these processes, this research expands our understanding of collisionless, gravitationally-interacting systems.

In the initial chapters, I study the collisionless semi-analytic halo simulations and show that the final properties are sensitive to the initial conditions, such as the power-spectra filtering scale, the secondary velocities' magnitudes and directions, and the accretion rate. The general conclusions are that semi-analytic halos are in hydrostatic equilibrium and have a power-law ρ/σ^3 profile. If there were discontinuities in the initial conditions, the power-law feature in ρ/σ^3 breaks. Because of this, hydrostatic equilibrium is a less restrictive condition than the ρ/σ^3 profile. These halos can recover from moderate discontinuities by either correcting a single profile by sacrificing other quantities or by sufficient post-accretion.

Finally, I compare collisionless semi-analytic and N-body simulations directly. This novel comparison is useful because these techniques use different physics to collapse the proto-halo. The physical differences between these two methods are used to determine causes of the final halo profiles. Specifically, I find the NFW density profile and power-law ρ/σ^3 are due to the slow rate of evolution, which is determined from the initial conditions and cosmology. The density slope-velocity anisotropy relationship is dependent, rather, on the physical processes (notably the radial orbit instability) and three-dimensional evolution used to collapse the proto-halos. We also find that the slow-evolution halos do not undergo violent relaxation (large changes in the global

potential). Thus we suggest that slow, collisionless relaxation is responsible for creating the power-law feature ρ/σ^3.

Acknowledgements

I would like to thank the following people:

1. Dr. Liliya L. R. Williams, my adviser, for her patient guidance in the past six years. This project would not have been possible without her help.

2. Dr. Eric Barnes for all of the times we spent talking research in Liliya's office until dark and for all the guidance in the right direction.

3. My University of Washington collaborators, Jillian (Meyer) Bellovary, Dr. Greg Stinson, Dr. Julianne Dalcanton, and Dr. Tom Quinn for teaching me N-body coding. Without your help, I would have had to alter my thesis topic.

4. My mother, Genevieve D. Austin, and my fiancé, Jason E. Pierce, for an enormous amount of personal support and encouragement to finish my dissertation.

5. Kisha Delain, Jessica Ennis, Becky Adamski, Dr. John Martin, Dr. Pearl Sandick, Shea Brown, Tea Temim, and Martha Boyer for keeping me sane during the "best years of my life."

6. Dr. Arif Babul and Dr. Eduard Salvador-Sole for collaboration and discussion on my research.

7. Dr. Roberta Humphreys who recommended (while I was an undergrad) that I pursue graduate school in astronomy, as I wasn't too excited about physics graduate school.

8. The NSF grant AST 03-07604 and the University of Minnesota Doctoral Dissertation Fellowship for supporting this research.

"Non est ad astra mollis e terris via." Seneca the Younger

Contents

List of Tables

List of Figures

Chapter 1

Introduction

To the uninitiated, cosmology is the study of the observable universe. Thanks to many experiments and observations, we understand a great deal about our universe. We know that our universe is currently expanding at an accelerating rate, that there is leftover radiation from the beginning of the universe, and that the primordial elements were Hydrogen and Helium.

We have also determined the total amount of matter in the observable universe, as well as the amount of matter that we observe via electro-magnetic radiation – these two are not equal. The amount of mass we observe is approximately fifteen percent of what was predicted. The other 85 percent of that mass needs to exist – but we cannot see it. We call this mass 'dark matter'.

This dissertation focuses on the distribution and evolution of dark matter. This first chapter will give a basic overview, introduce the simulation techniques, and finally discuss the research goals.

1.1 Simulation techniques

When astronomers simulate the universe, they try to take into account all of the components in the universe (gas, stars, galaxies, dark matter, etc.). As each component adds complexity, some may be neglected. The components that will be simulated are arranged to mimic the early universe (via theory). This initial distribution is then

evolved to the present day via physical laws. These results are compared to our observations; if the simulation results agree with observations, our initial distribution is a possible reality. If it does not reproduce our observations, we try again with different initial distributions or include different physical processes.

As technology improves, the level of physical complexity and resolution in the simulations increase. We are not yet at the point where all the physical components (stars, gas, and dark matter) and physical processes (gravity, gas dynamics, metal feedback from dying stars, etc.) are evolved synchronously. Many of these have to be approximated by simple scaling laws or neglected. These simulations yield results that are able to reproduce many (but not all) of our observations.

These thorough simulations are very complicated and computer intensive. As the interest here is in the motions and proprieties of the dark matter, the baryonic matter and related processes can be neglected. Simulating only dark matter is simpler: it does not interact with the electro-magnetic force, does not interact with other particles of dark matter, or condense. Neglecting baryonic matter and its processes is not a terrible estimation. Dark matter only interacts via gravity, and most of the gravitational matter is dark, 85%.

Additionally, I am only interested in studying the regions of collapsed dark matter. These collapsed halos are no longer in touch with the larger cosmological picture and instead obey non-linear processes while relaxing into a steady state. My dark matter simulations will not simulate large pieces of the universe; I will only create individual halos.

Despite these simplifications, dark matter is problematic because we cannot observe it directly. In order to verify our simulation results, we need to observe its effects on normal, baryonic matter. Chapter 2 discusses the challenges of inferring dark matter properties from baryons and outlines the relevant results.

This research only simulates dark matter; there are no stars or gas. Therefore, the following sections in this chapter will focus on the results and techniques of dark matter simulations. These simulations produce large, diffuse clumps of matter of various sizes. Inside this halo is where stars, galaxies, groups of galaxies, and/or clusters of galaxies would form.

1.1.1 *N*-body Simulations

N-body simulations use a number of particles to represent the dark matter in the universe. The particles are placed so that they reproduce the early-universe's mass distribution. This distribution is based on a power-spectrum, $P(k)$, which is a Harrison-Zeldovich spectrum (Section 4.4) processed with a transfer function, which accounts for the evolution of fluctuations through the epoch of matter-radiation equality. The amplitude of $P(k)$ at these high redshifts is small, so typical amplitude of fractional density excess is much less than one. Particles then interact gravitationally with each other, forming bound structures of several particles. This reconstructs the hierarchical nature of structure formation and evolution (Shapiro et al., 204). The particles exchange energy and momentum through the changing global potential, as well as two-body encounters (even though such encounters are suppressed).

The large, bound structure is a dark matter halo. The center of the halo is determined and the density profile is calculated as a function of radius from the center. Velocity profiles, energy profiles, and momentum profiles are just a few that can be calculated. For all of the profiles discussed here, the profiles will be calculated using concentric spheres, even if the dark matter halo is not spherical.

In order to determine details about these halos, they must be resolved. This means that each halo needs to be made up of many particles so that they can be averaged, and thus create smooth, continuous profiles. Cosmological studies are content to have a halo resolved with several hundred particles, as they are more interested in the large scale distribution of halos. To study the internal dynamics and non-linear process of a single halo, 10,000+ are needed. For each of these particles, and at each time step, several calculations must be done to determine the net force. There are several programs able to do this; in this dissertation I use PKDGRAV. PKDGRAV is advantageous as it can adapt to a large range of particle densities as well as automatically reduce the time step for particles with short dynamical timescales (Stadel, 2001).

Gravity is calculated via multipole expansion, out to the fourth order. This is done because the multipole expansion gives a good approximation of the mass distribution

while being much more efficient than the typical particle-to-particle potential calculations.

$$\Phi = \int_V \gamma(|r|)\rho(r)dr = \sum_{n=0}^{\infty} \frac{1}{n!}[\frac{\partial^n}{\partial r^n}\gamma(r_{cm})]M^n \tag{1.1}$$

$$M^n = \sum_{i \in V} m_i x_i^n \tag{1.2}$$

Here M^n is the multiple of order n, calculated for all particles in the volume (Stadel, 2001). γ is the Green's function; for Newtonian gravity $\gamma = -1/r$ and Plummer softening has $\gamma = -1/(r^2 + \epsilon^2)^{\cdot 5}$. The recursion relations and required expansion techniques are located in Stadel (2001)

This is a tree code, meaning that it calculates the forces on many scales at each time step. Each step through the 'tree' corresponds to a smaller and smaller rectangular subdivision of the volume. The last step, known as 'leaves', may correspond to a volume with only a few particles (8 particles is optimal). The sub-divisions are calculated such that each cell requires the same number of calculations, making this code an ideal parallel code. Before each sub-division, the boundaries are squeezed inwards thus reducing the number of necessary leaves. This is illustrated in 1.1.

This is not a typical KD tree code, in that each box is only subdivided as many times as necessary for force accuracy. Therefore low density regions will not have as many leaves, and there are fewer calculations to perform.

The particles have been divided in a top-down manner; the force calculations are done bottom-up. For each leaf cell the center of mass and the reduced multipole moments are found. Moving one step higher in the tree, this cell's center of mass and multipole moments is calculated from its sub-cells.

The gravitational force is then calculated via 2 procedures: particle-particle for nearby mass or particle-cell calculations for more distant mass. The opening criterion, θ, defines the difference between the two regimes. A standard value is 0.55. If a cell is within $r(\theta)$ its multipoles cannot be used; its child cells are then considered. Once the level has been found (where a cell is not within $r(\theta)$) its multipoles are used to calculate the gravity due to that cell. If there is no such level, the gravitational interactions are calculated on a particle-particle basis.

PKDGRAV uses gravitational softening. This is done to reduce particle scatter

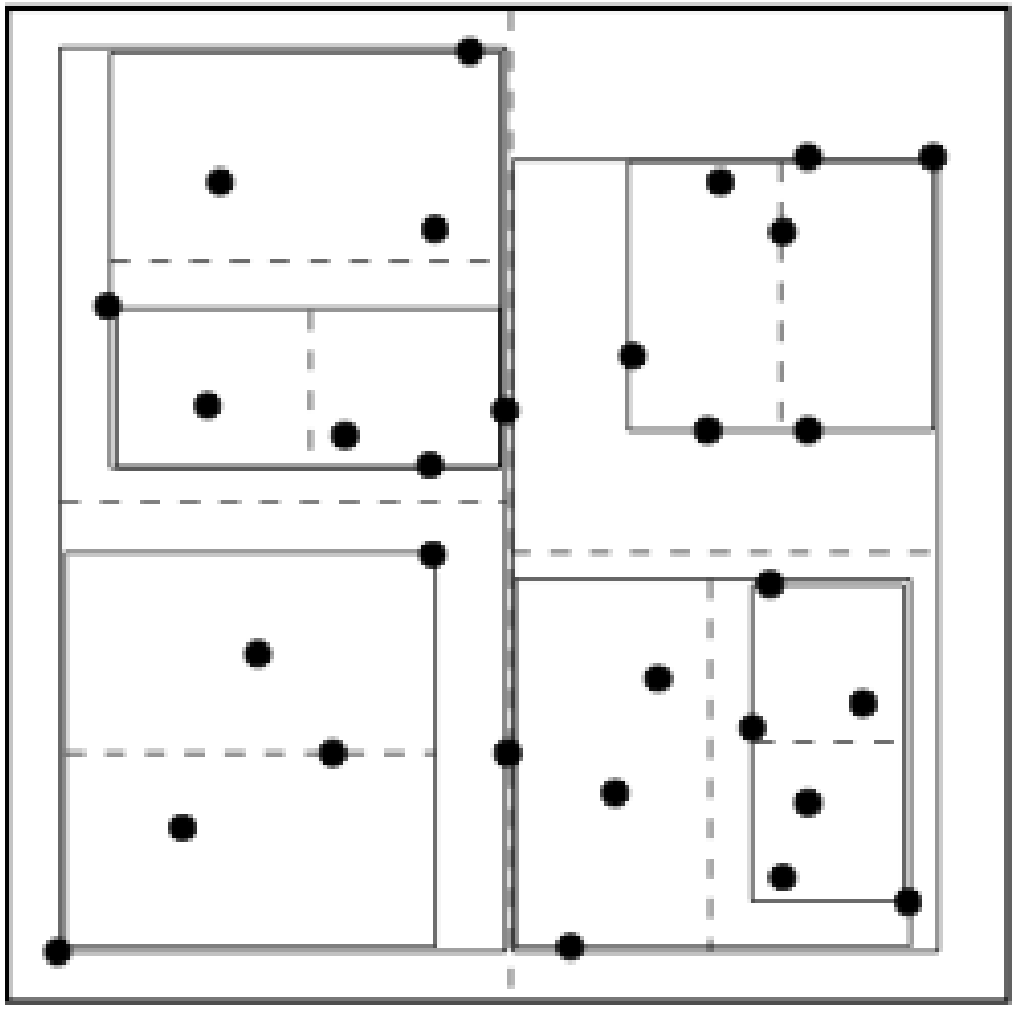

Figure 1.1: This figure is from Stadel (2001). It illustrates the sub-division process, creating the tree.

during close encounters. This is necessary when calculating dark matter, as the particles should be collisionless. PKDGRAV uses a spline softened gravity kernel so that gravity is Newtonian beyond 2ϵ; ϵ is the softening radius.

The time steps are also adaptive to increase computational efficiency. This is done because particles in high density regions have short dynamical timescales. The time step used to calculate forces needs to be shorter than this timescale to accurately describe its trajectory. However, the entire simulation is not highly dense and does not need the same time resolution.

Time steps are determined using the KDK method (kick-drift-kick). At each time step, the particles receive the acceleration based on the total gravitational force. They are then drifted: their new positions are calculated based on the particles' velocity and the length of the time step. If its drift exceeds the acceleration time step parameter, $\tau = 0.3 \cdot \epsilon^{1/2} a^{-1/2}$, its time step is reduced by half. Thus not all of the particles will have the same number of time steps; particles in higher density regions will experience more time steps.

Once the simulation has reached completion, the position and velocity of every particle is output. These are then analyzed using the TIPSY program. TIPSY locates the center of a potential well and creates profiles of physical quantities as a function of radius.

1.1.2 Semi-analytical Simulations, ESIM

Semi-analytic simulations are very different than *N*-body simulations. Rather than having each particle move independently in three-dimensional space, these simulations collapse concentric shells – each shell represents a specific amount of mass. At each time step, the new properties of the shell (peri-center, apo-center, angular momentum, and energy) are computed from the governing equations. They settle into the potential well and achieve equilibrium through violent relaxation. The method used here is based on Ryden & Gunn (1987), and was extended by Williams et al. (2004b); it is called ESIM: the Extended Secondary Infall Model. As we describe in section 3.2, these halos are not subject to the same processes and interactions as *N*-body halos. ESIM halos are spherically symmetric, with one spatial and two velocity (radial and tangential) phase-space dimensions. There are no mergers.

1.2 Dark Matter Density Profiles

Many separate *N*-body studies have found a 'universal' density profile (Cole & Lacey, 1996; Moore et al., 1999; Bullock et al., 2001; van den Bosch et al., 2002; Navarro et al., 2004; Dubinski & Carlberg, 1991; Navarro et al., 1997; Huss et al., 1999; Macmillan, 2006). This 'universal' profile (often called the NFW profile) is characterized as an inner slope of $d\log\rho/d\log r \sim -1$, which steepens to $\approx$ -3 beyond the virial radius. This universal profile is well described by the analytical equation

$$\frac{\rho(r)}{\rho_{crit}} = \frac{\delta_c}{(r/r_s)(1+r/r_s)^2} \tag{1.3}$$

(Navarro et al., 1997). Currently, some advocate this equation is the best description, while others find more merit in a fit suggested by Navarro et al. (2004):

$$ln\frac{\rho_\alpha}{\rho_{-2}} = \frac{-2}{\alpha}[(r/r_{-2})^\alpha - 1]. \tag{1.4}$$

The value of the central slope, and the nature of the transition between inner and outer slopes, is still a matter of debate. Regardless of which density profile expression proves to best describe *N*-body halos, the underlying physics that drive the halos to have this shape is not yet fully understood.

Several attempts have been made in the literature to explain the density profile shape. For example, Syer & White (1998) suggested that the NFW profile results from a series of repeated mergers: as the undigested cores of merging satellites accumulate at the center, the central r^{-1} cusp develops. However, Huss et al. (1999) performed simulations of isolated halos with varying degrees of thermal motion of dark matter particles. The final halos closely resembled the universal NFW shape, suggesting that hierarchical merging is not critical to the outcome. Moore et al. (1999) simulated halo formation using a matter power spectrum with suppressed small scale power. The final density profiles were still well described by the NFW fit. Some analytical studies suggest that secondary infall and accretion can determine the density profile shape (Avila-Rees et al., 1998). Barnes et al. (2005) argue that the density profile, and in particular its radially changing slope, is the result of a mild aspect of the radial orbit instability.

1.3 Dark Matter Velocity Dispersion Profiles

When we speak of the kinematic proprieties of the halo, we often use the velocity dispersion, σ, and the anisotropy parameter, β. These are spherically-averaged quantities as a function of radius. The velocity dispersion describes the spread in velocities and is defined as (Binney & Tremaine, 1987):

$$\sigma^2 = \overline{(v - \overline{v})^2} = \overline{v^2} - \overline{v}^2 \tag{1.5}$$

These velocities can be directed radially, tangentially, or at any intermediate state. We use the anisotropy parameter (Binney & Tremaine, 1987) to describe the amount of anisotropy:

$$\beta = 1 - \frac{\overline{v_\theta^2}}{\overline{v_r^2}}. \tag{1.6}$$

When $\beta = 1$, the velocities are radial; $\beta = -\infty$ indicates tangential orbits; and $\beta = 0$ describes isotropic orbits. Radially isotropic velocities indicate that the temperature (i.e. the average kinetic energy) is greater in the radial direction than in the tangential direction. Baryonic gas is expected to have isotropic velocities due to the large number of collisions experienced. Intra-cluster gas has a mean free path of several kpc, which is significantly smaller than a cluster (Hansen & Piffaretti, 2008). As dark matter is collisionless, it does not undergo these frequent and equipartitioning events.

Cole & Lacey (1996), Carlberg (1997), and Fukushige & Makino (2001) have shown that N-body dark matter halos are isotropic in the core and become radially biased as you approach the virial radius. Until recently, there had not been any observations to support this. Hansen & Piffaretti (2008) measured the X-ray profiles of two relaxed clusters so that HSE could be assumed. This allows for the derivation of the gas temperature profile and total density profile. These profiles are then used to derive the dark matter's radial velocity dispersion profile. The difference between this kinetic temperature and the gas temperature (in the outer, non-radiatively dominated halo) then gives the tangential kinetic temperature. With the radial and tangential dispersions calculated, the anisotropy is known. Hansen & Piffaretti (2008) found their two clusters to have $\beta > 0$ with 3σ confidence.

This method is young but will improve quickly. There are also plans to measure the

velocity anisotropy directly once WIMP detection is common. WIMPS are theorized to occasionally interact with baryonic matter; as of yet, there are no reliable detections. Host & Hansen (2007) show that when we are able to detect these interactions, we will see a greater detection rate in the direction of Earth's motion through the galaxy. The galactic dark matter's anisotropy will be a subtle effect superimposed on this large dipole. This is so subtle, however, that we would need to detect 10^6 events to determine β to an accuracy of 0.03.

In closing, measuring the dark matter velocity dispersion and anisotropy via using indirect methods is still novel. Direct measurement is still a hopeful goal for the future.

1.4 Dark Matter Coarse-Grained Phase-Space Density Profiles

The phase-space density (or the distribution function) is a six dimensional function that describes a particle's position and motion: $f(x, y, z, v_x, v_y, v_z)$. The motion of a particle through phase-space is described as a flow and is quantified by the collisionless Boltzmann equation (Binney & Tremaine, 1987):

$$\frac{\partial f}{\partial t} + \sum_{i=1}^{3}(v_i \frac{\partial f}{\partial x_i} - \frac{\partial \Phi}{\partial x_i}\frac{\partial f}{\partial v_i}) = 0 \tag{1.7}$$

The distribution function, f, is often called the fine-grained phase-space density, as it describes every particle's properties. The coarse-grained distribution function, $\overline{f}$, is an averaged quantity over a small volume; this does not satisfy the collisionless Boltzmann equation.

Equation 1.7 can be applied to non-spherical systems. However, when studying spherical systems, the quantity $\rho(r)/\sigma^3(r)$ is proportional to the coarse-grained phase-space density. ESIM halos are spherical, and ρ/σ^3 is the coarse-grained phase-space density. *N*-body halos, however, are not strictly spherical; the ρ/σ^3 will not be equivalent to the phase-space density. Taylor & Navarro (2001) measured this quantity for three *N*-body halos (circular velocities 160-200 $\mathrm{km\,s^{-1}}$) and found that it was well represented by a power-law fit (equation 1.8) over the majority of the halo, from $10^{-2.5}$ virial radii

to just beyond the virial radius.

$$\frac{\rho(r)}{\sigma^3(r)} \approx \frac{\rho_o}{\sigma_o^3}(\frac{r}{r_o})^\alpha \tag{1.8}$$

The power-law index α was found to be very similar for all the three halos: $\alpha = -1.875$. The presence of the power-law has been confirmed by Raisa et al. (2004), Ascasibar et al. (2004), and Dehnen & McLaughlin (2005), with slope values ranging from -1.84 to -1.95.

This finding was unexpected because the density profile, $\rho(r)$ undergoes a considerable slope change in the same radial interval. The scale-free nature of the phase-space density implies that the velocity dispersion changes in such a way as to offset the change in the density profile slope.

Given the 'universal' density fit to *N*-body halos and assuming that the halos are in equilibrium, one can calculate the phase-space density as a function of radius via the Jeans equation. Barnes et al. (2006) demonstrated that both the NFW (equation 1.3) and the N04 (equation 1.4) fits produce nearly scale-free phase-space density profiles for ~ 3 decades in radius, with a slope close to 1.9. They conclude that most *N*-body halos should have scale-free phase-space density profiles. Additionally, Barnes et al. (2006) demonstrated that the condition of hydrostatic equilibrium (where $\rho\sigma^2$ acts as a fluid pressure), as quantified by the Jeans equation, does not require ρ/σ^3 to be a power-law in radius.

The scale-free nature of ρ/σ^3 represents a novel way of looking at the properties of halos and, as such, should be explored further. If this property is universal, it is an unrecognized constraint on the shape of the density profiles and halo kinematics.

In this dissertation we address whether the scale-free nature of ρ/σ^3 is a result of initial conditions, an outcome of evolution and virialization, or a consequence of the final equilibrium state of halos.

1.5 Dark Matter Density Slope-Velocity Anisotropy Relationship

Despite all of this research, the community at large is only now beginning to understand the physical reasons for the ρ/σ^3 profile. Much of this understanding has come from studies of the Jeans equation (Austin et al., 2005; Taylor & Navarro, 2001; Hansen, 2004; Dehnen & McLaughlin, 2005). The steady state, spherical Jeans equation is given by Binney & Tremaine (1987):

$$\frac{d(\nu\overline{v_r^2})}{dr} + \frac{\nu}{r}[2\overline{v_r^2} - (\overline{v_r^2} + \overline{v_\phi^2})] = -\nu\frac{d\Phi}{dr}. \tag{1.9}$$

However, there are two relationships that need to be quantified before a solution can be determined: the coarse-grained phase-space density w.r.t. radius, $\rho(r)/\sigma(r)^3$, and the velocity anisotropy w.r.t. the density profile's slope, $\beta(\gamma)$.

Hansen & Moore (2004); Hansen et al. (2005) have quantified this latter relationship for several scenarios. They concluded that this relationship is linear and 'almost blind' to the specific initial conditions, as long as the halo is significantly perturbed and subsequently relaxed.

1.6 Conclusion

The dark matter is the dominant mass component in the universe. By using observations, we are beginning to learn more about the structure and kinematics of dark matter. However, directly detecting dark matter is still not possible. In the mean time, we use simulations to try to understand the non-linear collapse processes and predict what will be observed when it becomes possible.

These simulations are accomplished in a variety of ways, but the phenomenology of the final profiles (density, velocity, and coarse-grained phase-space density) are well described, yet we do not understand the physical processes that cause these features. The dynamical processes in question include violent relaxation, the radial orbit instability, dynamical friction, phase-mixing, or some other hitherto unidentified process.

In this dissertation, I will present simulations created with the ESIM semi-analytical

method and the PKDGRAV N-body code. The goal is to isolate and characterizing these cause-and-effect relationships in halo collapse. These two techniques – ESIM and N-body – evolve under different physical processes. As such, we are able to use the similarities and differences in the initial conditions and the physical processes operating during the collapse to determine how the final halo properties depended on these. We conclude that some final halo properties can be traced back to specific features of collapse; in other words, cause and effect are, to some degree, separable.

Chapter 2 presents a brief history of observations and discoveries relevant to dark matter. Chapters 3 and 4 explore semi-analytical simulations of dark matter with reference to the current understandings of others in the field. Chapter 5 then moves on to directly compare a semi-analytic simulation with a nearly identical numerical simulation.

Chapter 2

Galaxy Clusters

2.1 Introduction

Clusters of galaxies are the largest bound structures seen in the current universe. These typically contain on the order of 100 galaxies, and the total mass of the structure is greater than $10^{14} M_{\odot}$ (Bower et al., 2004). These structures are so large that they continue to gravitationally attract nearby galaxies, increasing the size of the cluster. Despite the large number of clusters that are cataloged, clusters are still rare objects. There is, on average, only one cluster in every 4900 Mpc^3 (Bower et al., 2004). As such, only 5 to 10% of all galaxies are located in clusters (Bower et al., 2004).

These large structures form by accreting galaxies and groups of galaxies. Groups have more than 5 bright galaxies and a total mass greater than $10^{13} M_{\odot}$ (Bower et al., 2004). There are also 'poor clusters' which generally have 20 to 50 galaxies. These different classifications are not well-defined, as the transition from groups to clusters is a gradual continuum.

As clusters accrete galaxies, they also accrete diffuse gas and form a relatively dense intra-cluster medium (ICM) between the galaxies. There is nearly 10 times more mass in the ICM than in all of the galaxies in the cluster (Bower et al., 2004). The ICM fills the cluster and is supported against gravity via gas pressure and magnetic pressure. As galaxies move through the cluster, the ICM exerts pressure, stripping the galaxies of their gas and adding to the content and metalicity of the ICM.

Clusters of galaxies contain more than just galaxies and ICM. The majority, about

85%, of the mass in clusters is in the form of dark matter. Dark matter refers to mass that does not interact with any force except gravity. We can only observe dark matter via its gravitational effects on the other cluster components. Dark matter is the dominant gravitational source, causing the galaxies' motions and ICM's properties to reflect the gravitational potential of the dark matter.

These 3 main components– galaxies, the ICM, and dark matter– exist together in the main body of the cluster. It is a loose distribution and, as such, has no well-defined spatial boundaries (Evrard, 2004). Yet, there is a canonical line that defines the edge of a cluster: the virial radius. This radius is defined where the average interior density is 200 times that of the critical density: $\rho_{crit} = 1.9 \cdot 10^{-29} \cdot h^2 \cdot g \cdot cm^{-3}$. Within the virial radius, it is assumed that the galaxies and dark matter obey the virial theorem. These galaxies and dark matter have developed orbits within the cluster, which are not strongly related to their histories prior to accretion. This is known as a relaxed state. Having a defined boundary at the virial radius allows for easier classification and analysis, but it does not indicate that the cluster ends abruptly at this point.

In the inner cluster, the galaxies undergo interactions, tidal forces, and mergers as they orbit the cluster's center. The ICM gas is supported against gravitational collapse via gas pressure and magnetic pressure but is also subject to large bulk motions and flows.

In the outer parts of the cluster, there is still material falling into the cluster. The smaller structures merge into larger structures; clusters are still in the process of forming (Section 2.5.2). This makes clusters of galaxies ideal for structure formation, kinematics, and relaxation studies. This also means that clusters are sensitive to cosmological parameters that affect structure formation such as σ_8 and Ω_M. σ_8 describes the amplitude of mass-fluctuations in 8 Mpc/h radius spheres, Ω_Λ describes the energy density in the cosmological constant, and Ω_M parametrizes the fraction of total mass with respect to closure density of the universe. As such, clusters of galaxies have the potential to be excellent tests for the cosmological models.

To use clusters as probes of cosmology, we first have to locate them. Clusters can be detected through optical richness in galaxy counts (Section 2.2.1), through X-ray detection of the ICM (Section 2.3.1), identifying prominent luminous red galaxies at the clusters center (Section 2.2.6), and through the Sunyaev Zel'dovich effect (Section

2.3.6)(Evrard, 2004). In this chapter, we will concentrate on the techniques of observing clusters as well as the constraints these observations have placed on the evolution of clusters.

2.2 Components and structure: Galaxies

The term 'cluster' was first used by Hubble and Humason in 1931, referring to the Virgo Cluster (seds.org, 2005), though the overdensities in galaxy population (then known as 'nebulae') were observed as early as 1781 by Charles Messier (seds.org, 2005). Since this discovery, large amounts of time has been spent searching the sky for large galaxy populations. Recent optical surveys of the sky have been successful in locating clusters.

2.2.1 Galaxy Surveys

Clusters are bright, large objects and as such are observable at large distances. Though, as galaxies and clusters are observed at larger distances, they appear fainter and become harder to detect. Due to the large distances to clusters and their movement with the Hubble expansion, astronomers often use redshift to describe these distances. Redshift, z, is defined as the relative change in the observed wavelength of light vs. the emitted wavelength: $1 + z = \lambda_{observed}/\lambda_{emitted}$. This change in the wavelength is due to the source moving with respect to the observer; in this case it is due to the expansion of the universe.

When we observe nearby galaxies, this effect is minimal and $z = 0$. However, if we look deeper into space at an object with a redshift of $z \sim 0.1$, the effect is more noticeable. Using an $H_o = 70$ and an $\Omega_M = 0.3$, this object would have a luminosity distance of $1.5 \cdot 10^9$ light years. An object with a redshift of $z \sim 1.0$ has a luminosity distance of $21.5 \cdot 10^9$ light years.

The surface brightness decreases as $(1 + z)^4$, placing a strong cutoff on the ability to observe dim galaxies at large distances (Rosati, 2004). In this paper, we will mainly be considering objects between $z = 0$ and $z = 1.5$.

The Two Degree Field survey (2dF) and the Sloan Digital Sky Survey (SDSS) have cataloged clusters and member galaxies in hopes of determining the spatial distribution of galaxies in clusters (Bower et al., 2004). Together, SDSS and 2dF have cataloged over

1000 luminous red galaxies and 10,000 galaxies in the range of redshift from 0.4 to 0.7 (Nichol, 2004). These projects have found clusters in many evolutionary stages, aiding the understanding of cluster formation, galaxy mergers and galaxy evolution (Bower et al., 2004).

2.2.2 The Sloan Digital Sky Survey

The Sloan Digital Sky survey is a multicolor and spectroscopic survey (Nichol, 2004). It is mostly a northern hemisphere project using a dedicated 2.5 m telescope in New Mexico. The project was designed to catalog 10^6 galaxies over a quarter of the celestial sphere (Nichol, 2004). The SDSS images the sky in 5 filters: u, g, r, i, and z allowing for 4 measurement of relative color. SDSS is capable of spectroscopy from 3700 to 9100 Å.

SDSS provides a three-dimensional image of the sky, with redshifts determined from the spectra. The unique SDSS searching algorithm looks for galaxies that are related in 7 dimensions: 3 space and 4 color. Each galaxy must lie within a range of right ascension, declination and redshift. Also, the galaxies must have similar colors in u-g, g-r, r-i, and i-z (Nichol, 2004). If a galaxy were closer (farther) than the cluster, it would appear bluer (redder) than the majority of the cluster members. Using the color to define a cluster in this way minimizes projection effects by limiting the number of foreground and background galaxies included in a cluster (Nichol, 2004). These restrictions automatically eliminate 80% of all detected galaxies resulting in a cluster catalog that is more than 90% complete with less than 10% contamination of field galaxies (Nichol, 2004).

Even with the 7-D SDSS algorithm for determining the members of a cluster, there are still galaxies that are included in the catalog that are actually members of the field (this is the less dense space between clusters and groups). This introduces a bias, as field galaxies and cluster galaxies evolve differently.

The maximum redshift for SDSS spectroscopic detection of large, luminous red galaxies (which are excellent traces of large-scale structure, Section 2.2.6) is $z = 0.45$ (Nichol, 2004); in a joint effort with the 2dF survey, this limit is pushed to $z \sim 0.7$. At this redshift, only the brightest galaxies are able to be detected. While this still provides information of the structure at $z = 0.45$, we only have information on a small

subset of the brightest and most massive members of the cluster's population resulting in a Malmquist bias. This effect may also select galaxies with certain star formation history. Galaxies that have had a recent decrease in star formation will also have a decrease in luminosity by up to one magnitude (Bower et al., 2004). This may increase the number of observed star forming galaxies w.r.t. the number of passively evolving systems, hence biasing the sample.

The SDSS catalog provides us with a large body of information, from which astronomers will be able to derive the galaxy morphology and color evolution. From these, we can derive the galaxies' star formation rate.

2.2.3 The Two Degree Field (2dF) survey

The 2dF survey is specifically targeted to observe the three-dimensional structure of the universe by determining the redshifts and positions for 120,000 galaxies (Couch et al., 2004). The survey is based at a 3.9 m Australian telescope and covers $188^{\square\circ}$ to a limiting magnitude of 19.45 (Couch et al., 2004).

The 2dF survey is able to detect galaxies from $z = 0$ to $z = 0.3$. This corresponds to a volume of $10^8 h^{-3} Mpc^3$ and allows structure observations up to scales of $400h^{-1}$ Mpc. Figure 2.1 shows a slice of the structure as measured by 2dF. The amount of clustering is statistically measured (using a two point correlation function and analysis of the power spectrum) confirming coherent collapse on large scales and determining $\Omega_M = 0.30 \pm 0.06$ (Couch et al., 2004).

2.2.4 Cluster Mass via the Dynamical Technique

The dynamical mass of a cluster can be derived using observations of member galaxies – galaxies' velocities are sensitive to the amount of mass interior to their position. By observing a sample of galaxies, the velocity dispersion (σ) can be determined. However, these measurements are done via Doppler technique, which only measures one velocity dimension: along our line of sight. As the natures of the orbits are unknown (tangential, radial, or isotropic), determining the full 3-dimensional velocity dispersion is not possible (Williams, 2003). If the orbits are assumed to be isotropic, the 1-D velocity dispersion is $\sqrt{1/3}$ that of the total velocity dispersion. The mass is then determined to be

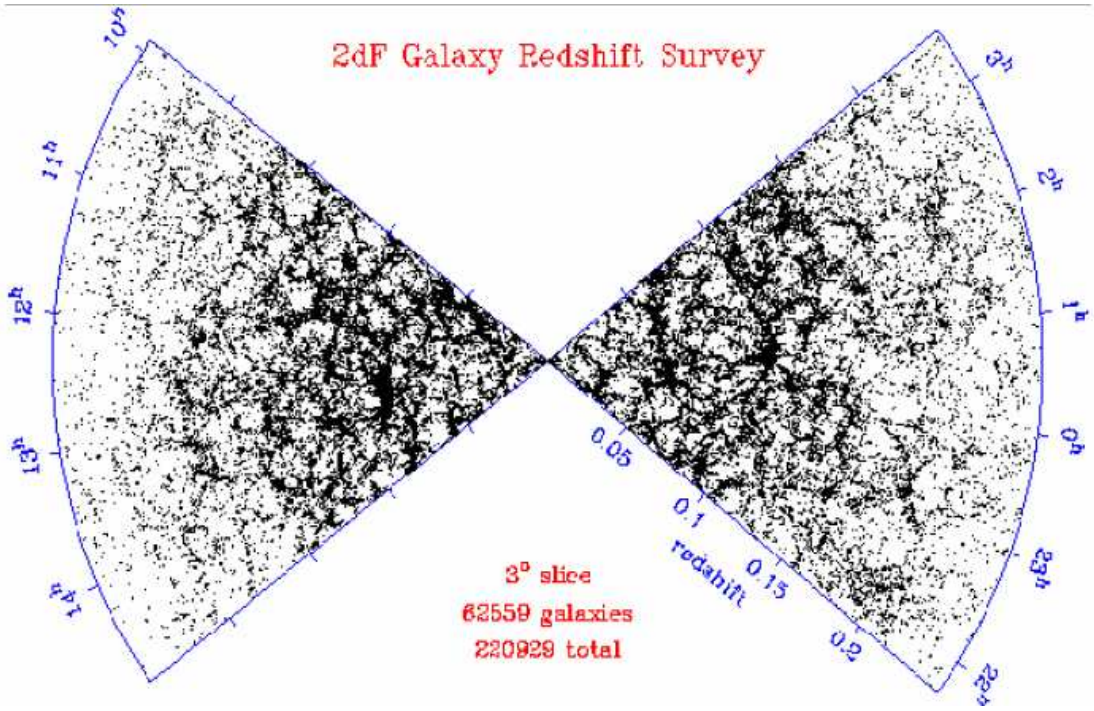

Figure 2.1: From Couch et al. (2004), a cone diagram based on a 3-degree slice taken through the NGP (left) and SGP (right) strips of the 2dFGRS. This shows the structure and clustering of galaxies to a redshift of $z = 0.3$.

$M = 3\sigma^2_{1-D} \cdot r \cdot G^{-1}$. This method estimates the total mass of the cluster to an accuracy of $\sim 50\%$; these errors are due to the difficulties in measuring the degree of velocity anisotropy.

2.2.5 The Red-Sequence technique: Identifying Member Galaxies

The red-sequence method takes advantage of the fact that most cluster galaxies have little current star formation, and their stellar populations are passively evolving (section 2.2.7). As their stellar populations age, the color becomes redder (Gladders, 2004) and the luminosity decreases ~ 1 magnitude from $z = 1$ to $z = 0$. Assuming the member galaxies formed at a similar time, the galaxies will display an identifiable color-magnitude structure (Gladders, 2004).

The red-sequence is a linear relationship in color (typically B-R) versus magnitude (R band). E+S0 galaxies (elliptical and lenticular galaxies) demonstrate this relationship. Foreground galaxies appear bluer (due to the difference in redshift) allowing these to be easily removed from the sample (Gladders, 2004). Background galaxies are, on average, fainter and may be removed from the sample. Using these photometric selections, a cluster's catalog contains only 5% contamination (Gladders, 2004). While this technique only contains 5% of unrelated galaxies, it also excludes related galaxies that may have been formed earlier or later, have a different morphological type, or otherwise have a different color than the main E+S0 population. As such, this method is useful for identifying clusters, but less reliable when studying the properties of cluster galaxies in general.

The location of the red-sequence is also dependent on the distance to the cluster. Distant clusters will be more redshifted, moving the red-sequence to higher values of B-R color. Treu (2004) have shown that more distant elliptical and lenticular galaxies also follow the red-sequence relationship to $z = 0.8$. Using this to study stellar populations at different redshifts (and different look-back times), conclusions about the star formation history can be drawn: clusters are dominated by passive stellar evolution with the last star formation burst at $z_{form} = 2$ (Treu, 2004).

2.2.6 Morphology of Cluster Galaxies

Field galaxies can form into any of the observed galaxy morphologies, depending on the local environment. About half of the field galaxies are spiral galaxies, while the other half are elliptical galaxies. However, morphology studies by SDSS and 2dF find that galaxies in clusters are almost completely elliptical or lenticular type galaxies.

There are two possible explanations for this. First, galaxies that are in clusters formed earlier, since they were located near a large overdensity of matter. Perhaps forming in a higher density region preferentially forms elliptical or lenticular morphologies (early-type galaxies). Second, perhaps the cluster galaxies became early-type galaxies as they were consumed by the cluster. Cluster galaxies are subjected to interactions with the ICM and neighboring galaxies; these processes may transform late-type spirals into the early-type ellipticals and lenticulars observed population.

Galaxies in several stages of accretion into a cluster are observed with 2dF and SDSS. As the galaxies enter the cluster, they show a variety of morphologies, including spirals. This implies that galaxies are formed as field galaxies and become early-type galaxies as they merge with the cluster. The second scenario seems to be correct: field and cluster galaxies were formed in a similar environment. As galaxies are accreted into a cluster, the process alters the morphology, creating this distinct population of galaxies (Dressler, 1980).

Specifically, observations of elliptical and lenticular galaxies (E+S0s) have been able to corroborate this. E+S0s are observed with SDSS at different radii from the center of the cluster. Central galaxies – in the higher density region – have fewer spiral galaxies. As you move towards the virial radius, the local density of galaxies continues to decrease, and there are more late-type galaxies.

This is known as the morphology-density relationship (Bower et al., 2004). The density of galaxies in the cluster core is, on average, 3 orders of magnitude higher than that in the field (Couch et al., 2004), increasing the rate of interactions and mergers. Each interaction has the potential to disrupt an organized galaxy (such as a late-type spiral); mergers preferentially form larger early-type galaxies.

This preferential and irreversible transition of morphology appears to happen relatively quickly as the galaxy begins to fall into a cluster. SDSS and 2dF have shown that this tends to happen near the viral radius. SDSS has determined a critical surface

density of $\Sigma = 1$ galaxy $\cdot h_{75}^{-2} \cdot Mpc^{-2}$ (Nichol, 2004). Also, 2dF has determined the critical density at which the star formation rate drops: $\rho = 1$ galaxy$\cdot Mpc^{-3}$ (Couch et al., 2004), thus reinforcing the model that a galaxy undergoes specific evolution as it enters a cluster.

Clusters also contain luminous red galaxies (LRG). LRGs appear to be excellent tracers of clusters and the large-scale structure in the universe (Nichol, 2004). These galaxies are dominated by their old, luminous stellar populations and are only found in highly-overdense regions. LRGs are among the oldest members of the cluster and are detectable to high redshift: $z \sim 0.7$. Their red stellar populations are passively evolving, and the mass implies several more mergers than the typical E+S0 galaxy. Nichol (2004) have found that the LRG correlation function is comparable for both groups and clusters: the amplitude and the scale lengths are similar. This makes these luminous galaxies ideal for the identification of clusters.

2.2.7 Star Formation in Cluster Galaxies

In addition to the morphology difference, we also see a difference in the star formation rates between field galaxies and cluster galaxies (Bower et al., 2004). Star formation rates (SFRs) in cluster galaxies are much lower than seen in the field. In part, this may be related to the morphology change as a galaxy falls into a cluster.

SDSS has observed that star formation (SF) within galaxies decreases as the local galaxy number surface density increases, independent of the morphology (Nichol, 2004). As these galaxies have varied histories, this observation indicates that the decrease in star formation is due to an interaction with the cluster's environment. Bower et al. (2004) showed that SF in clusters is suppressed by an order of magnitude w.r.t. the local field value of $1.6 \cdot 10^{-2} M_{\odot} \cdot yr^{-1} \cdot Mpc^{-3}$.

Lewis et al. (2002) found a similar relation in the 2dF data; there is a transition in the star formation rate from field-like to cluster-like at the cluster's virial radius and corresponding density. This suppression continues monotonically with radius, leading to central galaxies that have little or no current SF (Couch et al., 2004) (with the exception of CDGs, Section 2.3.4).

Bower et al. (2004) have shown that galaxies in groups (or poor cluster) show a similar trend in the SFR: as a field galaxy begins to enter a group, the SFR is suppressed.

Thus the suppressed SF is not limited to high mass clusters but is instead seen on several scales, and it correlates with the local galactic density (Bower et al., 2004). For groups with a velocity dispersion below $150\,km/s$, the observed SFR is higher than even the field galaxies. This is due to an increased probability for binary galactic interactions which shocks the remaining gas and triggers SF (Couch et al., 2004).

For example, a star-forming spiral falling into a cluster would experience tidal stripping at ~ 1 virial radius. This would remove gas reservoirs from the galaxy and strangle star formation on a timescale of $\tau \sim 1\,Gyr$ (Bower et al., 2004), leading to a galaxy with a passively evolving population (Bower et al., 2004; Nichol, 2004). As the SF is quenched, the emission lines due to star formation (e.g. $H\alpha$, [OII]) also fade (Couch et al., 2004). As this last generation of stars ages, the overall galactic color moves from optically blue to red (Bower et al., 2004).

Evidence for this can be seen in anemic spirals. These are galaxies located near the virial radius (Nichol, 2004) and appear to be gas deficient and have a low SFR.

2.3 Components and structure: The Intra-Cluster Medium

The intra-cluster medium (ICM) was undetected until the advent of X-ray observing technology, despite the fact that the bulk of the baryons in clusters are in this state (Bower et al., 2004). The ICM is composed of gas that has been accreted along the filaments, tidally stripped from the member galaxies, removed during large merging events, and fed-back from supernovae and active galactic nuclei (AGN). As the cluster merges with other galaxies, groups and clusters, shocks propagate through the ICM heating the gas to $10^7 - 10^8$ degrees Kelvin (Rosati, 2004).

Observations of the ICM are useful in many ways. The mean metalicity of the ICM reflects the history due to supernovae enrichment, stellar outflows, etc. The gas is suspended in the gravitational potential which can be used to determine the mass of the cluster (under assumption of hydrostatic equilibrium).

2.3.1 X-ray Observations

The first extragalactic X-ray source was detected in 1966 from M87. Since then, there have been several advances in the technology, making X-ray observations invaluable

tools for studying complex processes and interactions taking place in the ICM.

There have been several X-ray missions since the 1960s and 1970s. However, X-ray imaging of distant sources became possible in the late 1970s. *Einstein* was launched in 1978, providing imaging at 5" (FWHM) and low resolution spectra of clusters (Edge, 2004). However, *Einstein* only did targeted observations, limiting any statistical or evolutionary conclusions. EXOSAT performed follow-up observations in the 1980s (Edge, 2004). These missions detected 55 clusters in X-rays.

The ROSAT All Sky Survey (RASS) was launched in 1990, allowing for high spatial resolution. This mission detected 100,000 soft X-ray sources with a flux limit of $0.3{\cdot}10^{-12}$ to $1.0 \cdot 10^{-12} erg \cdot s^{-1} \cdot cm^{-2}$ (Edge, 2004). Of these, ROSAT identified nearly 1200 candidate clusters (Edge, 2004). This mission provided the first reliable statistical survey of X-ray emitting clusters.

The Italian satellite Beppo-SAX was launched in 1996. This instrument provided spectra from 0.1 to 200 keV, with 1' imaging possible from 0.1 to 10 keV (nasa.gov, 2005). Beppo-SAX was designed to resolve spectra of clusters and provide information on the ICM temperature structure, cooling flows, and metalicity information. Also working to observe the ICM temperature structure were the RXTE and ASCA missions. RXTE was sensitive to hard X-rays; ASCA was designed for soft X-ray detections. These 3 observatories made the first sensitive X-ray spectra observations and provided temperature measurements (nasa.gov, 2005).

X-rays are excellent tools for selecting clusters to a flux limit, despite the brightness and distance biases (Edge, 2004). The X-ray surface brightness decreases as $(1 + z)^4$, strongly limiting observations of higher redshift objects (Rosati, 2004). To date, X-rays have provided a detailed picture of the overall structure of the low redshift, projected ICM (Rosati, 2004; Edge, 2004).

2.3.2 The *Chandra* and XMM-Newton X-ray Observatories

The ESA's XMM-Newton observatory was launched in 1999. XMM was designed for spectral observations at a limiting flux of $10\, erg \cdot cm^{-2} s^{-1}$. XMM is capable of 5 arcsec resolution imaging in the range of 0.1 to 12 keV (Edge, 2004). Spectra are provided by two spectrometers, allowing medium-resolution from 350 - 2500 eV (sci.esa.int, 2005).

The *Chandra* X-ray observatory was also launched in 1999. This unique instrument

uses hyperboloid and paraboloid mirrors to achieve sub-arc second imaging. At low redshifts, *Chandra* has a resolution on kiloparsec scales; at higher redshifts, *Chandra* is still be able to resolve structure at 100 kiloparsecs (Rosati, 2004). Beyond $z = 1.3$, *Chandra* is able to detect emission, but cannot resolve internal structure of the ICM (Rosati, 2004). Through these observations, *Chandra* has been able to study the ICM morphology and the ICM surface brightness at $z > 1$ in greater detail than any previous instrument.

Chandra is also equipped with 3 spectrometers. The Advanced CCD Imaging Spectrometer (ACIS) records the energy of each photon as it is acquired by the imaging CCD array. This allows for low resolution spectroscopy. The High and Low Energy Transmission Grating Spectrometer instruments (HETGS and LETGS) provide high resolution spectroscopy in the 0.4 to 10 keV and 0.08 to 2 keV energy range, respectively (chandra.harvard.edu, 2005).

2.3.3 ICM Properties

The ICM gas is often described as an isothermal body of gas in hydrostatic equilibrium (HSE). This simplified view may be reasonable as an overall description, however, the ICM is far from a steady-state, uniform-temperature body of gas.

The ICM has a typical density of 10^{-4} to $10^{-2}\, atoms \cdot cm^{-3}$ and contains 10 times more mass than the cluster's stellar populations (Mushotzky, 2004). X-ray temperature maps show the ICM to hold a relatively constant temperature with radius irrespective of the changing density profiles from 0.05 to $0.6\, R_{Virial}$ (Mushotzky, 2004).

The gas is highly ionized with an average temperature of 10^7 to $10^8\, ^\circ K$. At this temperature, the primary cooling mechanism is thermal Bremsstrahlung radiation (Edge, 2004). This cools the gas on a timescale proportional to $P/(\rho\Lambda)$, where Λ is the cooling rate, P is pressure, and ρ is the density. Estimates of this cooling time are shorter than the Hubble time, implying that the clusters should be cooling and display a decreasing temperature profile. In order to explain the constant temperature observations, a heating mechanism is required. Without heating, a cooling flow is expected: the cooled gas becomes more dense and moves into the central core.

The inclusion of heating mechanisms is supported by the observed temperature-bolometric luminosity relationship. With no ICM energy injection, the cluster cools via

radiation. This would lead to a $L_B \propto T^2$ correlation (Mushotzky, 2004). However, the data follow $L_B \propto T^3$.

The ICM is heated via galaxy outflows, cluster merging, AGN, shocks, supernovae, and outflows from star forming regions. Each of these heat the ICM, breaking the self-similarity and allowing for more complex structure. Also, these processes enrich the ICM with metals, distribute materials, and affect the cluster's evolution.

The metalicity of clusters vary from $0.1 to 0.65$ of the solar value, with higher density clusters having a higher metalicity (Edge, 2004). The distribution of the metals is relatively constant throughout the cluster, once out of the central core (Mushotzky, 2004).

2.3.4 Intra-cluster Processes and Interactions

Within a cluster, several processes directly interact with the ICM. These processes inject energy, disrupt HSE, and transport energy and material. Despite this, clusters with cooling flows are in HSE; this is based on the agreement between the lensing mass and the X-ray derived mass (Grego, 2001) (see Section 2.4.2). Cooling flows act as a transport mechanism and are a cooling process; in this section, cooling flows and additional processes will be discussed.

In previous sections, the ICM has been referred to as a fairly stable isothermal system, as well as to passively evolving stellar populations in cluster galaxies. This is a simplified view that may be applicable to much of the cluster, but does not hold at the very center. *Chandra* has observed the surface brightness profiles to a resolution of tens of kiloparsecs for several clusters. On these scales, a central decrease in the X-ray emission is observed due to the locally reduced temperatures (McNamara, 2001).

These 'cool cores' are due to large bodies of cool gas (10 to 100 °K) that sink into the central core and displace the hot X-ray emitting gas via buoyancy (McNamara, 2001). Here, the ICM is not isothermal and is best described as a complex, multiphase system in which feedback from supernovae and AGN are important. This depression in the X-ray is also spatially correlated with very luminous ($L > 10^{42}\, erg/s$) radio lobes (McNamara, 2001). These radio lobes are less dense than the surrounding medium and may be contained via magnetic fields.

These lobes may be the source for "ghost cavities." Here, neither X-ray nor radio

emission are seen. The current explanation for ghost cavities involves radio lobes, whose power source has ceased. The lobes would expand, cool, and rise out of the cluster, evolving beyond the limits of radio detection. Such a scenario would distribute up to $10^{58-59} ergs$ back into the ICM as each bubble disperses (McNamara, 2001). These ghost cavities would then be a historical record of the active/passive periods of the radio source.

Radio relics are another structure seen in clusters of galaxies and are evidence of magnetic fields. Relics are large diffuse regions of radio synchrotron emission; from this emission the magnetic field strength can be derived. Cluster-wide magnetic fields have been found to be about 0.1 to 1 μG. The classical relic morphology is elongated, located in the mid- to outer-cluster, and extends 400 to 1500 kpc. Often the elongation is seen in the radial direction. Relics can also appear as a radio halo around the cluster (Giovannini & Feretti, 2004).

Relics also tell us how much we do not yet understand, as the source of these relics are currently unknown (Giovannini & Feretti, 2004). Relics are not related to AGN activity, but appear to be created during cluster mergers and subsequent shocks propagating through the ICM. If this is the case, relics may be able to help us determine the energy released into the ICM during a merger, the mechanisms for transport of the shock energy, as well as retaining an imprint of past mergers (Giovannini & Feretti, 2004).

Ghost cavities, radio relics, and cooling flows would all disrupt the validity of HSE as well as the general isothermal properties of the ICM. None the less, observations of these objects can tell us a great deal about the ICM and a cluster's history. Yet these are not the only processes that affect the ICM.

The ICM can also absorb energy from galactic mergers, AGN, supernova, and stellar winds. Several of these events also alter the ICM's metalicity. Mergers are important in describing the morphology and possibly the mixing and shock structure seen in the ICM and active galactic nuclei (AGN) are believed to be a dominant energy injection mechanism (De Lucia et al., 2004).

As mergers and galactic stripping cannot account for the high metal content of the ICM, supernovae from the early star-forming times at $z \sim 2 - 4$ are thought to be the primary source of metal enrichment of the ICM. Given the SFR or initial mass function,

it is still difficult to achieve the required yield. This has lead to an assumption that the IMF may have been top heavy: the first stars were biases towards higher masses; this would increase the SN rate (De Lucia et al., 2004). Also, if observations of Lyman break galaxies are correct, these galaxies may have been forming stars since $z \sim 5$, thus reducing the need for a top-heavy IMF (De Lucia et al., 2004).

2.3.5 Cluster Mass Estimates from the ICM

The ICM can also be used to estimate cluster mass. If it is assumed that the gas traces the gravitational potential, we can use the gas properties to derive the radial profile of the overall matter distribution.

As seen in Figure 2.2, observations have determined a correlation in X-ray temperature vs. galaxy dispersion. This relation can be determined, analytically, assuming the gas and galaxies have similar velocities and dynamics (Rosati et al., 2002).

$$k_B T \backsimeq \mu m_p \sigma^2 \backsimeq 6 \left(\frac{\sigma}{10^3 \, km \cdot s^{-1}} \right)^2 keV \tag{2.1}$$

With this, temperature data can be used to determine the velocity dispersion of the gas. Using the assumption that the galaxies and gas have similar dynamical structures, we can determine the cluster's mass: $M = \langle R \rangle \sigma^2 / G$ (Shore, 2003).

A similar technique uses the ICM's temperature to determine the mass of the cluster based on assumptions of HSE, the isothermal nature of the ICM, and a spherical geometry. Using a spherical application of HSE, Evrard (2004) obtains:

$$\frac{GM(< r)}{r^2} = \frac{-\nabla P}{\rho}. \tag{2.2}$$

Once the gas pressure and density profile has been determined, the cluster's mass can be determined.

Both of these methods incorporate several assumptions. As such, it is not surprising that the ICM-dependent mass estimates disagree with other methods (galaxy dispersions or gravitational lensing) up to a factor of 2 to 3. The ICM-dependent methods tend to under-predict the mass; this is discussed further in section 2.4.2.

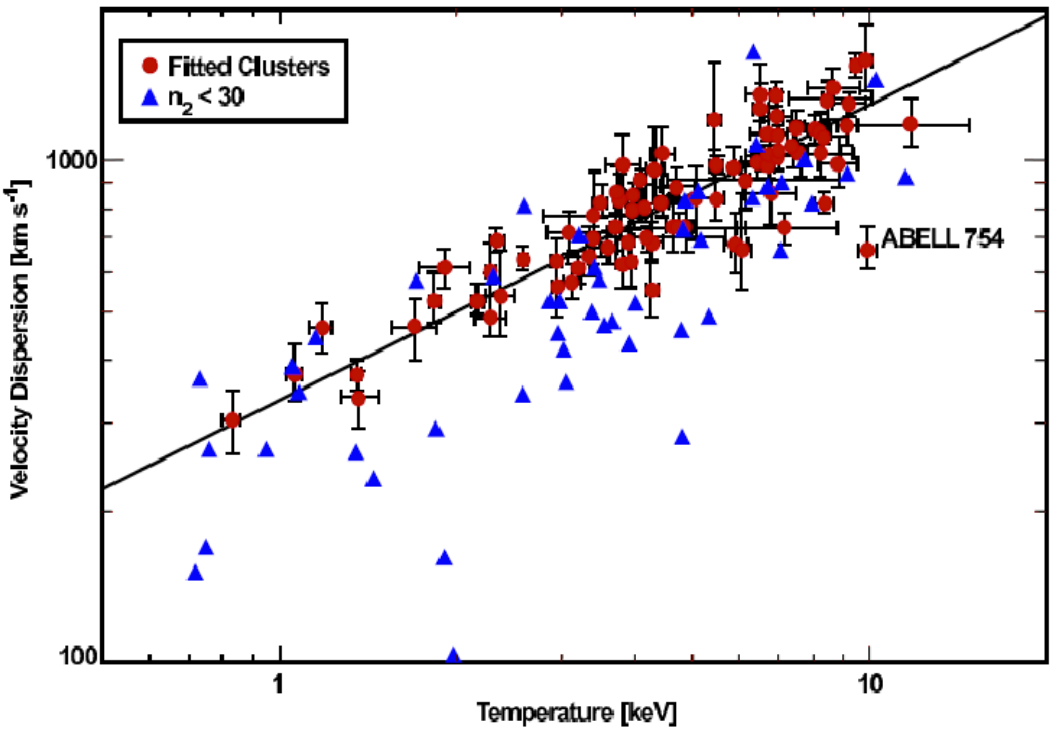

Figure 2.2: This graph (from Mushotzky (2004)) shows the observed relation in galaxy velocity dispersion with X-ray temperature. Blue triangles represent clusters with 30 or fewer member galaxies (poor clusters).

2.3.6 The Sunyaev-Zel'dovich effect

The thermal Sunyaev-Zel'dovich (SZ) effect is the comptonization of cosmic microwave background (CMB) photons off the ICM. Here, the CMB photons pass through a cluster and scatter off hot electrons in the dense gas, increasing the average energies of the photons. This process, where the photons gain energy via electron interactions, is known as inverse-Compton scattering.

Measuring this signal in the CMB is actually the same at all redshifts. This is because the surface brightness of the SZ effect is related to the energy of the CMB photons, which were more energetic in the past (Birkinshaw, 2004). This effective increase scales as $(1 + z)^4$ and is observed at redshifts higher than 1.62 (assuming a ΛCDM universe) (Birkinshaw, 2004). This means that the SZ effect can be used to locate clusters back to any redshift, as long as the ICM has already formed; the flux density of the SZ effect is proportional to the total ICM electron energy w.r.t. the angular diameter distance squared (Birkinshaw, 2004).

This effect causes the relative temperatures of the CMB to change. A simple depiction is shown in Figure 2.3. The CMB, when observed directly in the line of sight with the cluster, will appear hotter. These CMB photons will enter the ICM, inverse-Compton scatter and (on average) will exit the ICM with more energy. Also, CMB photons from nearby regions may interact with the CMB, and inverse-Compton scatter into our line of sight. This also contributes to the heated CMB towards the cluster.

The SZ effect can also be used to determine H_o. The X-ray surface brightness is proportional to $n^2\Lambda(T)L$ where n is the electron density, Λ is the cooling factor, and L is the path length through the cluster (Birkinshaw, 2004). The SZ effect, measured as a change in temperature, is $\Delta T \propto nTL$ (Birkinshaw, 2004). Thus, with X-ray and SZ observations, we can solve for the path length of a cluster. Using the assumption that a cluster is spherical, we can equate the path length to the diameter and find the Hubble constant.

This assumption of sphericity also introduces the strongest bias into the SZ observations: clusters that are oriented along the line of sight scatter more CMB photons toward us. The SZ effect becomes more pronounced, increasing the likelihood that it will be detected. Observations of the SZ effect are currently being carried out on bolometers and interferometers. These observations will be a mass limited sample, as a large

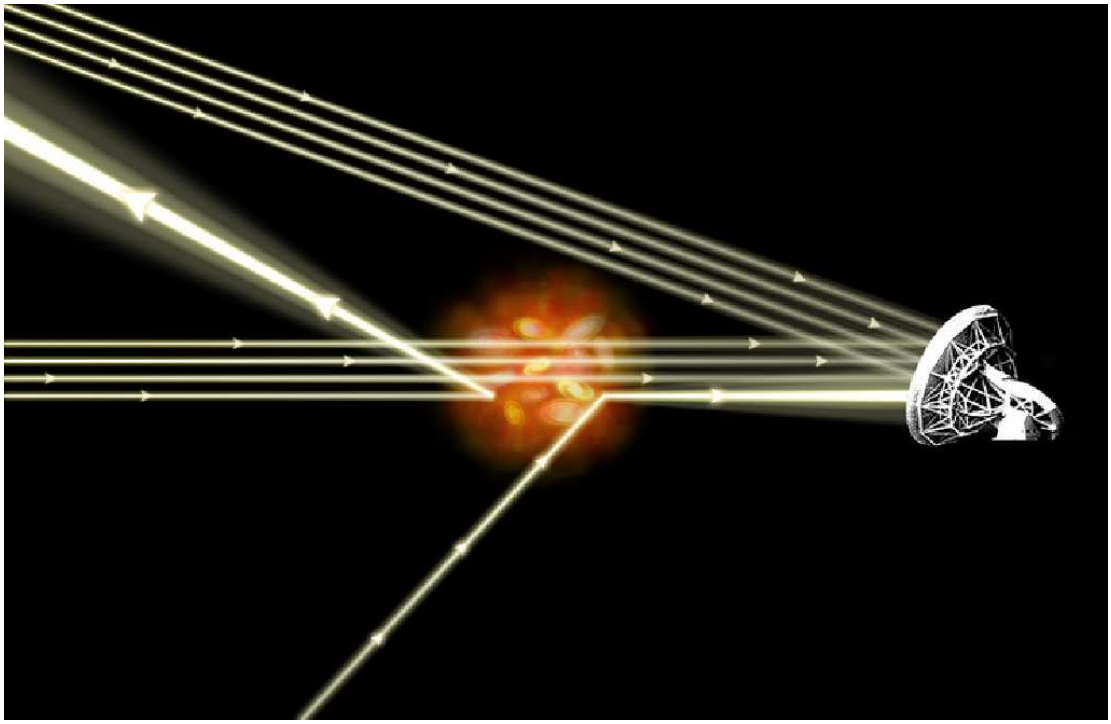

Figure 2.3: The observed temperature of the CMB is altered due to inverse-Compton scattering. As the CMB photons traverse the ICM, a small number of them will interact with the gas. Most interacting photons receive an increase in energy; a small portion will lose energy. As light from different pieces of the sky are scattered into our line of sight, which gain energy, the CMB at this position appears hotter. This figure is from chandra.harvard.edu (2005)

body of dense gas is needed to inverse-Compton a large number of photons (Birkinshaw, 2004). These detections will allow for a high redshift study of clustering and structure.

Akin to this thermal SZ effect is the kinematic SZ effect. This effect is caused by a relative motion of a cluster w.r.t. the CMB, producing a signal that is $\sim 1\%$ of the thermal SZ effect (Birkinshaw, 2004). Currently observations of the kinematic SZ effect are not possible.

2.4 Components and Structure: Dark matter

Dark matter is the dominant mass component in clusters of galaxies, yet it is also the most elusive. Dark matter can only be measured through its effects on regular matter and radiation. Despite this, it has been speculated since the 1930s, before the discovery of clusters, that there must be additional, non-observed mass in clusters.

Zwicky studied the kinematics of galaxies and noted how much mass would be needed to reproduce their motions. The mass inferred from kinematics was much higher than could be accounted for with all of the observed stars and galaxies. This is known as the "missing mass problem."

Today, we have a much more thorough understanding of the matter components within a cluster. Using several methods, we can determine the mass, mass distribution, and the motions of the dark matter.

2.4.1 Gravitational Lensing Observations

Gravitational lensing is an effect light experiences when it passes through a gravitational field. As light passes through a strong gravitational field, it will follow null-geodesics and be deflected. The amount of displacement is relative to the strength of the gravitational field. The a minimum mass surface density, Σ_{crit}, required to lens a distant source is (Wu, 1995):

$$\Sigma_{crit} = \frac{c^2}{4\pi G}\frac{D_s}{D_d D_{ds}} \tag{2.3}$$

Figure 2.4 depicts strong gravitational lensing of a background source. The light's path is deflected towards the mass by a small angle – and towards the observer – causing the images to appear displaced away from the lens. The images may also be magnified

and deformed depending on the lensing geometry.

In 1979, Walsh made the first cosmological observations of gravitational lensing. Since then, lensing has become an invaluable tool when studying clusters of galaxies. Gravitational lensing by clusters results in the distortion of background galaxies' images. These background sources are at $z > 1$ and are distorted into arc-like images concentrically surrounding the mid- to low redshift lensing clusters (Blandford & Narayan , 1992). An example of this is shown in figure 2.5.

Using the assumption that a cluster is spherically symmetric, the lensing arcs can be used to determine the mass of the system interior to each arc. This mass determination is only dependent on the cluster's mass and the geometry of the lensing system. There are no dependencies on distance ladder estimates, assumptions of HSE, or the kinematic state of the cluster. Lensing is an independent estimator of a cluster's mass that we can use to compare with non-direct methods, such as those derived from the T_{X-ray} profiles and HSE or the kinematic mass estimate.

The assumption of spherical symmetry would not be a valid assumption in a cluster currently undergoing a large merging event. However, with more complex modeling of lensing systems, deviations in the mass-distribution can be reconstructed to explain the observed lensed images. By using more complex (i.e. non-spherical lens symmetry), gravitational lensing is able to probe the cluster's mass distribution, hopefully down to scales of 10 kpc (Smail, 2004).

2.4.2 X-Ray vs. Lensing masses

Both gravitational lensing and X-ray profiles are able to provide estimates of the cluster's total mass. However, as seen in table 2.1, the two estimates disagree. The mass derived from X-ray surface brightness profiles is 3 to 7 times smaller than the lensing derived mass. Clusters of galaxies with small cores (< 50 kpc) and high X-ray gas densities tend to have a better agreement between the X-ray and lensing masses (Smail, 2004). (Allen, 1998, Figure 3) performs a similar analysis, but focus on clusters that appear to be relaxed. A relaxed cluster is better described by HSE, giving better mass estimates. Their 13 clusters show excellent agreement (less than a factor of 2 difference) between the X-ray and lensing masses.

There are several possible causes for this discrepancy, most of which are derived

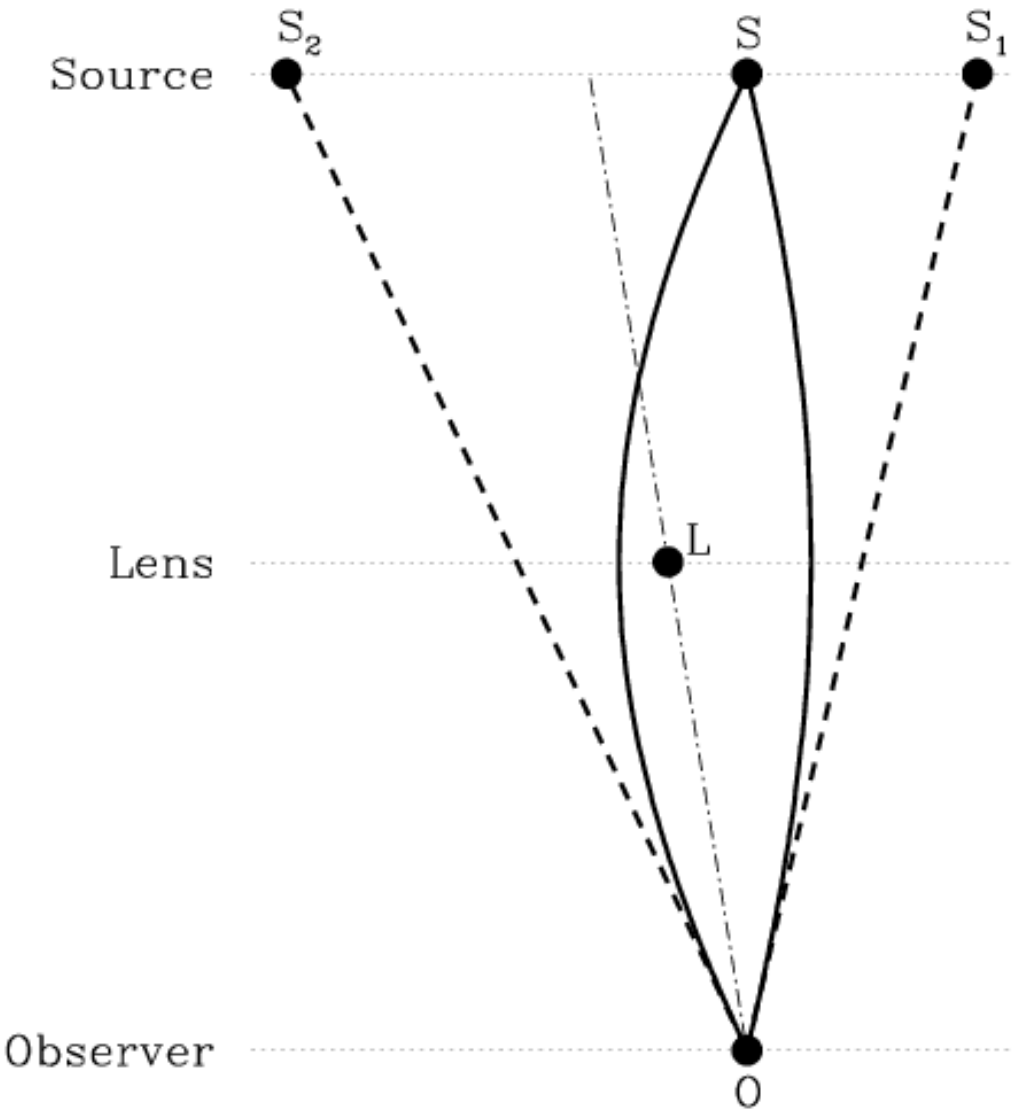

Figure 2.4: From Wambsganss (1998), this figure illustrates the geometry of a lensing system. The light from the background source (S) is deflected by the lensing mass (L). Observation of a lensed source causes the image(s) (S1 and S2) to appear displaced, and possibly magnified and distorted.

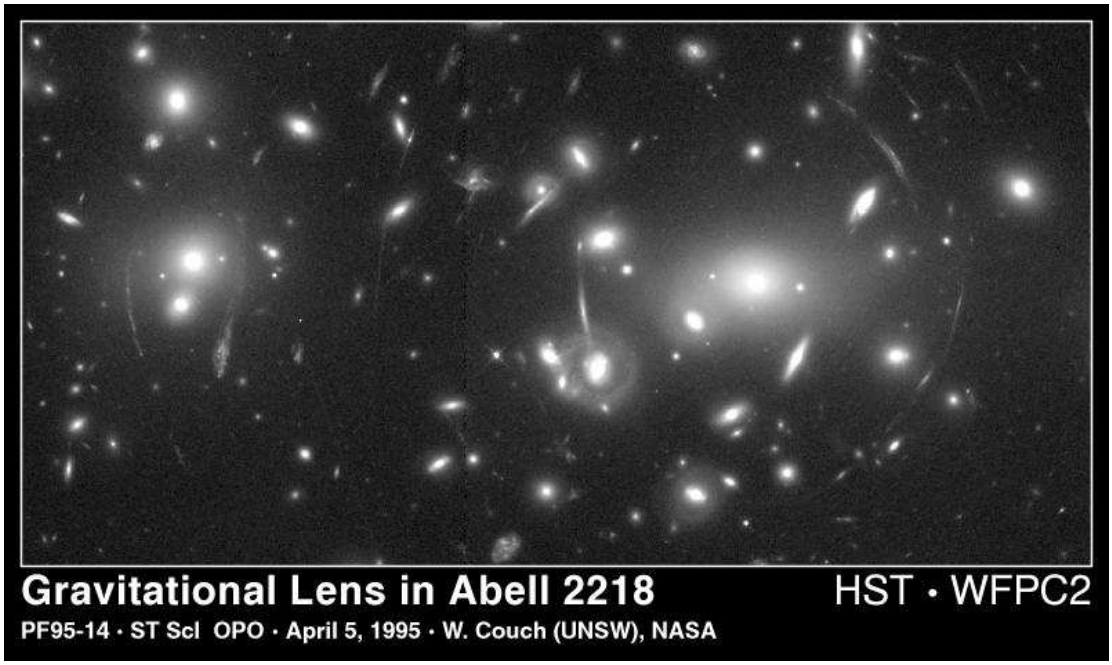

Figure 2.5: This image shows an example of lensed arcs, cluster Abell 2218. The gravitational lensing is evident by the arc-like images encircling the cluster (Wambsganss, 1998).

Cluster		Arc	Mass ($M_\odot$)		
name	z_d	z_s	M_{X-ray}	$M_{cluster:lens}$	$M_{cluster:lens}/M_{X-ray}$
Abell 370	0.374	1.3(?)	$2.26 \cdot 10^{14}$	$8.20 \cdot 10^{14}$	3.63
MS1006.0+1202	0.221	0.6	$1.36 \cdot 10^{14}$	$6.91 \cdot 10^{14}$	5.08
		2.0	$1.36 \cdot 10^{14}$	$4.87 \cdot 10^{14}$	3.58
MS1008.1-1224	0.301	0.6	$1.36 \cdot 10^{14}$	$7.47 \cdot 10^{14}$	5.60
		2.0	$1.36 \cdot 10^{14}$	$4.34 \cdot 10^{14}$	3.25
MS1910.5+6737	0.246	0.6	$1.36 \cdot 10^{14}$	$9.95 \cdot 10^{14}$	6.12
		2.0	$1.36 \cdot 10^{14}$	$6.64 \cdot 10^{14}$	4.08

Table 2.1: From Wu (1995), this table shows 4 clusters with the derived masses using the lensing technique and the HSE technique. The redshift of the cluster is z_d and z_s is the redshift of the background source. The projected virial mass derived from the X-ray surface brightness profile is listed as M_{X-ray} with the mass estimates from gravitation represented as $M_{cluster:lens}$. The cluster estimates are significantly larger than the X-ray gas estimates.

from the original assumptions. First, HSE is almost certainly not true, but seems to be more valid in evolved, dense clusters (Smail, 2004). The ICM may also be supported by more than just pressure; clusters have been shown to have a magnetic field (Carilli & Taylor, 2002), but magnetic pressure has been neglected in this treatment (Wu, 1995). Interactions and merging in the system may also disrupt equilibrium and heat the surrounding gas, which would tend to lower the X-ray derived mass.

Also, the overall cluster geometry may affect these estimates. If the cluster is not spherical, but is triaxial (the most common configuration) along our line of sight, the de-projection of the cluster's gas density derivation will be affected; this would also tend to lower the X-ray derived mass.

With all of these possible, and likely, sources of error, it is impressive that these estimates agree as well as they do. The discrepancy between these two estimates can be used to estimate how much we still do not yet understand about the intricate processes in the ICM and a cluster's equilibrium state.

2.4.3 Dark Matter Distribution

The spatial distribution of dark matter can only be determined by observing its effects on other objects. The dark matter halo extends well beyond the galactic population and

beyond the hot ICM. Classically, the dark matter distribution in galaxies was determined by observing the velocity structure of stars. The orbital velocity of each star is only dependent on the radius, and the mass interior to its orbit. At each observed star's position, the interior mass could then be determined. With observations at several radii, a rough estimate of the total mass distribution could be derived.

This technique describes the total mass distribution. In order to derive the dark matter's mass distribution, the normal matter's contribution must be removed (Smail, 2004).

The main source of error in this approach is the uncertainty in the 3-D velocity structure of the orbits (Williams, 2003). In spiral galaxies, disk stars could be assumed to have circular orbits. We do not have this constraint when measuring galaxies' orbits in a cluster.

Lensing techniques offer another method for determining the dark matter mass distribution (see section 2.4.1). Deviations form a circular arc pattern (due to a non-spherical mass distribution) can be used to constrain the total matter distribution to the scale of large sub-structures. Sub-structures within the cluster will cause a secondary deviation or distortion on the arcs whose light path travels near the substructure. Similar to the dynamical method, this determines the total mass distribution.

These methods are useful in probing the actual mass distribution in clusters, but provide little information on the evolution, formation, and sub-structure of dark matter halos. It is in this arena that numerical simulations are making significant progress (see section 1.1.1.

Most of these simulations produce a similarly shaped density profile (see section 1.2). This trend is a viable description for halos of varying mass, varying initial conditions, and even varying cosmologies. As such, the qualitative fit presented by Navarro et al. (1996) is often used as a general description. The details of this fit and others are discussed more in Section 1.2.

Observationally, clusters display a dark matter mass distribution similar to that of the NFW profile, though the inner halos tend to have shallower cores than NFW model (Smail, 2004).

2.4.4 Dark Matter Velocity Structure

Despite the various methods available to probe the dark matter distribution, very little is known about the velocity structure of dark matter halos. When estimating the cluster's mass via the X-ray temperature method, it is assumed that the dark matter velocities are similar to that of the gas. However, as dark matter interacts very differently than gas, this may not be the best approximation.

Simulations are currently providing the most information regarding collisionless systems' velocity structures. As the simulated density profiles are similar to observations, the simulated velocity structure might also describe the actual velocity structure.

In simulations, the velocity dispersions tend to be $\approx 10^{2.5}\, km/s$ throughout, with a weak maximum occurring within the virial radius. The velocities are isotropic in the central halo, and become more radial at the outer halo (Shapiro et al., 204).

2.5 Evolution of Clusters

Clusters of galaxies are dynamical systems constantly undergoing evolution. We can use the evolution within the ICM and the member galaxies to describe their evolutionary state and infer their formation history.

Chandra observations extend to $z = 1$, allowing evolution studies up to this point. The main result from these observations is that clusters are already highly evolved by $z = 1$. Temperature and surface brightness profiles of high redshift clusters are similar to low redshift clusters (Rosati, 2004). ICM morphology is also seen, on average, to be similar to low redshift clusters (the exception being actively merging clusters, see Section 2.6.4). This information implies that clusters are advanced evolutionary systems and that, by $z \sim 1$, the ICM gas and galaxies have been able to thermalize and relax into the cluster's potential.

The evolution before z=1-1.5 is not as well observationally constrained, though radio emissions have been used to locate distant clusters extending to $z \sim 4$ (Rosati, 2004). Also, Lyman-α systems are being used to study early star-forming systems, which may be the antecedents to today's clusters (Rosati, 2004).

2.5.1 Galaxy Evolution in Clusters

Galaxies well within the boundaries of clusters are a special sub-sample of galaxies. These galaxies preferentially formed earlier than nearby field galaxies, as they formed in a region of higher density. These galaxies are also observed to have different star formation rates and morphologies than field galaxies (Sections 2.2.6 and 2.2.7).

Field galaxies and cluster galaxies exist in very different environments, and their evolution should reflect this difference (Bower et al., 2004). Cluster galaxies are subjected to stronger gravitational potentials and dynamic friction with galaxies and the intra-cluster medium (Section 2.3) (Smail, 2004).

Cluster galaxies also undergo mergers and tidal interactions with their neighbors. This fuels SF, creating bluer, younger stellar populations (Bower et al., 2004). As the integrated number of mergers increases with time, the galaxies' dark matter halos are truncated, resulting in a more global cluster potential with less pronounced substructure (Section 2.5.2) (Taylor & Babul, 2005).

Low redshift evolution is seen in the E+S0 populations. At $z < 1.2$, these galaxies show tight correlations in the evolution of the mass to light ratio: $M/L \propto M^{0.24} \propto t^{0.8}$ (Franx, 2004). E+S0 galaxies also show a resilient color magnitude relation in low redshift observations (Franx, 2004). However, this relationship breaks down at $z > 2$ (Bower et al., 2004). This means that E+S0 galaxies were formed before $z \geq 2$.

The global star formation rate also evolves with redshift. In the universe, the mean star formation has decreased monotonically since $z = 3$ (Papovich et al., 2005). Since a $z = 1 - 2$, the overall SFR has dropped 3-10 times (Bower et al., 2004), supporting the consensus that cluster cores have old stellar populations that formed at $z > 2$ (Bower et al., 2004). Consequently, the recent ($z < 1.5$) star formation tends to be seen in younger field galaxies (Bower et al., 2004).

Observations of early, high redshift systems are done with Lyα-break galaxies. These galaxies are large star forming galaxies seen at $z > 2.5$ (Bower et al., 2004). These galaxies may be the progenitors of large galaxies now seen in clusters.

2.5.2 Hierarchical merging in clusters

Independent studies based on WMAP, Lyman-α systems, 2dF, etc. have shown that structures form hierarchically. This means that smaller structures formed first and were accreted into larger and larger objects over time (Ostriker, 2004). During this processes, small objects continue to form in the lower-density regions outside of clusters and groups.

A cluster forms from matter accreted from several mega-parsecs of space (Carlberg, 2004). As the material is accreted along filaments, the material encounters a more dense environment, affecting the evolution of galaxies (Section 2.5.1) and creating shocks during adiabatic compression (Carlberg, 2004; Hallman, 2004).

Observationally, 2dF has confirmed the accretion of smaller objects into clusters, by determining the positions and velocities of galaxies as they fall into a cluster's potential (Edge, 2004). Once a galaxy has been accreted in to the cluster (now referred to as a sub-structure), it is subjected to non-linear processes such as dynamical friction, tidal disruption (mass-loss) and merging with other sub-structures.

The relaxation time for the accreted material is short w.r.t. the timescale for major collisions ($\tau \sim 100 Myr$ (Nichol, 2004)). As such, we would expect most galaxies within clusters to be in equilibrium at any given time after the main cluster is formed (Donahue & Voit, 2004).

Simulations have shown that most large mergers occur between $z \sim 1-2$ with small mergers occurring from $z \sim 1-4$ (Taylor & Babul, 2005). Observationally, we see evidence of merging at $z \sim 1$ with double-core clusters (Section 2.6.4) and accretion of galaxies (Section 2.5). The amount of dark matter stripped from the galaxy is related to the amount of time the galaxy has been in the cluster (Taylor & Babul, 2005), thus we would expect larger amounts of substructure within high redshift clusters. The substructure's central density decreases (due to stripping), the density distribution is truncated, and up to 80% of the mass is removed and added to the parent cluster.

The result of hierarchical merging is the formation of larger objects (clusters, in our case). The outer parts of the cluster's density profile will change, the cluster's mass will increase, and virial radius will increase (Taylor & Babul, 2005).

2.5.3 Metalicity

Optical, infrared, and X-ray observations are able to determine the metal content of a cluster's ICM and its member galaxies' stellar composition. By observing clusters at different stages of evolution, we can study the evolution of the metalicity within clusters of galaxies.

Beppo-SAX and ROSAT have found radial and temperature trends in clusters' ICM metal abundances. On average, the central cluster metalicity is 0.006 in mass or ≈ 0.3 of solar values. This holds for ICM temperature from $3 \leq kT \leq 9\,keV$ (Renzini, 2004). However, low temperature clusters ($1 \leq kT \leq 3\,keV$) display a much less defined metalicity, ranging from 0.1 to 1.2 of solar values (Renzini, 2004). The cause for this change in metal content in cool cluster cores is currently unknown.

Radial gradients in metalicity were also found. As can be seen from figure 2.6, not all clusters display this radial gradient. Clusters with cool cores display the radial gradient; non-cool-core clusters do not show this morphology. The physical intuition for his trend has yet to be established.

The observed oxygen, neon, magnesium, calcium, silicon, sulfur, and argon metals are attributed to Type II supernovae (SN), where as elements similar in mass to iron (iron-peak) elements are mainly due to Type Ia SN. Using the chemical abundances, it may be possible to determine the rate of SN and the relative number of Type Ia and Type II SN taking place in clusters.

Type Ia SN are predicted to have occurred at a rate of $0.16 \pm 0.06 \cdot 10^{-12}\, h_{70}^2\, L_{B_\odot}^{-1}$ per year in cluster E/S0 galaxies, each producing $0.7 M_\odot$ of iron. SN type II are less well-constrained. Each SN type II produces $0.002\, M_\odot$ to $0.3\, M_\odot$ with the SN rate dependent on the initial mass function (IMF) Renzini (2004). Taking these into account, Renzini (2004) finds that SN Ia can produce one-tenth the observed metal values. As such, SN do not seem to be able to reproduce the observed metal abundances. To explain observations, the IMF, SN rate, or the SN yield may need to be altered.

The metal content of the ICM appears to be twice that of galaxies. This implies that galaxies lose more metals to the ICM through ejection processes than are recycled into the galactic stellar population.

The evolution of the metalicity is not yet well-constrained with observations. Renzini (2004) proposes that at z=3, the metalicity was $\approx 30\%$ of today's value by estimating

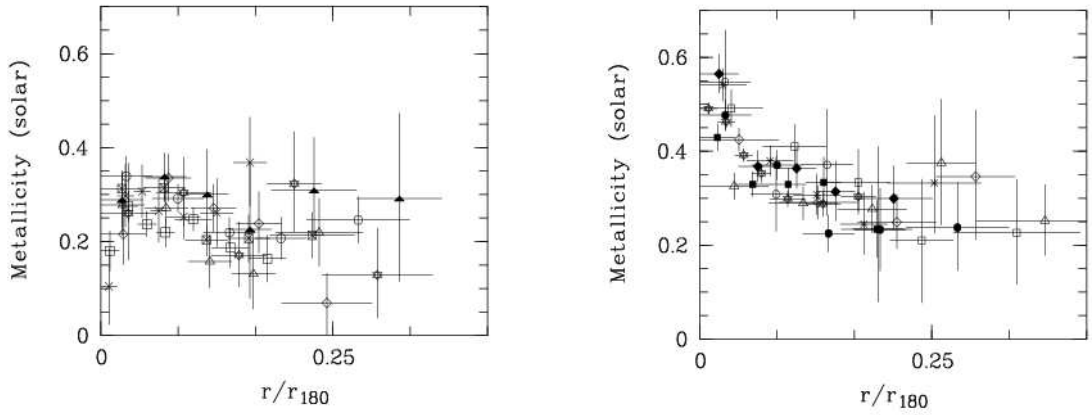

Figure 2.6: This figure, from Renzini (2004), shows the metalicity profiles for two types of clusters. The left figure is a non-cool-core cluster, while the right figure shows a cluster with a cool core. The difference in metalicity profile morphology due to the different temperature structures is not yet well understood.

that 30% of the stars had been formed by z=3. By this reasoning, the metalicity at z=3 would have been 0.1 times that of the current solar value.

The metalicity evolution is important to understand, as metals affect star formation, star evolution, and radiative cooling rates. Currently, models under-predict observations of metal abundances, and the evolution of the metalicity can only be as well-constrained as the initial mass function and stellar populations in clusters.

2.6 Constraints on Cosmology

Clusters are the largest bound structures in the universe. Due to the hierarchical nature of structure formation, clusters are also the newest category of structure to form. The inner cluster is assumed to be virialized, but the whole structure is still forming and has not entirely reached equilibrium. This makes clusters sensitive to cosmological parameters that affect structure formation and the distribution of mass in the universe (Rosati, 2004).

2.6.1 Cosmological parameters: Ω_M

Ω_M describes the density of total matter in the universe w.r.t. the critical density: $\rho_{crit} = 1.9 \cdot 10^{-29}\, h^2 g\, cm^{-3}$.

$$\Omega_M = \frac{\rho_M}{\rho_{crit}} = \frac{\rho_{dark\,matter} + \rho_{baryons}}{\rho_{crit}} = \Omega_{baryons} + \Omega_{dark\,matter} \tag{2.4}$$

Accurate determinations of this parameter are important, as it is needed to describe the geometry of the universe and the rate of structure formation.

Clusters of galaxies are assumed to contain a representative sample of baryonic and dark matter in the ratio expected throughout the universe. Thus, measurements of a cluster's M/L ratio can be used to describe the universal value of Ω_M. The M/L ratio is a measure of the amount of total mass of the cluster relative to the luminosity of the cluster. This is then normalized to the solar values.

If the universe were purely matter dominated, and had a flat geometry, $\Omega_M = 1$ would imply a M/L ratio of 1500 times the solar value (Williams, 2003). As can be seen from Table 2.2, the typical rich cluster's M/L ratio is 300. This corresponds to an

Property	Rich Clusters	Poor Clusters and Groups	Compact Groups
Number of Members	30-300	3-30	4<
Radius (Mpc/h)	1-2	0.1-1	0.1
Mass within 1.5 Mpc ($10^{14}h^{-1}M_{\odot}$)	1-20	0.03-1	0.03-1
σ (kms^{-1})	400-1400	100-500	200-250
$L_B(10^{12}L_{\odot})$	0.6-6	0.03-1	0.03-1
$M/L_B(hM_{\odot}/L_{\odot})$	300<	200	200
$L_X(10^{10}h^{-2}L_{\odot})$	1-25	-	0.1-0.3
T (keV)	2-14	-	$\sim$1

Table 2.2: Based on Shore (2003), this table lists properties of clusters of different sizes.

Ω_M value of 300/1500 $\approx$ 0.2. This is slightly lower than the currently accepted value $\Omega_M \approx 0.3$ as determined from the CMB and supernova constraints (Figure 2.7). This difference can be explained as an error in the mass determinations and the assumption that the luminosity accounts for all of the matter in the halo.

2.6.2 Baryonic Content: Ω_{baryon}

Much like Ω_M, Ω_{baryon} describes the density of baryonic matter w.r.t the critical density. Baryonic matter is a sub-class of all matter. Thus Ω_{baryon} is included in the broader cosmological parameter Ω_M. Ω_{baryon} can also be used to describe the amount of dark matter via the difference in the matter density and the baryonic density.

In the previous section, the M/L ratio was used to describe the total mass contribution in the universe. The M/L ratio is also often used to describe the amount of non-luminous matter in structures. Though, the M/L ratio is not a direct measure of non-baryonic matter: it is also sensitive to sub-luminous populations of baryonic matter (i.e. brown dwarfs, black holes, cool gas, planetary bodies, and dust).

The amount of baryonic matter relative to the amount of dark matter can be derived in a more rigorous way for clusters. X-ray observations are able to give us the ICM gas mass (this is the dominant form of baryonic matter) in a cluster. This can then be compared to the total mass (derived by galaxy velocity dispersion, ICM gas temperature, X-ray Luminosity, or gravitational lensing) to determine the approximate

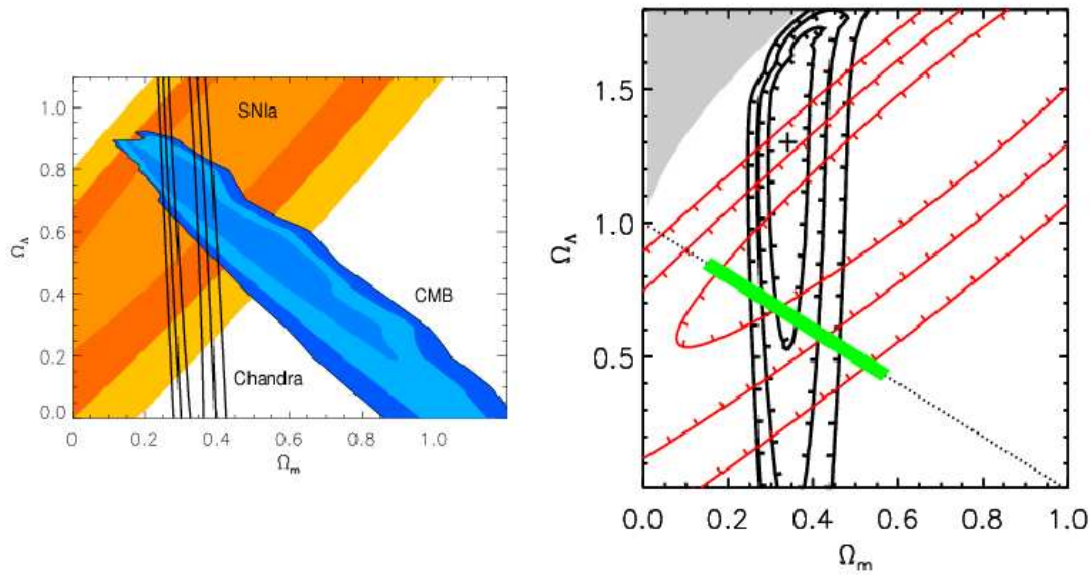

Figure 2.7: *Chandra*'s limits for cosmological parameters Ω_M for two samples of clusters. Left: Clusters in a redshift range of $0.1 < z < 0.5$. Right: High redshift clusters from $0.7 < z < 1.3$ and with a $T > 4\,keV$. The green bar represents WMAP's constraints. (Rosati, 2004)

value of Ω_{baryon}. Using this method, *Chandra* X-ray observations have yielded the fractional content of baryons in a cluster to be $f_{baryon} = 0.15$ (Rosati, 2004). Typical values of Ω_{baryon} are then $\Omega_M \cdot 0.15 = 0.045$ (Rosati, 2004). CMB anisotropies and primordial nucleosynthesis are also able to derive this parameter; these methods predict an $\Omega_{baryon} = .024\,h^{-2}$. If h is assumed to be 0.73, this corresponds to a value of $\Omega_{baryon} = 0.045$. This is similar to the X-ray values.

The currently favored values are $\Omega_M = 0.27 \pm 0.04$, $\Omega_{baryon} = 0.044 \pm 0.004$, and $\Omega_{total} = 1.02 \pm 0.02$ (Bennett et al., 2003). The ratio of Ω_M and Ω_{baryon} describe the amount of dark matter in our universe: $100 \cdot (1 - \Omega_{baryon}/\Omega_M) = 83.7\%$. Approximately 85% of all matter in our universe is dark matter.

2.6.3 Cosmological parameters: σ_8

Perhaps the most straight-forward way to use clusters as probes of cosmology is to use their spatial density to describe the mass distribution in the universe. The number of clusters seen per unit volume can be used to constrain the mass power spectra (Rosati, 2004). The parameter σ_8 is used to define the normalization of the amplitude of density perturbations. This is generally described by the amount of RMS mass dispersion within a sphere of radius $8h^{-1}Mpc$ (Williams, 2003).

By counting the amount of mass fluctuations (via cluster counts), σ_8 can then be derived with a dependence on Ω_M. Current estimates from *Chandra* are $\Omega_M^{0.6}\sigma_8 \approx 0.4 - 0.6$ (Rosati, 2004). If the canonical value of Ω_M is used (Section 2.6.1), this results in $\sigma_8 \approx 0.82 - 1.23$. This value agrees with the derived galaxy normalization: $\sigma_{cluster:galaxy} \approx 1$ (Rosati, 2004). $\sigma_{cluster:galaxy}$ describes the spatial distribution of galaxies, and this derivation of σ_8 is based on clusters. The agreement of these two values indicates that structures of various sizes form with a similar spatial distribution. This implies that the assumption that clusters are a representative sample of the universe is valid.

The degeneracy between σ_8 and $\sigma_{cluster:galaxy}$ can be broken if we study the evolution of σ_8 with redshift (Rosati, 2004). The relative amount of matter, Ω_M, affects the rate at which structures grow. Current observations find little change in σ_8 at varying distances. This implies that Ω_M is small (less than 0.5), as a lower density universe has a lower rate of structure formation. The physical implications of a lower σ_8 value is that fewer

massive clusters will form (Evrard, 2004).

2.6.4 Large Scale Structure Formation

Structure formation is severely constrained by the relative amounts of non-baryonic matter, baryonic matter, radiation, and the cosmological constant in the universe. Early in the universe, radiation was the dominant density component. As radiation does not group into regions of overdensities, structure formation in the early universe was suppressed.

At a redshift $\sim 4 \cdot 10^4 \Omega_M h^2$, matter became the dominant density component (Williams, 2003). The transition between radiation and matter domination is known as the time of matter-radiation equality. At this point in time, non-baryonic matter (which had already become non-relativistic) was allowed to slowly begin to form structures. Baryonic structure growth was still suppressed due to its interactions with radiation. The universe was still opaque, and baryonic matter was not allowed to cool via radiation and hence collapse into structure.

After matter-radiation equality, the universe continued to expand. This cooled the ambient temperature of the radiation and the matter. Eventually, the universe cooled to the point to allow protons and electrons to recombine into neutral atoms. This is the epoch of recombination: $z_{recombination} \approx 1200$ (Williams, 2003). It was during this time that the radiation background was last in contact with the baryonic matter, creating the CMB. This also allowed the universe to become transparent. Baryons were now able to cool by emitting radiation and collapse into structures. In a lower matter density universe, this epoch would happen sooner and structure formation would begin at a higher redshift.

The dark matter had already traced out preliminary structures, and the baryons traced this pattern through gravitational interactions. It is at this point where hierarchical merging begins to take place (Section 2.5.2). Eventually, larger overdensities form, creating the progenitors of today's clusters. By $z \sim 1.3$, clusters (as we know them) have formed, and non-linear structure growth within the cluster creates massive galaxies, such as cD galaxies presently observed within cores of clusters (Rosati, 2004).

At this same time ($z \sim 1 - 2$), cluster accretion of small and comparable mass objects is common (Rosati, 2004). X-ray observations have revealed 3 $z \approx 0.8$ clusters

(RXJ1716, RXJ0152, and MS1054) that show a double core structure in the ICM. This trend is also seen in the spatial distribution of their member galaxies, though dynamical information has yet to be obtained (Rosati et al., 2002).

These clusters have been interpreted as undergoing current mergers. At this redshift, it is expected from hierarchical models to see clusters merging with entities of similar mass. It is also expected to see the relative amount of substructure increase with redshift. Even with these few data points, it is apparent that clusters at high redshift are forming hierarchically.

The future of structure formation can be predicted using the cosmological constraints that have been derived through observations of supernovae, clusters, and the CMB. Linear structures (i.e. those of small overdensity) will continue to grow until the exponential expansion of the universe halts structure formation. This will happen when $\Omega_m a^{-3} < \Omega_\Lambda$ (Williams, 2003; Rosati, 2004).

When this condition is satisfied, the universal expansion of space will not allow any non-collapsed structure to form, as space will be expanding faster than gravity can attract diffuse mass. Structures that have already formed and virialized, with an overdensity ~ 200 times that of the critical density, will continue to evolve in the non-linear regime.

2.7 Conclusions

Despite having relatively few major mass components, clusters of galaxies are complicated structures. The dark matter, ICM, and galaxies (approximately 85%, 14% and 1% by mass) interact via a number of processes, giving rise to a complicated geometry and history. By using observations of clusters, we may learn how each of these components interact and how the additional intra-component processes affect the global properties of clusters.

Clusters of galaxies are rare objects, only containing $\sim 10\%$ of known galaxies in the visible universe. Also, clusters are the largest bound structures currently at an advanced stage of virial evolution. This makes them sensitive to structure formation scenarios and the relative amounts of matter, dark matter, and cosmological constants. As such, clusters are used to constrain cosmological models.

To date, clusters of galaxies have proved to be an invaluable laboratory for metal enrichment, galaxy evolution, feedback processes, structure formation, etc! Yet, we still do not fully understand clusters: how efficient are energy feedback processes, when did star formation and metal enrichment start, and at what rate did it continue? Clusters are sure to be invaluable in answering these questions, while raising new questions.

2.7.1 Conclusions relevant to the dissertation

This chapter has introduced many concepts used throughout this dissertation, as well as describing the evidence for dark matter. Observations of clusters have placed limits on the dark matter mass distribution and recently the velocity structure.

It is not currently possible to observe dark matter directly. As such, all of our observations are indirect: determined by observing its effects on baryonic mass and radiation.

Classically, the dark matter distribution in clusters was determined by observing the line-of-sight velocity structure of member galaxies. Lensing techniques and X-ray temperature maps now offer alternative methods. Each of these techniques tell us that clusters display a density profile similar to that of the NFW profile.

All of these techniques have problems, though. Dynamically, it is difficult to determine the 3-D galactic velocity dispersion. For lensing, it is difficult to find enough lensed images at a variety of radii to constrain the density profile. Deriving the X-ray de-projected temperature profile can be difficult; also, the ICM may not be in HSE. All of these methods only derive the total mass density; error is introduced when the baryonic matter is removed to reveal the dark matter distribution.

Hope is not lost, however, as none of these methods have reached their prime. Current work continues to improve modeling and observations. The dark matter density profile will become better constrained.

Observing the dark matter velocity structure is even more difficult. Very recently Hansen & Piffaretti (2008) have derived the dark matter dispersion and anisotropy via two cluster observations. To derive these quantities, it was assumed that the dark matter velocities are similar to that of the gas and that the anisotropy is constant with radius. As this technique is still novel, there is much more work that can be done to improve the results. This technique will surely be applied to other clusters and their

model may evolve to determine the anisotropy as a function of radius.

As technology progresses, observations improve. This dissertation may help to predict and explain the observations of the density, velocity dispersion, and velocity anisotropy profiles. Already, there is speculation that we will be able to directly measure the properties of dark matter, including the anisotropy, given that we could observe 10^6 WIMP annihilation events.

In closing, observations of clusters have provided information about the existence and distribution of dark matter. As we still know so little about the kinematic structure, detailed mass distribution, non-linear regime of collapse, or the composition of dark matter, it is apparent that there is still much work to be done. This work focuses our understanding of dark matter by working to understand the simulation results. Thus, when actual observations are made, we may understand their current configuration as well as the evolution that has brought them to their specific final state.

Chapter 3

Semi-analytical dark matter halos

A slightly modified version of this chapter appears in the Astrophysical Journal: Austin, C. G., Williams, L. L. R., Barnes, E. I., Babul, A., Dalcanton, J. J. 2005 ApJ, 634, 756

Abstract

Although N-body studies of dark matter halos show that the density profiles, $\rho(r)$, are not simple power-laws, the quantity ρ/σ^3, where $\sigma(r)$ is the velocity dispersion, is in fact a featureless power-law over ~ 3 decades in radius. In this paper we demonstrate, using the semi-analytic Extended Secondary Infall Model (ESIM), that the nearly scale-free nature of ρ/σ^3 is a robust feature of virialized halos in equilibrium. By examining the processes in common between numerical N-body and semi-analytic approaches, we argue that the scale-free nature of ρ/σ^3 cannot be the result of hierarchical merging, rather it must be an outcome of violent relaxation.

3.1 Introduction

As was discussed in 1.2, there is a broad consensus that collisionless dark matter halos, starting from some realistic matter power spectrum, have a spherically-averaged density profile that is well represented by the NFW prescription (Navarro et al., 1997), or its close variants (Moore et al., 1998; Navarro et al., 2004). Regardless of which density

profile expression proves to best describe N-body halos, the underlying physics that drives the halos to have this shape is not yet fully understood.

Taylor & Navarro (2001) (hereafter TN01) and Hansen (2004), alternatively, studied the quantity $\rho(r)/\sigma^3(r)$, which has the dimensionality of phase-space density (see Section 1.4). TN01 found that ρ/σ^3 of their three halos is very well approximated by a single power-law, from $10^{-2.5}$ virial radii to just beyond the virial radius. This finding is unexpected because the density profile, $\rho(r)$ undergoes a considerable slope change in the same radial interval. The power-law index α, where $\rho/\sigma^3 \propto r^{-\alpha}$, was found to be very similar for all the three halos studied by TN01; $\alpha = 1.875$.

In this chapter we address the following questions: (i) Is the scale-free nature of ρ/σ^3 a result of initial conditions or (ii) an outcome of evolution and virialization.

These questions can be addressed by studying halo formation techniques different from N-body simulations. Halos forming in N-body simulations are subject to a complex set of dynamical processes. Particles can exchange energy and momentum through violent relaxation and two-body encounters (even though the latter are suppressed in cosmological simulations). Additionally, phase-mixing can decrease phase-space density, while preserving particles' energies. These processes are brought about by halo collapse, merging, dynamical friction, etc.

The semi-analytical methods do not incorporate such a wide range of processes. As we describe later in more detail, ESIM halos are spherically symmetric with one spatial and two velocity (radial and tangential) phase-space dimensions. They virialize through violent relaxation, which changes the shells' energies, but conserves the angular and radial momenta of each shell throughout the collapse. There are no mergers or two-body interactions.

Given such different formation scenarios, it is not surprising that the final properties—density distributions, etc.—of N-body and ESIM halos tend to be different. However, if specific final properties are present in N-body and ESIM halos, that strongly suggests that the property is the result of shared physics. This is our premise in addressing question (ii). Specifically, we find that the phase-space density of our halos is well represented by a power-law (Section 3.2), a result similar to the one reached through the study of numerically generated halos. Question (i) is also addressed in Section 3.2, where we vary input conditions of ESIM halos. Again, the power-law nature of ρ/σ^3 does not

seem to be affected by these indicating that the answer to question (i) is negative.

3.2 Extended Secondary Infall Model (ESIM) Halos

3.2.1 Summary of the Method

The collisionless dark matter halos in the present study are formed using an analytical method originally introduced by Ryden & Gunn (1987). The method, including minor extensions, is fully described in Williams et al. (2004b). In summary, halos are spherically symmetric and isolated. We use a flat, matter dominated geometry with $h = 0.5$. The initial power spectra is a standard CDM Harrison-Zeldovich power spectrum normalized such that $\Omega^{0.6}\sigma_8 = 0.5$. Evolution of the power spectrum is dictated by the transfer function given by Bardeen et al. (1986) in their Appendix G. The density profile of a proto-halo is taken to be the profile of a peak in a density field described by this power spectrum, $P(k)$ as is illustrated in Williams et al. (2004b), Figure 9.

In addition to the primary peak, proto-halos have superimposed secondary perturbations, whose properties are derived from the same $P(k)$. In a real halo these secondary perturbations generate random motions of dark matter particles, both radial and tangential. In ESIM halos, the RMS amplitude of random velocities (as a function of radius) are calculated from $P(k)$, as described in Ryden & Gunn (1987), and in the Appendix of Williams et al. (2004b). For each shell the magnitude of the velocity perturbation is chosen from a Maxwell-Boltzmann distribution with the above RMS; the direction is chosen randomly. It has been recently pointed out that the Maxwell-Boltzmann distribution does not describe the particle velocities of equilibrium halos (Kazantzidis et al., 2004; Hansen et al., 2005). However, the Maxwell-Boltzmann distribution is sufficient for our purposes, because we use it to describe the initial pre-collapse, not the final equilibrium halos. Even if the Maxwell-Boltzmann assumption is not strictly correct for the proto halos, it suffices for our purposes, because we use ESIM halos as a simplified tool only; we do not aim to reproduce real halos.

When a particular shell reaches its maximum turn-around radius the perturbation in radial and tangential velocity is added to the existing radial infall velocity. In a real halo these additional random velocities result in dark matter particles having elliptical, precessing orbits. In ESIM halos, the random velocities transform the initially thin

shells into thick, overlapping shells, each with its own apo- and peri-center. A key assumption in ESIM calculations is that the collapse proceeds adiabatically, with each shell conserving its angular and radial momentum. Note that each shell's secondary velocity perturbation is oriented randomly, so that the halo as a whole has zero net angular momentum, and no net rotation. As the collapse proceeds, the mass distribution in the halo changes, and the potential and shells' energies are recalculated after each step in the collapse. This is violent relaxation. To sum up, ESIM halos are formed via smooth accretion of somewhat lumpy material, with no major mergers.

Our method of halo formation has considerable flexibility with direct control over the parameter space of initial conditions. For example, we can change the shape of the primary density peak by smoothing or altering the matter power spectrum. Both the shape of the primary peak and the amplitude of the secondary perturbations are based on $P(k)$, but we can alter the shape of the primary peak and the amplitude of secondary perturbations independently, which gives us another degree of freedom in exploring the resulting final halo profiles. For example, we can change the secondary perturbations—the overall amplitude and radial dependence—while keeping the primary peak unaltered. Even though these changes need not correspond to any astrophysically plausible scenarios, the evolution of ESIM halos proceeds in a physically consistent way.

3.2.2 ESIM Halo Calculation Results

We generate three sets of halos, with 'galaxy,' 'group,' and 'cluster' scale masses. To get different ranges of halo mass we filter the mass power spectrum, prior to normalization, on comoving scales r_h of 0.05, 0.35 and 0.7 Mpc, respectively. Larger r_h mean that the collapse will start later, and more massive halos will form as a result. The initial properties of each of these mass scales are shown in Figure 3.1.

Within each mass set we study the effect of the secondary velocity perturbations on the final halo profiles. To that end, we form halos where the magnitudes of the secondary velocity perturbations are scaled by a parameter, hereafter called the perturbation amplitude scaling parameter, or scaling parameter for short. In this Section the scaling parameter is altered uniformly for a given halo, but in Section 3.2.8 we radially vary it within the halos. A scaling parameter of zero corresponds to no secondary perturbations, in which case the velocities are purely radial. A scaling parameter of 1

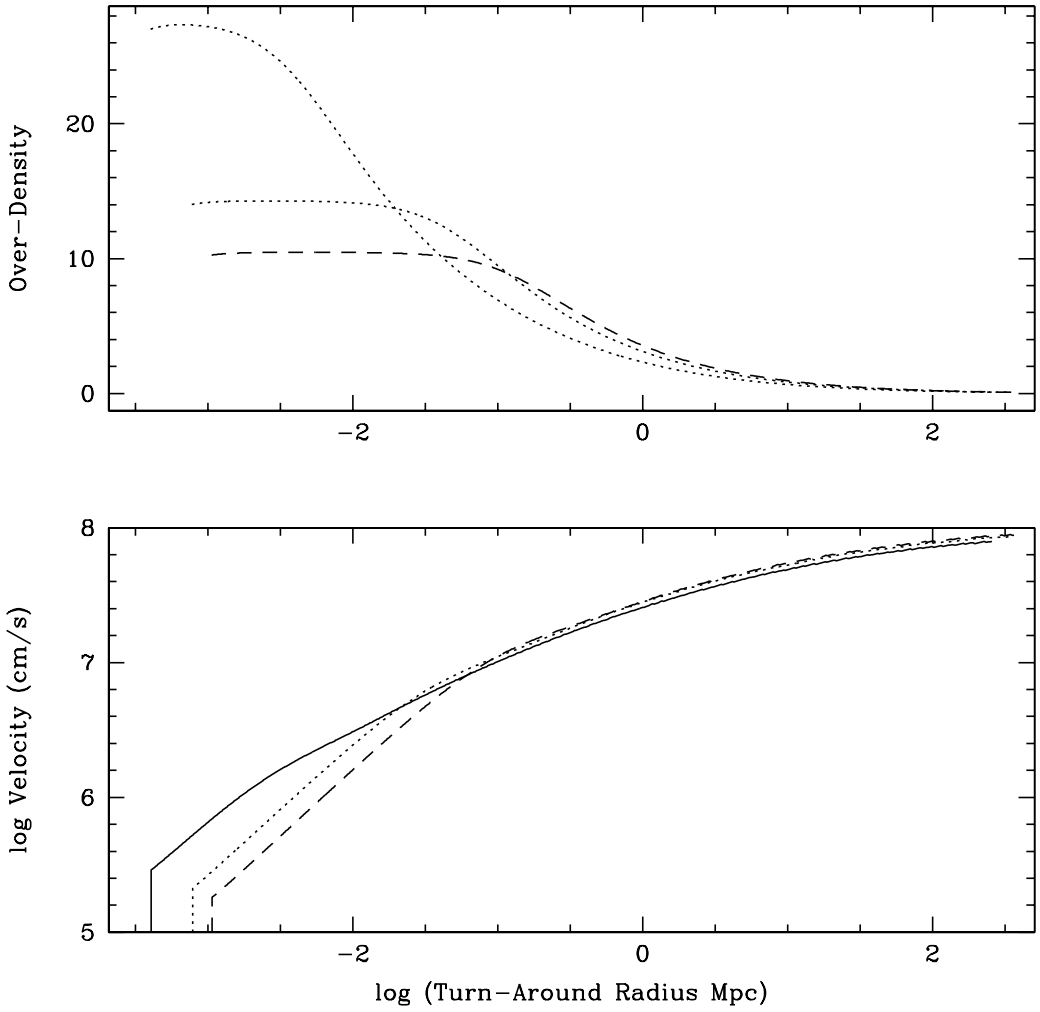

Figure 3.1: This shows how the initial properties vary with the mass categories. Density and velocity as a function of turn-around radius (top and bottom, respectively). The solid line is the galactic initial proprieties, dotted is the group, and dashed line represents the cluster mass scale.

corresponds to the original amplitude of secondary perturbations derived from the same power spectrum that determined the shape of the primary density peak, while setting the scaling parameter to 2 doubles the amplitude of all secondary perturbations.

The perturbation amplitude scaling parameter is varied from 0.4 to 2.5 in increments of 0.05. Because each shell is assigned a velocity perturbation from a distribution extending to $\approx 2.5V_{RMS}$, there is a chance that the shell's kinetic energy will exceed its potential energy. This is especially likely if the scaling parameter is large, and the shell happens to be far from center. In this case, we assume that the shell is instantaneously lost from the halo and is no longer considered in the potential calculations or the kinematic analysis. Each shell's potential energy is calculated based on the mass distribution due to a finite number of shells, with the outermost shells extending well beyond the virialized portion of the halo at the present epoch. The total number of shells, and hence the zero-point of the potential, is fixed such that halos computed using scaling parameters less than 1.5 do not lose any mass during the collapse, while halos with a scaling parameter of 2 lose at most 25% of their final mass.

Each ESIM halo is unique since the secondary velocities for each shell are picked randomly from a distribution. To reduce the dispersion in the final halo properties the halos presented here are averages of ten individual halos. To verify the reliability of the results two sets of averaged halos were computed for each scaling parameter. In all cases our analysis applies to the portion of each halo between $10^{-2.0}$ and 1 virial radius, r_{200}, the radius at which the average enclosed halo density is 200 times the critical, $\rho_o = 2.77 \times 10^{11} h^2 M_\odot \; Mpc^{-3}$. As mentioned earlier, we use a standard cold dark matter model. While this model is not the currently favored one, the particular cosmological model used has a minimal effect on the final halo properties of interest.

In the following sections we describe the various properties of the final virialized ESIM halos. In Sections 3.2.3-3.2.6 we discuss in detail the properties of galaxy mass halos. Since the qualitative properties and the general trends are similar for galaxy, group, and cluster mass halos, we do not discuss the latter two specifically, but present a summary of their properties in Section 3.2.7.

3.2.3 Density profiles

Figure 3.2 shows four halo density profiles, expressed in units of critical density ρ_o, and multiplied by $(r/r_{200})^2$ This is done in order to accentuate features in the density profiles. All halos were generated using the galaxy-mass $P(k)$ filtering scale $r_h = 0.05$Mpc. The standard case, a halo with a scaling parameter of 1, is shown in the bottom-left panel. Panels top-left, top-right, and bottom-right show halos with scaling parameter of 0.4, 0.6 and 2, respectively.

As in Williams et al. (2004b), the ESIM halos differ from those in N-body simulations. For convenience, NFW density profiles, $\rho(r) \propto (r/r_s)(1 + r/r_s)^2$ (Navarro et al., 1997), where the concentration parameter is $c = r_{200}/r_s$, are over-plotted as long dash lines. ESIM density profiles are better approximated by a single power-law between $r = 10^{-2.0} r_{200}$ and r_{200} than the NFW profiles.

The effects of changing the amplitude of secondary perturbations on the density profile can be seen in the four panels of Figure 3.2, and is summarized in panel A of Figure 3.3, which plots γ_{fit}, the fitted density profile slopes, vs. scaling parameterand Figure 3.4 which illustrates how γ_{fit} is related to the final halo mass. As expected, the halos with larger secondary perturbations, and hence more angular momentum have shallower density profiles. (Note that the steepest central cusp slope of ESIM halos is $\gamma = -2$, as explained in Section 5.1 of Williams et al. (2004b).) To further characterize the density profiles we calculate the radii where the slope, $\gamma_{fit} = (d \log \rho)/(d \log r)$, attains the values of -1, -2, and -3. We denote these radii by $r_{\gamma=-1}$, $r_{\gamma=-2}$, and $r_{\gamma=-3}$. The dependence of these radii w.r.t. the scaling parameter is shown in panel D of Figure 3.3. The values of $r_{\gamma=-1,-2,-3}$ increase with the scaling parameter, consistent with the density profiles becoming shallower as the angular momentum content of the halos increases.

3.2.4 Velocity dispersion and velocity anisotropy

Since many shells overlap at any given radius, the total velocity dispersion profile is calculated as the mass-weighted RMS value of the radial and tangential velocity dispersions of all the shells that exist at that radius. Figure 3.5 shows the velocity dispersion

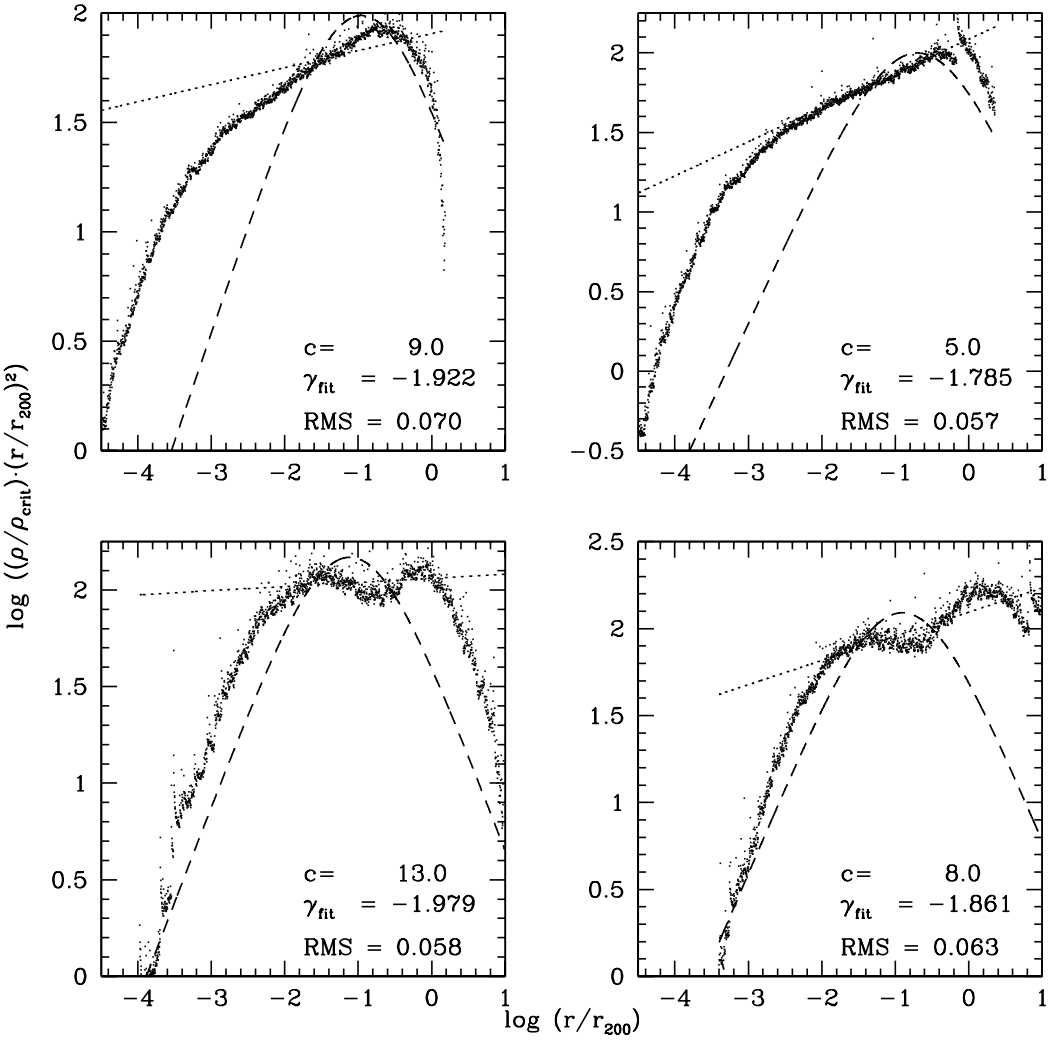

Figure 3.2: Density vs. radius for galaxy-mass halos generated with $r_h = 0.05$Mpc, and scaling parameters of 0.4, 0.6, 1, and 2 (top-left, top-right, bottom-left, and bottom-right). Density is expressed in units of the critical density and multiplied by $(r/r_{200})^2$; this accentuates deviations from the fits. The slope and RMS of the power-law fit (dotted line), $-\gamma_{fit}$, is noted in each panel. The NFW profile is over-plotted as a dash line; the NFW concentration parameters are shown. All fits were calculated using the density profile between 10^{-2} and 1 virial radii.

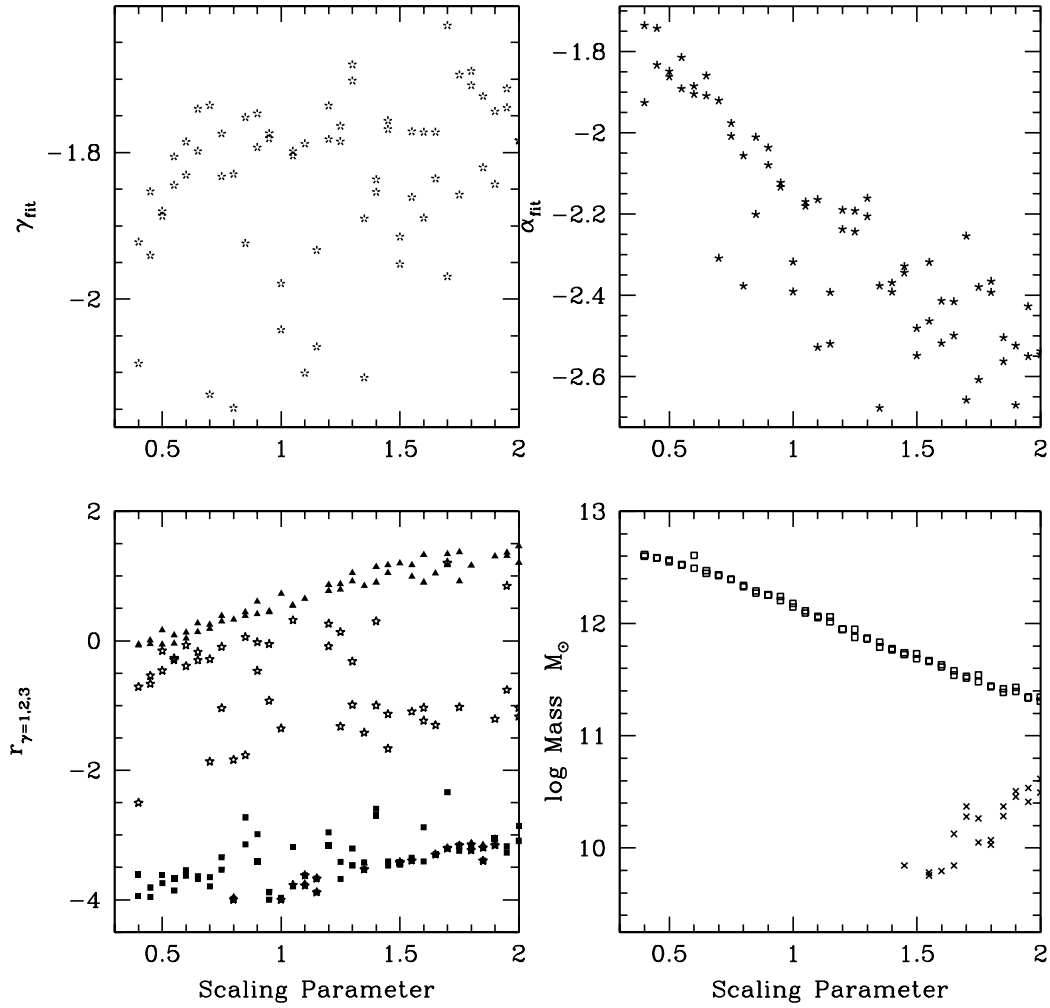

Figure 3.3: The final properties of galaxy-mass halos with $r_h = 0.05$Mpc as as a function of the perturbation amplitude scaling parameter. Top-left: Slope of the log-log density profile, γ_{fit}; Top-right: Slope of the log-log ρ/σ^3 profile, α_{fit}; Bottom-left: The radius where the logarithmic density slopes attain the values of -1, -2, and -3, respectively: $r_{\gamma=1}$, $r_{\gamma=2}$, and $r_{\gamma=3}$. Bottom-right: Virial mass of the halo (squares) and amount of mass lost during formation (crosses). Note that as the amplitude of secondary perturbations is increased, the resulting halos have shallower density slopes (top-left and bottom-left) due to increased angular momentum, steeper phase-space density slopes (top-right), and more mass loss (bottom-right) due to the increased probability of matter reaching escape velocity.

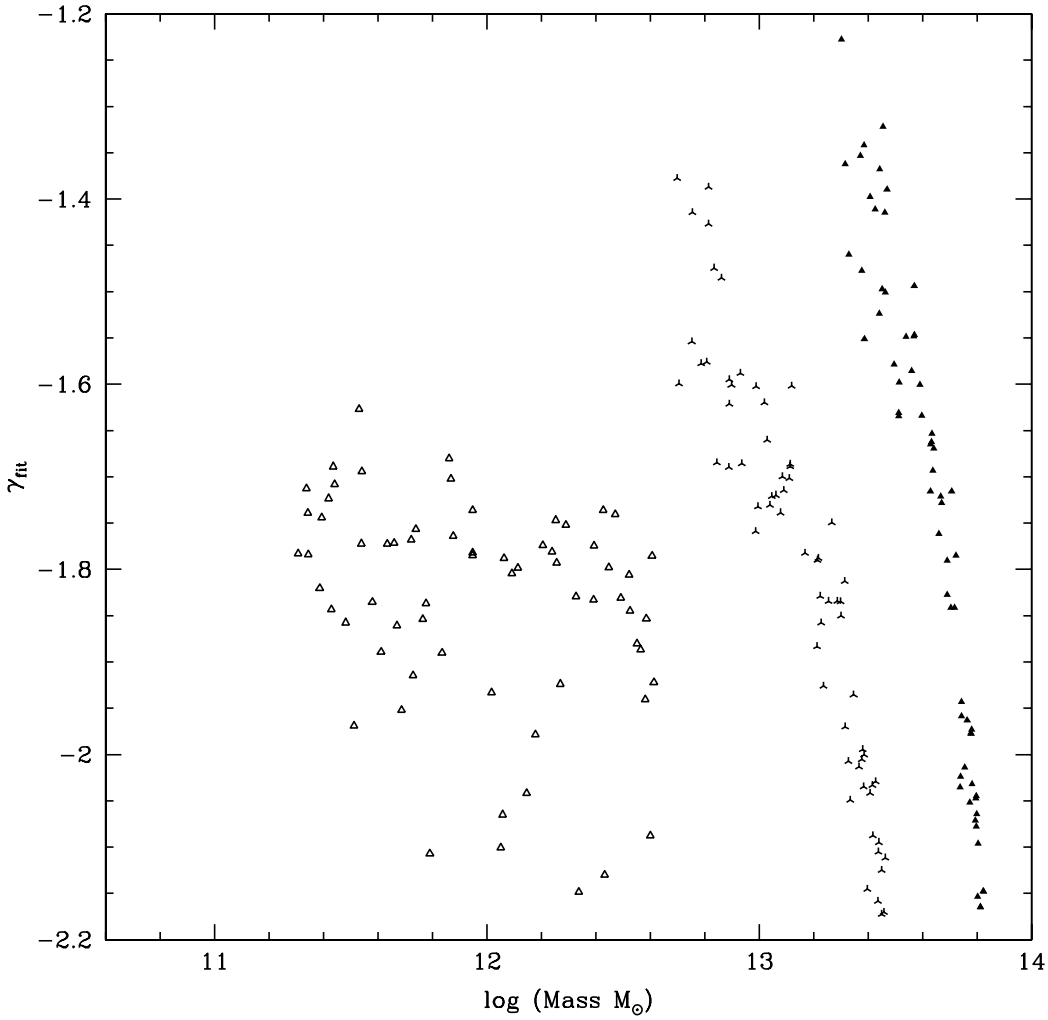

Figure 3.4: The logarithmic density slope as a function of the virial halo mass, for three mass categories (galactic: open triangles, group: starred triangles, and cluster: filled triangles).

profiles for the halos presented in Figure 3.2. Figure 3.5 also shows the velocity dispersion anisotropy, β, which describes the relative directions of the velocity dispersions (Binney & Tremaine, 1987),

$$\beta \equiv 1 - \frac{\sigma_\theta^2}{\sigma_r^2}. \tag{3.1}$$

Except for halos generated using small scaling parameter values, $\lesssim 1$, the anisotropy parameter stays close to 0 between $\sim 10^{-3}$ and ~ 1 virial radii. For the standard halo, the average velocity anisotropy parameter is $\beta \sim 0.1$. In general, a halo's average β increases with decreasing scaling parameter: smaller secondary perturbations imply less angular momentum, and hence more radial orbits. In the limit of perturbation amplitude scaling parameter of 0, purely radial orbits will result.

In Figure 3.6, we show the dependence of the velocity dispersion anisotropy with respect to the density slope, γ_{fit}. This relation has been presented for N-body simulations by Hansen & Moore (2004). They have found that there is a tight, linear correlation between β and γ irrespective of the considered models. ESIM halos do not display this correlation. One possible explanation for this difference between ESIM and N-body halos is that ESIM formalism does not allow the onset of the radial orbit instability, which may be key in forming $\beta - \gamma$ correlation in N-body halos (Barnes et al., 2005).

3.2.5 Phase-space density

The phase-space density profiles of the halos displayed in Figure 3.2 are shown in Figure 3.7. ESIM halos appear to have nearly scale-free distribution of ρ/σ^3 extending over $2 - 4$ decades in radius, interior to the virial radius. Aside from the very central and outer regions (which we will return to shortly), the ρ/σ^3 profiles are fit by power-laws better than the corresponding density profiles. For example, between $10^{-2.0}$ and $10^{-3.5}$ virial radii the density profile of the halo with the scaling parameter of 1.0 (bottom-left panel) is becoming shallow rapidly, but ρ/σ^3 is still well fit by the same slope that characterizes larger radii.

To understand why ρ/σ^3 deviates from a power-law at large and small radii we have to consider the equilibrium state of halos. Binney & Tremaine (1987), under the assumptions of spherical symmetry and a non-rotating system, rewrite the Jeans

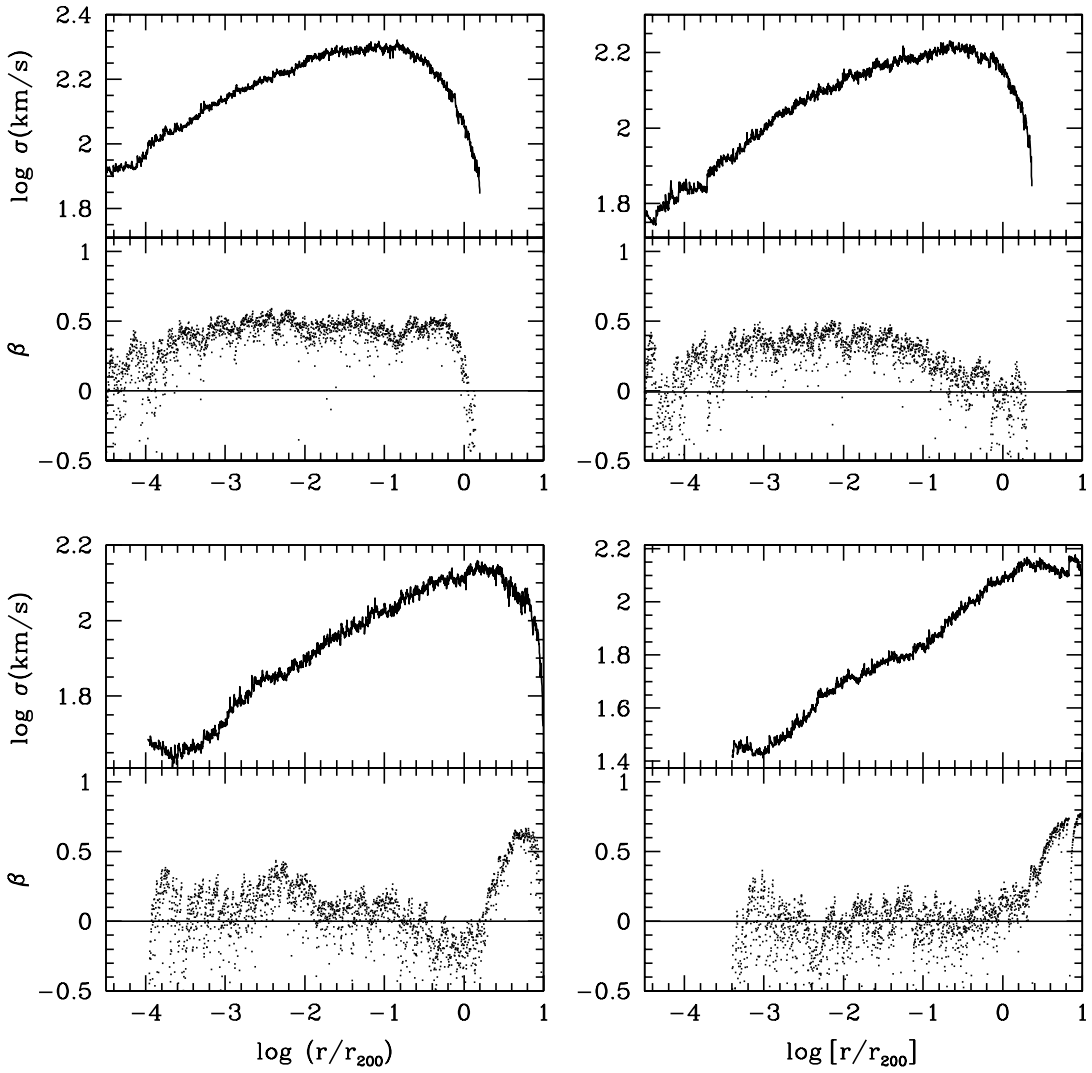

Figure 3.5: The top half of each of the four panels shows the RMS velocity profile for halos with perturbation amplitude scaling parameters of 0.4 (top-left), 0.6 (top-right), 1.0 (bottom-left), and 2.0 (bottom-right). The lower half of each panel shows the velocity dispersion anisotropy, β. Low scaling parameter halos have somewhat radial velocity anisotropies, while higher scaling parameter halos have nearly isotropic velocity dispersions up to the virial radius.

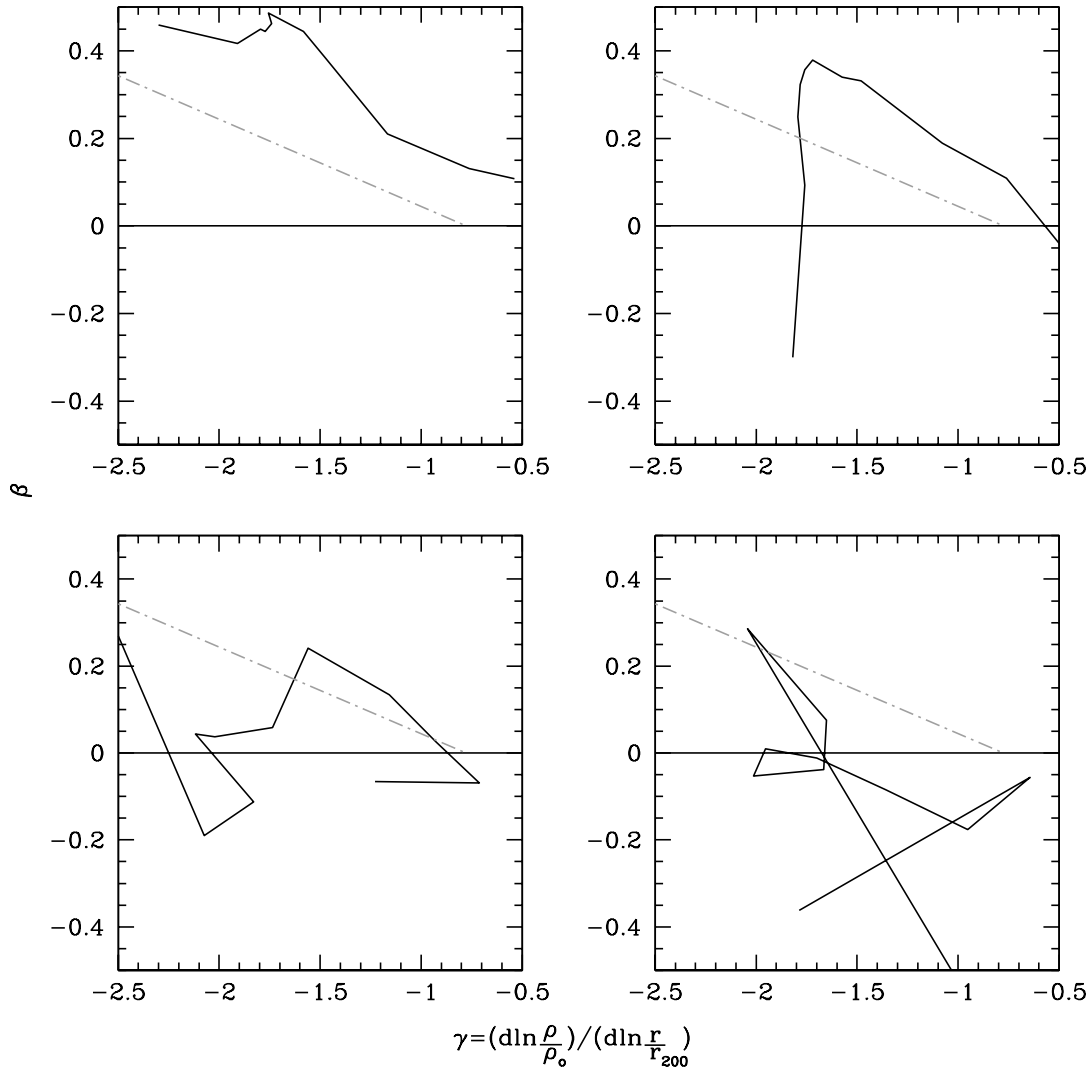

Figure 3.6: The anisotropy parameter (β) vs. the density slope (γ_{fit}) relationship for ESIM halos with scaling parameters of 0.4, 0.6, 1, and 2, respectively. The points were binned into sets of 170 points to reduce noise and reveal the overall trend. The dot-dash line indicates the relationship found by Hansen & Stadel (2006).

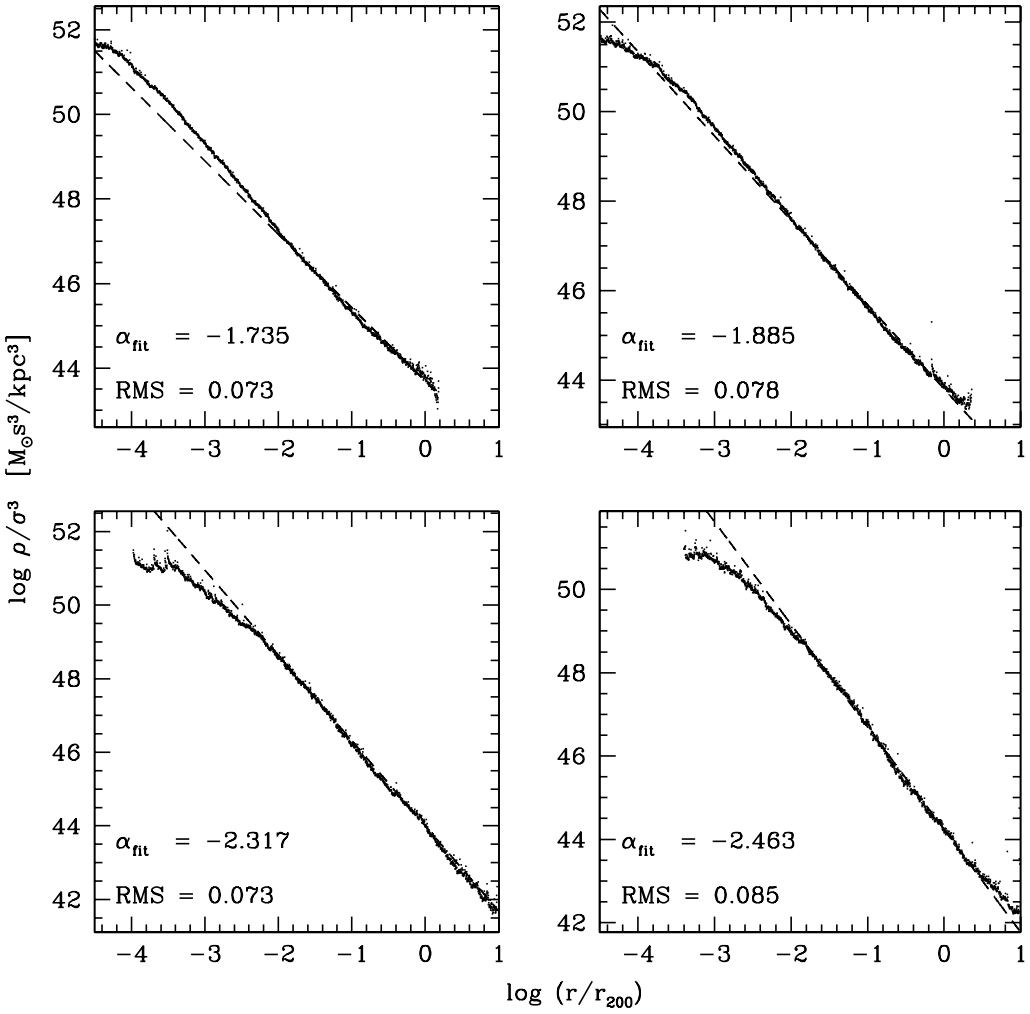

Figure 3.7: The phase-space density profiles of halos with perturbation amplitude scaling parameters of 0.4 (top-left), 0.6 (top-right), 1 (bottom-left), and 2 (bottom-right). The ρ/σ^3 data have been normalized to a power-law fit between $10^{-2.0}$ and 1 virial radius. The value of the power-law index fit is indicated in each panel as α_{fit}. Also, the slope of the ρ/σ^3 profiles from r/r_{200} of $[10^{-2.0}, 10^{-2}]$ and $[10^{-0.5}, 1]$ are noted as α_{low} and α_{high} for comparison. Note the nearly scale-free behavior for 2-3 decades in radius.

equation as

$$\frac{1}{\rho}\frac{d(\rho\sigma_r^2)}{dr} + 2\frac{\beta\sigma_r^2}{r} = -\frac{d\phi}{dr}. \tag{3.2}$$

In Figure 3.8, the LHS of equation 3.2 (i.e. the pressure gradient plus the anisotropy term) is plotted at each radius, while the RHS, the potential gradient, is shown as the smooth curve. Hydrostatic equilibrium is satisfied when the points follow the curve. This is the case in panels top-left, top-right, and bottom-left; in panel bottom-right there is a lot of scatter in the points that represent the LHS of Equation 3.2, and so the equilibrium condition is not well satisfied. This apparently results in ρ/σ^3 being only marginally well approximated by a power-law. In panels top-left, top-right, and bottom-left, the hydrostatic equilibrium breaks down outside of the virial radius, which apparently leads to a break in the scale-free behavior of ρ/σ^3at the same radius.

Figure 3.8 also helps to explain why ρ/σ^3 breaks away from a power-law at small radii. At small radii, the potential gradient scales as $1/r^2$. This is due to the presence of a compact inert core at the center of every ESIM halo. As described in Williams et al. (2004b) (Sections 4.1, A.1, A.5), ESIM halos have finite mass resolution. At the center of each halo the smallest resolvable mass is represented by an inert core, which provides the initial 'seed' for ESIM calculations. The inert core does not evolve, i.e. its mass distribution does not change as the halo collapses. Because the part of the halo where the core dominates is not subject to the same dynamical evolution as the rest of the halo, that part should not be considered in the analysis. In all panels of Figure 3.8 the regime of core domination begins roughly at 10^{-4}, $10^{-3.5}$, 10^{-3}, and $10^{-2.0}$ virial radii, respectively. The corresponding panels of Figure 3.7 show that these radii coincide with the break in the scale-free nature of ρ/σ^3.

Excluding the innermost and the outermost regions of halos, the remaining portions are well represented by power-laws (this is further illustrated in Section 3.2.7 and Figure 3.11 below). Figure 3.7 demonstrates that the scale-free nature of ρ/σ^3 is resilient: it persists despite the changes in the magnitude of the secondary perturbations, at least in the range 0.5-1.5. However, the power-law index, $\alpha = (d\log\rho/\sigma^3)/(d\log r)$, is not constant; in general, α_{fit} increases with increasing scaling parameter (see panel B of Figure 3.3).

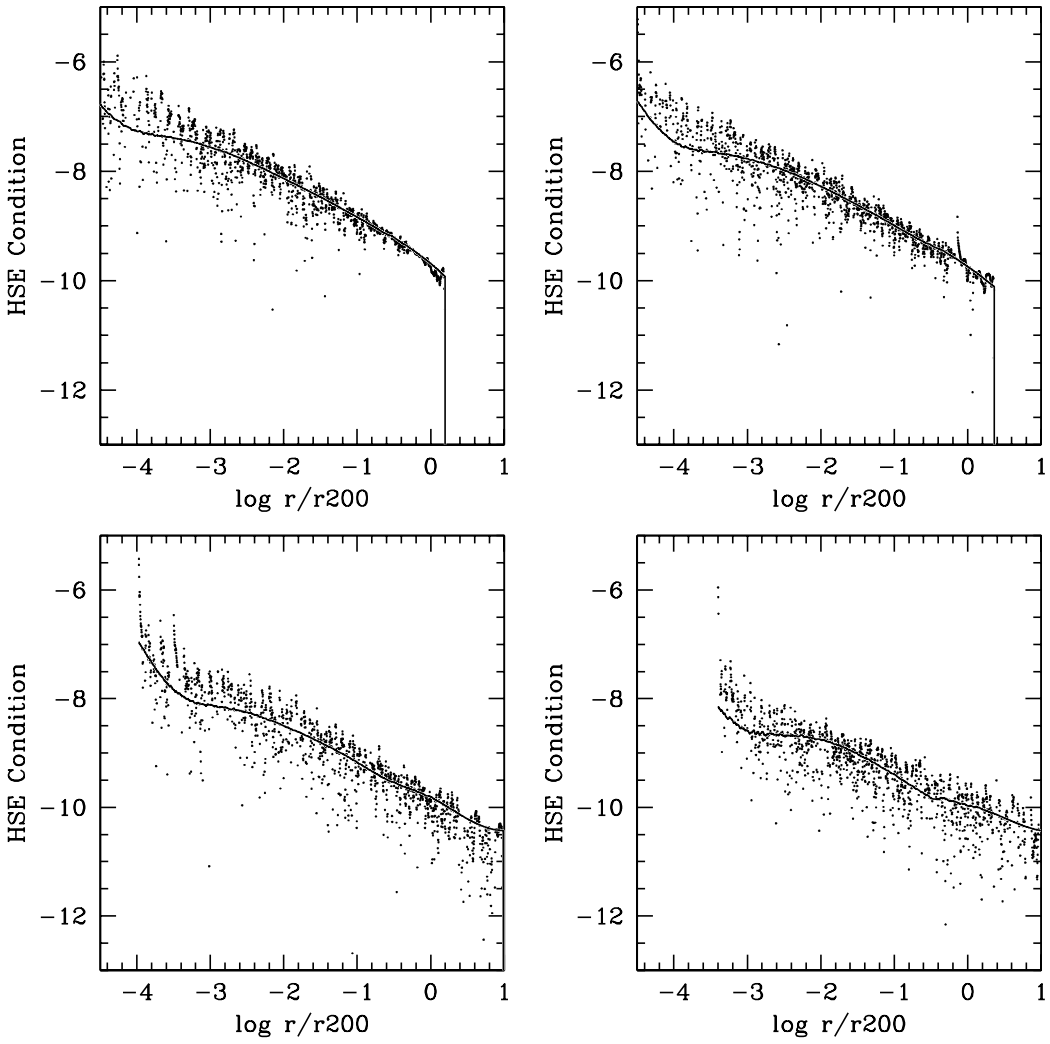

Figure 3.8: The hydrostatic equilibrium (HSE) condition: the LHS and RHS of equation 3.2 are shown as points and the smooth curve, respectively. Panels top-left, top-right, bottom-left, and bottom-right represent halos with scaling parameters of 0.4, 0.6, 1, and 2, respectively. Where the line traces the plotted points, the halo is in hydrostatic equilibrium.

3.2.6 Halo mass

The bottom-right panel of Figure 3.3 shows that the mass of virialized halos, for a given power spectrum filtering length ($r_h = 0.05$ Mpc for these halos), decreases steadily as the perturbation amplitude scaling parameter increases. Large secondary perturbation amplitude implies a more extended mass distribution, and smaller virial masses. Additionally, if the shells' energy reaches the threshold to cause mass loss, the final mass is reduced further. However, this effect is negligible for most halos: there is no mass loss during formation for halos with the scaling parameter less than about 1.5.

3.2.7 ESIM halos of groups and cluster masses.

So far, we have discussed how the properties of galaxy-mass halos ($r_h = 0.05$Mpc) change with the changing amplitude of secondary perturbations. Group and cluster-mass halos, generated using power spectrum filtering lengths of $r_h = 0.35$ and 0.7Mpc, respectively, behave similarly. The overall trends for these two cases are summarized in Figures 3.9 and 3.10, which are similar to Figure 3.3.

Two examples are shown in Figure 3.11, for $r_h = 0.35$Mpc (left column) and $r_h = 0.7$Mpc (right column); both halos have scaling parameter of 1.0. It is apparent that larger r_h values result in density profiles that are not as well described by a single power-law, as smaller r_h halos. This is further illustrated in the bottom-left panels of Figure 3.9 and 3.10; $r_{\gamma=1}$, $r_{\gamma=2}$ and $r_{\gamma=3}$ are closer together than in galaxy-mass halos, implying that the density slope changes more rapidly with radius.

Despite the non power-law behavior of the density profile, the phase-space density profile, ρ/σ^3, remains a power-law for at least 2-3 decades in radius interior to r_{200} (third row of Figure 3.11). These panels also show that the scale-free nature of ρ/σ^3 breaks down interior to $10^{-3.5} - 10^{-3}$, where the inert core begins to dominate the potential (the fifth row of Figure 3.11). The same behavior was noted in the case of galaxy-mass halos, in Section 3.2.5. The best-fit slope α_{fit} decreases with the scaling parameter for a fixed r_h, but gets consistently larger with increasing r_h.

Figure 3.12 depicts the dependence of the ρ/σ^3 power-law slope, α_{fit} on the virial mass for all three sets of halos: $r_h = 0.05$ Mpc (open triangles), $r_h = 0.35$ Mpc (starred triangles), and $r_h = 0.7$ Mpc (filled triangles). The main conclusion from Figure 3.12

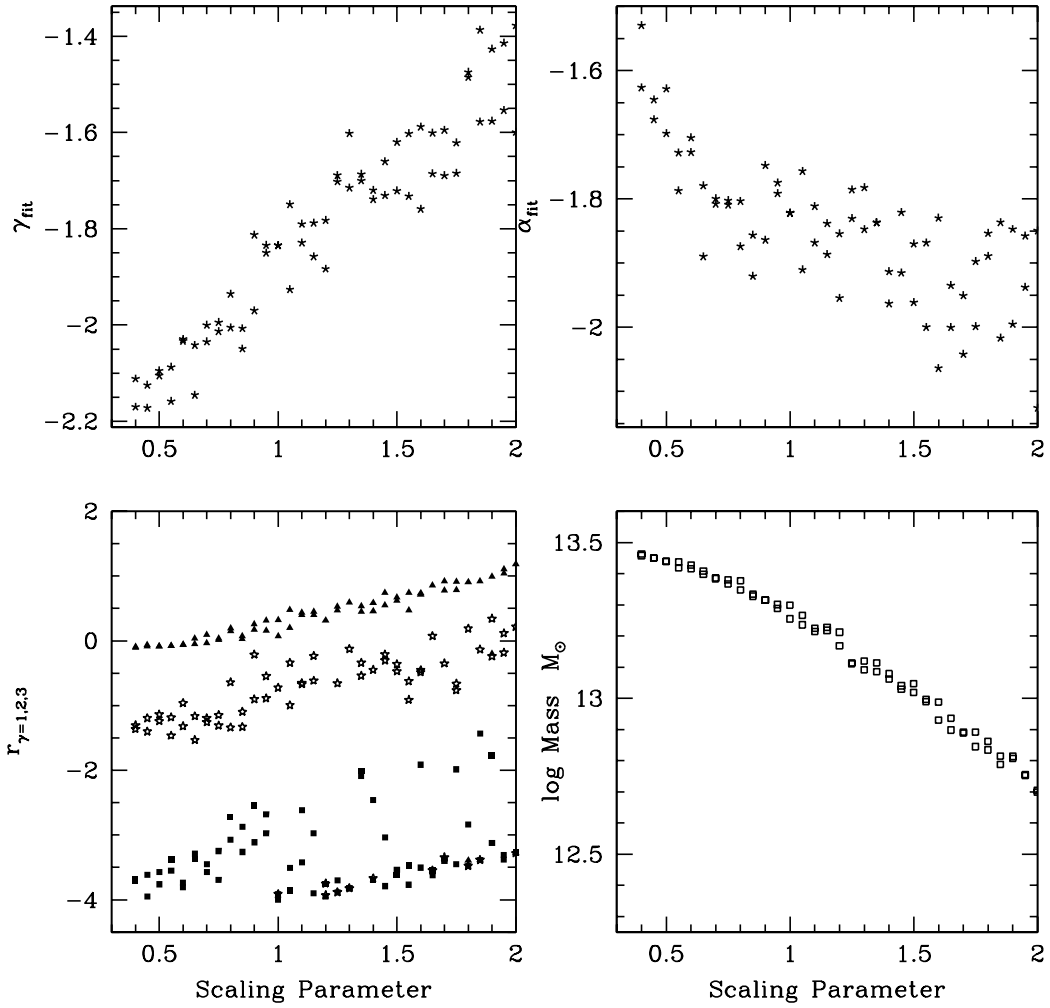

Figure 3.9: Same as Figure 3.3, but for group-mass halos with $r_h = 0.35$Mpc.

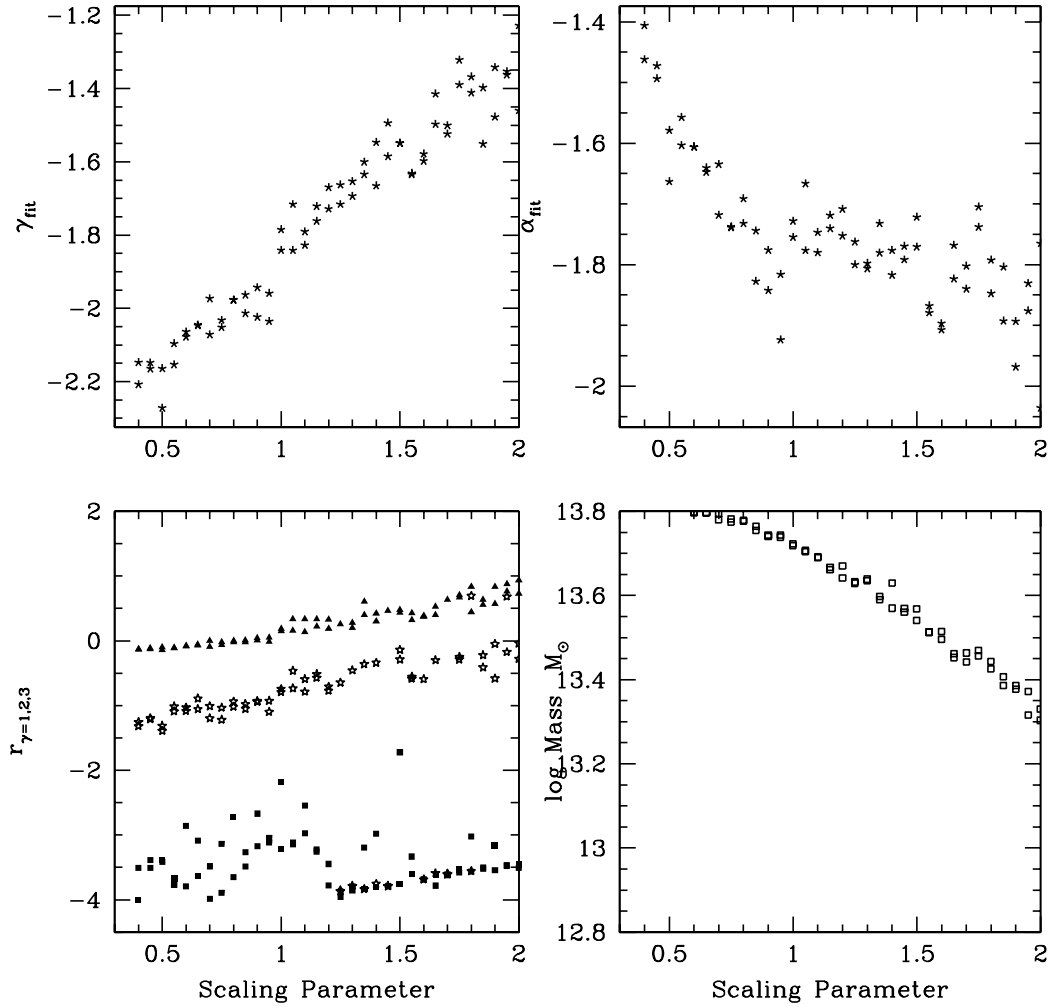

Figure 3.10: Same as Figure 3.3, but for cluster-mass halos with $r_h = 0.7$Mpc.

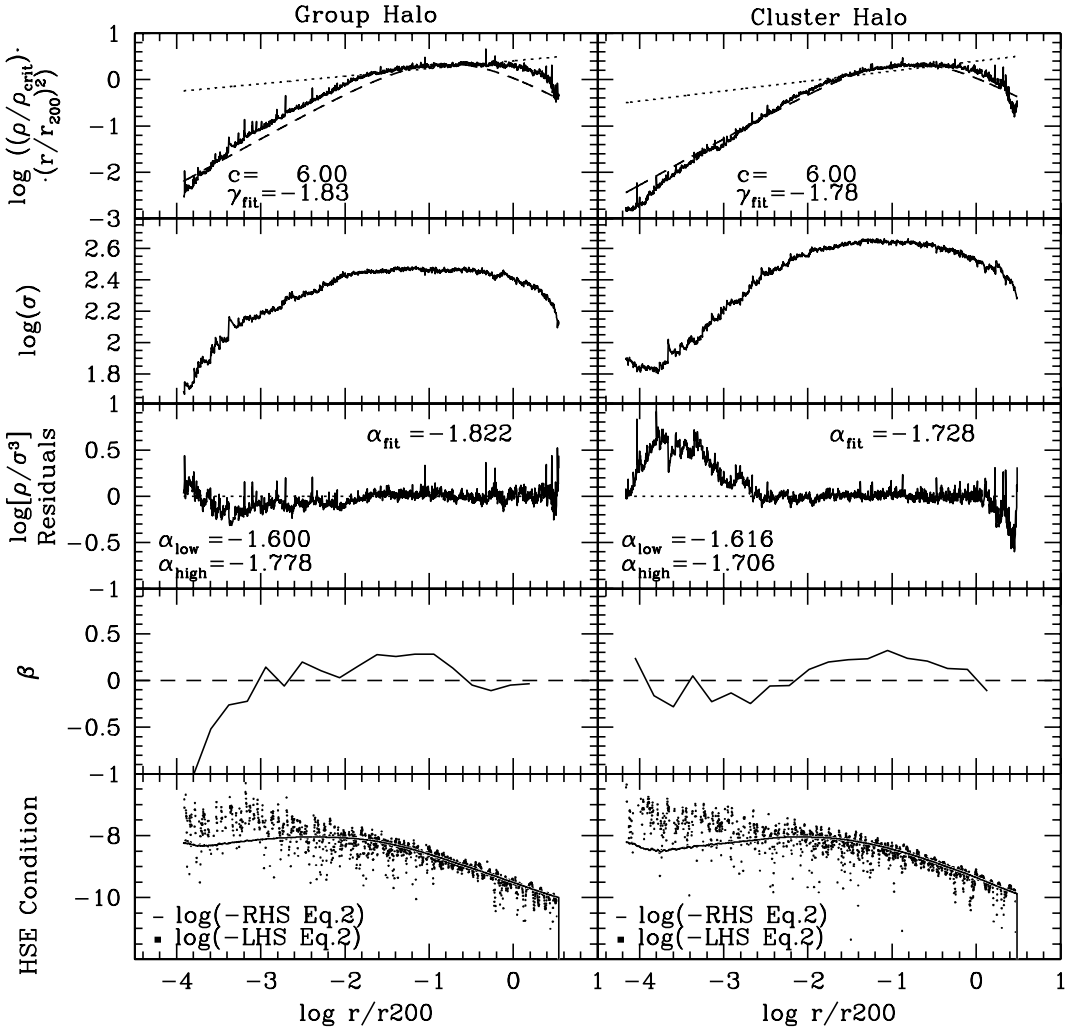

Figure 3.11: Profiles of two halos, both having scaling parameter of 1.0, generated with r_h = 0.35Mpc (right column) and r_h = 0.7Mpc (left column). Shown, from top to bottom, are the density profiles with the NFW formula over-plotted as a long dash line, the RMS velocity dispersion, the velocity anisotropy β, the phase-space density, and the equilibrium condition, showing the LHS (points) and the RHS (smooth curve) of Equation 3.2. Again, the values of γ_{fit}, α_{fit}, α_{low}, and α_{high} are noted in the appropriate panels. Note that the phase-space density profiles are well fit by power-laws, while the density profiles are not.

is that α_{fit} is not uniquely determined by any single halo property, such as mass, perturbation amplitude scaling parameter, or r_h.

Additionally, we show the $\beta - \gamma$ relationship for these two halos in Figure 3.13. These halos show much more agreement with the results of Hansen & Stadel (2006) than the galaxy-sized halos. Despite this, ESIM does not show a linear relationship in this plane, nor does the description hold over the entire radial range.

3.2.8 Testing the Resiliency of the ρ/σ^3 Power-law

Since the halos considered in previous sections exhibit a near-perfect power-law in ρ/σ^3, we wish to determine what would be required to break this resilient behavior. To that end, we generate halos with different scaling parameters assigned to blocks of shells. These changes are not meant to mimic realistic situations, but rather to push our simulations to unphysical extremes. In several trials we increased or decreased the scaling parameter linearly with radius; in other trials, we assigned the inner 5-15% of radii a larger perturbation amplitude scaling parameter of 5, 20, or 50, with smaller scaling parameters assigned to outer shells.

The halos with the scaling parameter assigned linearly in radius (with no large discontinuities) display the power-law in ρ/σ^3. However, halos in the trials with the 'excited sections' (blocks of shells with large scaling parameters) had a ρ/σ^3 profile that showed deviations from a power-law behavior. Figure 3.14 shows the specific halo where all the shells were assigned a scaling parameter of 0.9, except for those with an initial comoving radius between 0.59 and 0.79 Mpc, which were assigned a scaling parameter of 5. The last shell to collapse in this evolution had a comoving radius of 1.92 Mpc. Visual inspection of the top-left and top-right panels show that, even though these halos have been subjected to radially discontinuous changes in the amplitude of the secondary perturbations, the final density and velocity dispersion profiles still appear well behaved, but the deviations of ρ/σ^3 from a power-law are evident. This and other similar trials illustrate that one must adopt extreme measures—large discontinuities in the scaling parameter—in order to break the scale-free nature of the phase-space density profile.

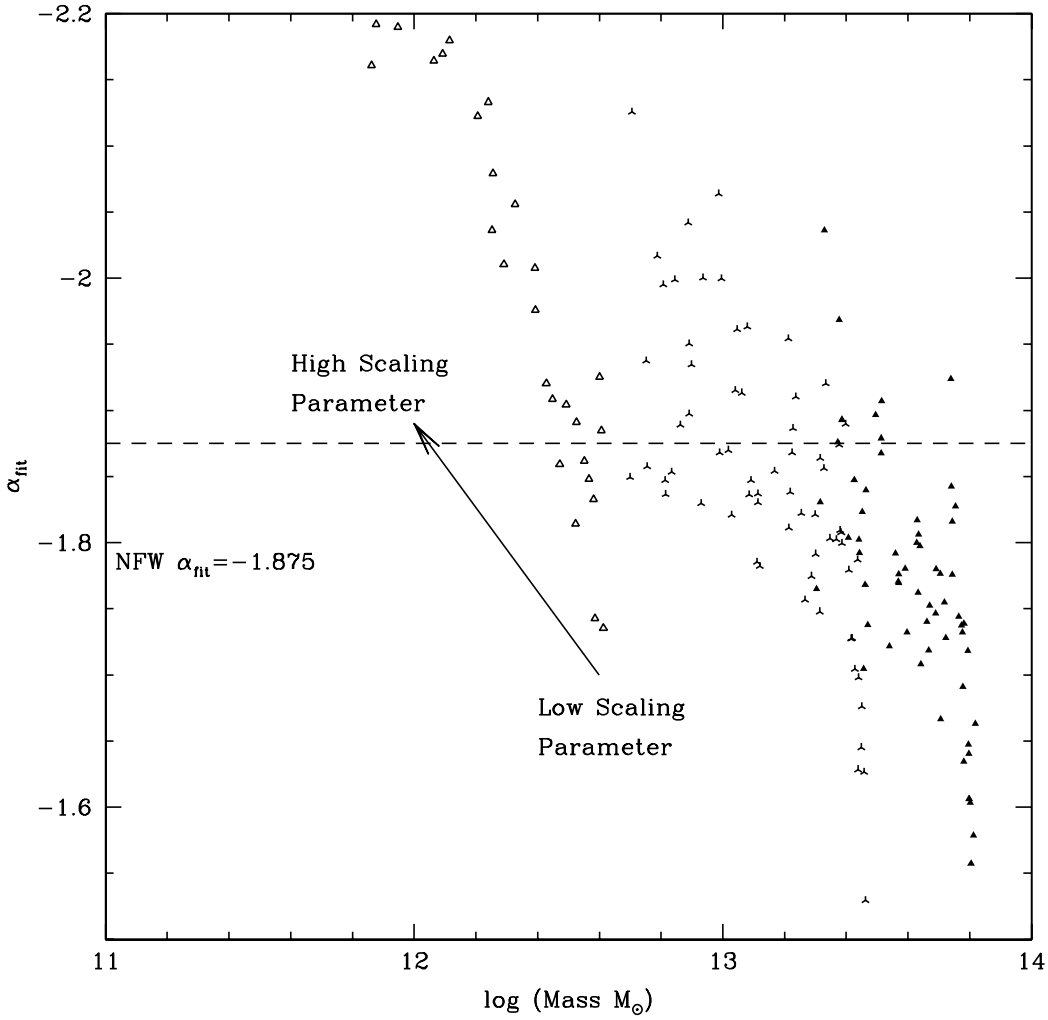

Figure 3.12: The double logarithmic slope, α_{fit}, of ρ/σ^3 vs. radius, as a function of the virial halo mass, for three different $P(k)$ filtering scales, $r_h = 0.05, 0.35$ and 0.7Mpc (open triangles, starred triangles, and filled triangles). Note that α_{fit} is not uniquely determined by halo mass, amplitude of secondary perturbations, halo filtering scale, etc.

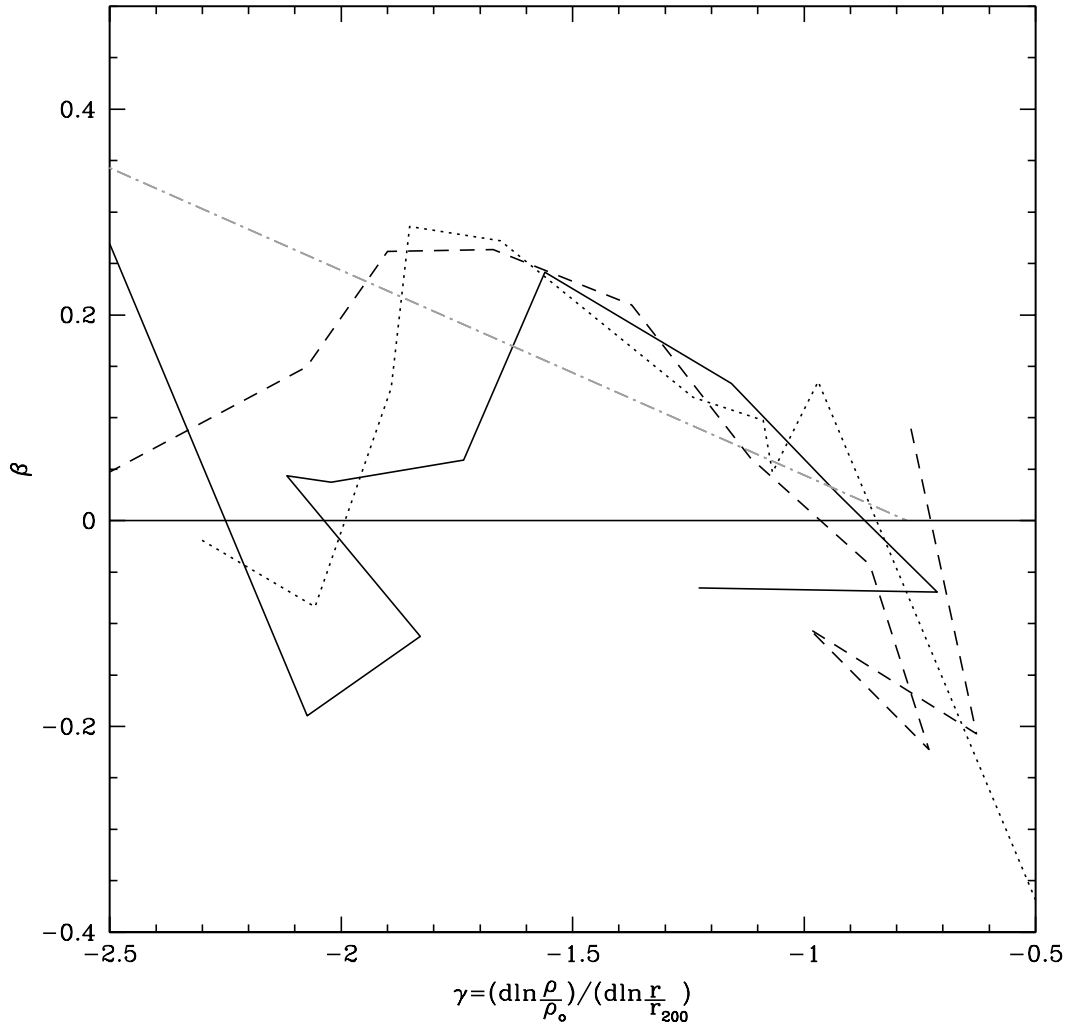

Figure 3.13: The anisotropy parameter β vs. the density slope γ_{fit} relation for the galaxy-sized halo (solid line), the group-sized halo (dotted line), and the cluster-sized (dashed line) ESIM halos The points were binned into sets of 170 points to reduce noise and reveal the overall trend. The dot-dash line indicates the relationship found by Hansen & Stadel (2006).

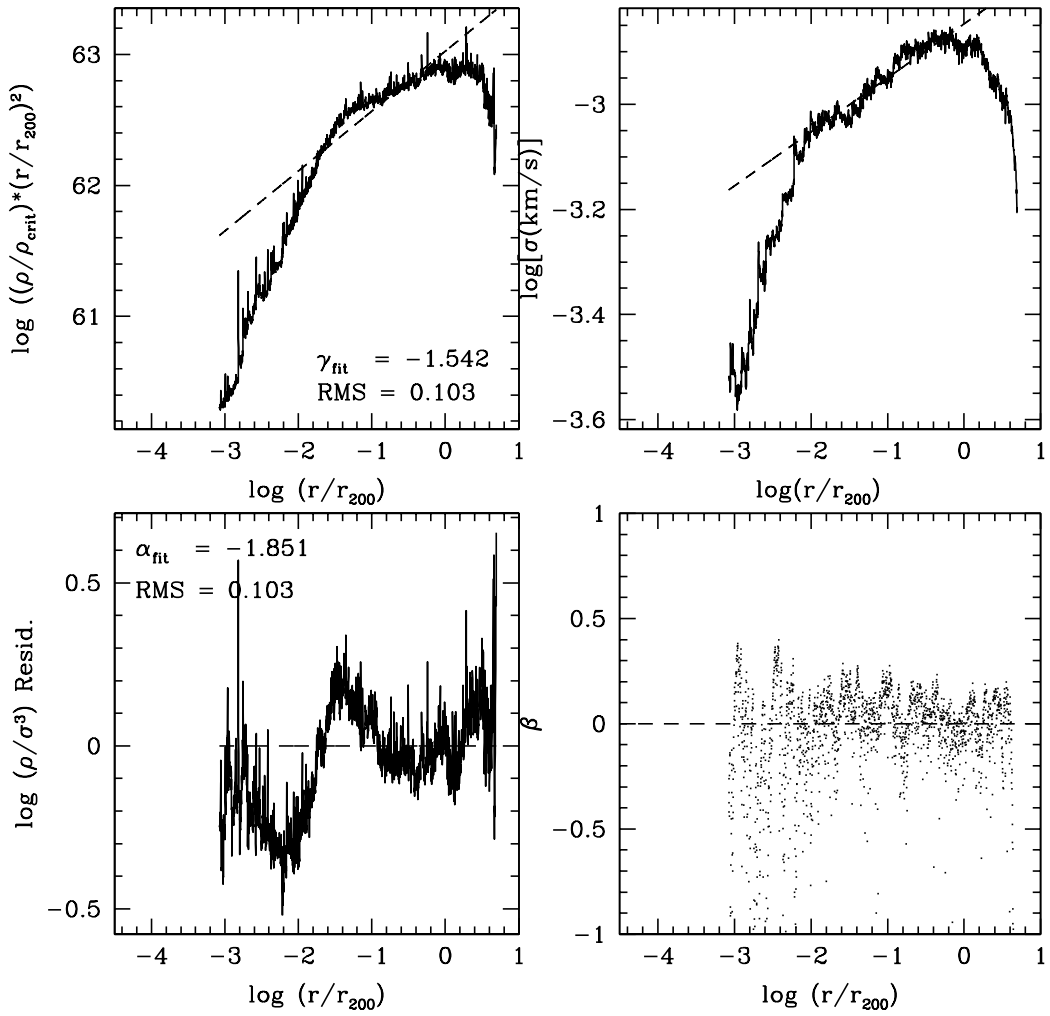

Figure 3.14: An example of a halo with discontinuous perturbation amplitude scaling parameters: shells with the initial comoving radii between 0.59 and 0.79 Mpc were assigned a scaling parameter of 5, while the rest of the halo (up to the last shell at 1.92 Mpc) were assigned a scaling parameter of 0.9. Top-left: Density profile, normalized to a power-law fit between r/r_{200} of $10^{-2.0}$ and 1; Top-right: RMS velocity dispersion profile in km/s; Bottom-left: Phase-space density profile, normalized to its power-law fit; Bottom-right: Velocity dispersion anisotropy profile, β.

3.2.9 Conclusions from ESIM Halos

The ESIM formalism provides us with a simplified, but physically self-consistent way of generating collisionless dark matter halos. It is very different from *N*-body simulations. In the preceding sections we described ESIM halo properties in detail, pointing out that the density profiles are generally different from those produced in *N*-body simulations. By changing the initial conditions we produced a range of density profile types: by filtering the mass power spectrum on small scales ($r_h = 0.05$Mpc) to simulate galaxy-mass halo formation, we ended up with density profiles that showed virtually no change in slope over 2-3 decades in radius inside of the virial radius (Figure 3.2). Larger filtering scales ($r_h = 0.35$ and 0.7 Mpc) aimed to produce group and cluster-mass halos resulted in more curved density profiles (Figure 3.11).

The most important conclusion of Section 3.2 concerns the phase-space density profile, ρ/σ^3. Despite the differences in methods and density profile shapes, one feature was shared by all ESIM halos and *N*-body simulated halos: the power-law nature of the ρ/σ^3 profile. We have shown that this feature of ESIM halos is very resilient, and one must concoct rather extreme cases in order to end up with ρ/σ^3 that shows deviations from a single power-law (Section 3.2.8). There are no models in astrophysics literature that provide a physical explanation for this feature of virialized halos. We argue that the scale-free nature ρ/σ^3 cannot be uniquely characteristic of hierarchical merging because ESIM halos do not undergo mergers. We speculate that it is a generic consequence of the one dynamical process which is common to both ESIM and *N*-body halo formation—violent relaxation, i.e. global changes in the potential, and the accompanying changes in particle energies brought about by the collapse.

Our results concerning α, the double logarithmic slope of ρ/σ^3 vs. radius, are different from those of TN01. We find a range of values from -1.6 to -2.2, while TN01 find that the same $\alpha = -1.875$ described all three of their *N*-body halos. It is possible that the latter finding is due to a small number of halos studied. In our study, α_{fit} was not uniquely determined by any single property of halos, such as mass, epoch of formation, or amplitude of random velocities.

3.3 Conclusions

Examination of a handful of *N*-body dark matter halos indicates that the phase-space density, ρ/σ^3, is a power-law in radius, even though the density profile is not (Taylor & Navarro, 2001). To determine if the scale-free nature of ρ/σ^3 is peculiar to *N*-body halos (may be even just those presented in TN01), or is a more generic outcome of collisionless gravitational collapse, we turned to a different method of generating equilibrium halos. The Extended Secondary Infall Model (ESIM) halo formation, which we presented in Section 3.2, proceeds very differently from that of *N*-body simulations. ESIM halos are spherically symmetric and non-rotating. By assumption, the collapse conserves the angular and radial momenta of all shells individually. The final equilibrium halos are supported against collapse by radial and tangential velocity dispersion.

Despite the differences between *N*-body and ESIM methods and the differing final density profiles, both types of halos are characterized by a scale-free ρ/σ^3 profile. We speculate that because this feature is common to the two types of halos, it is an outcome of the one piece of physics shared by the two methods: violent relaxation. At the very least violent relaxation is a sufficient, if not the necessary condition needed to produce $\rho/\sigma^3 \propto r^\alpha$. We will further test this hypothesis in subsequent work.

If the scale-free nature of ρ/σ^3 is, in fact, a generic feature of collisionless halos, it implies an additional constraint on the halo structure as the density and velocity dispersion profiles are now closely related. This advances us slightly further in our understanding of the collisionless collapse of dark matter halos. Our ultimate goal is to identify the physical processes that shape the dark matter halos produced in simulations, and eventually, in the real Universe.

Chapter 4

Investigating Semi-Analytical Halo Collapse Further

Abstract

In this chapter, the Extended Semi-Analytic Method of halo collapse is discussed further. Specifically, we look at the effects of the inert ESIM core, the number of shells used, the initial power spectrum, the Hubble Constant, non-isotropic initial velocity perturbations, satellite accretion, dynamically excited halo sections, and momentum transfer.

We find that the code is robust to the inert core but not to the number of non-collapsing, external shells. To resolve this, we implement a constant fraction of non-collapsing shells for all ESIM simulations.

ESIM halos remember their initial conditions to some extent, but there is evidence that a halo wants to recover from the imposed alterations. This is possible with the density or velocity profile appearing unaltered at the cost of driving the other profiles further from the original state. Also, if the accretion rate is altered, the halo profiles will appear unaltered if there is enough subsequent quiescent accretion. It is also shown that the profile deviations need not occur at the same radius for different quantities.

Each of these simulations are in HSE but do not necessarily have a scale-free ρ/σ^3 profile. The $\rho/\sigma^3 \sim r^\alpha$ is a more restrictive condition than HSE, with its specific slope depending on the initial conditions.

Finally, I altered the physics of dark matter so that overlapping shells were able to share momentum. This is analogous to collisional dark matter which does not aid in establishing a scale-free ρ/σ^3. This supports the hypothesis that $\rho/\sigma^3 \propto r^\alpha$ is an outcome of collisionless relaxation.

4.1 Introduction

In the previous chapter, the discussion was on the method of creating ESIM (extended semi-analytical method) halos, as well as the dependence of the final properties on the initial velocity perturbations and mass scales. However, in this chapter, several other aspects of ESIM halo collapse are investigated. The goal of this section is to quantify which of these are important in driving the collapse into a specific equilibrium.

In the first few sections, the robustness of our code is tested. In Section 4.2, the mass of ESIM's inert core is varied. Section 4.3 illustrates the dependence of the final profiles on the spatial extent of the simulation.

After this, I explore the effects of global cosmology and changing the physics considered in the collapse. Section 4.4 demonstrates the effect of a scale-dependent power spectrum. The value of the Hubble Constant is altered in Section 4.5. Next, it is considered that dark matter may not be completely collisionless in Section 4.6. Section 4.7 considers halos that 'form' with no radial perturbations.

Finally, the individual halos are altered to emulate local effects. Section 4.9 simulates the accretion of satellites and under dense regions. Next, specific regions of a halo are artificially excited to see if the collapse processes can relax the halo back to the original equilibrium in Section 4.8. Finally, in section 4.10, the effect of varied accretion rates is explored.

4.2 Code Robustness Tests: Initial Seed Mass

ESIM has an inert mass at the very center of the halo; it does not evolve at all. The purpose of this is to provide a seed to start the shells' collapse. Its gravity pulls the first shells inward; this deepens the potential well, which then attracts more distant shells.

The effect of the initial seed on the final profile was unknown. This was also indicated

in Section 3.2.5, where it was shown that the inner region of the halo is not in HSE. As such, I varied the mass of the inert seed to quantify the final halo's sensitivity.

In Figure 4.1, I show 3 simulations (0018/7117, 0018/7495, and 0018/7695). These were identical in all initial conditions and parameters except the seed mass. 0018/7495 reduced the core mass by 10 times; this was done by reducing the core's radius by a factor of $10^{-1/3}$. 0018/7695's inert core was increased in mass by 10 times.

Figure 4.1 shows that the final density profile is fairly blind to the original seed mass: simulations 0018/7495 and 0018/7695 have a similar normalization to 0018/7117. The profiles do deviate around $\log r/r_{200} = -2$. The least massive core has the most different shape and inner density slope.

The velocity profiles are also similar in shape and normalization. The most massive core did have an inner velocity dispersion that breaks at $\log r/r_{200} = -2$, and the least massive core breaks interior of the standard core. Despite these changes, all halos have ρ/σ^3 profiles with a similar slope in the fitting range used in Chapter 3: $\log r/r_{200} = -2$ to 0.

All of these simulations show the same velocity anisotropy except in the very inner halo: the halos are isotropic, with perhaps a slightly radial region at $\log r/r_{200} = -3$ to -2. In the simulation with the most massive core, the inner velocity anisotropy is tangential. Also, as seen in Figure 4.2, all simulations are in HSE.

Therefore, the least massive core has slightly changed the density profile and the larger core altered the inner velocity dispersion and anisotropy. The ρ/σ^3 profiles are quite different. The overall shapes are similar but the slopes are quite different. There is a break near the core, with the smallest core breaking farther in. The best power-law fit is the lowest core mass. The slopes and RMS for the fits are [-2.4, 0.09], [-2.1, 0.06], and [-2.3, 0.08] for 0018/7117, 0018/7495, and 0018/7695.

The standard core size will still be our default, however. All halos are in HSE; changing the core size just to improve the power-law fit is superficial.

4.3 Code Robustness Tests: Extended Potential

I also studied the effect of the simulation's spatial extent. The ESIM simulation technique produces the proto-halo and divides it up into spherical shells. There are many

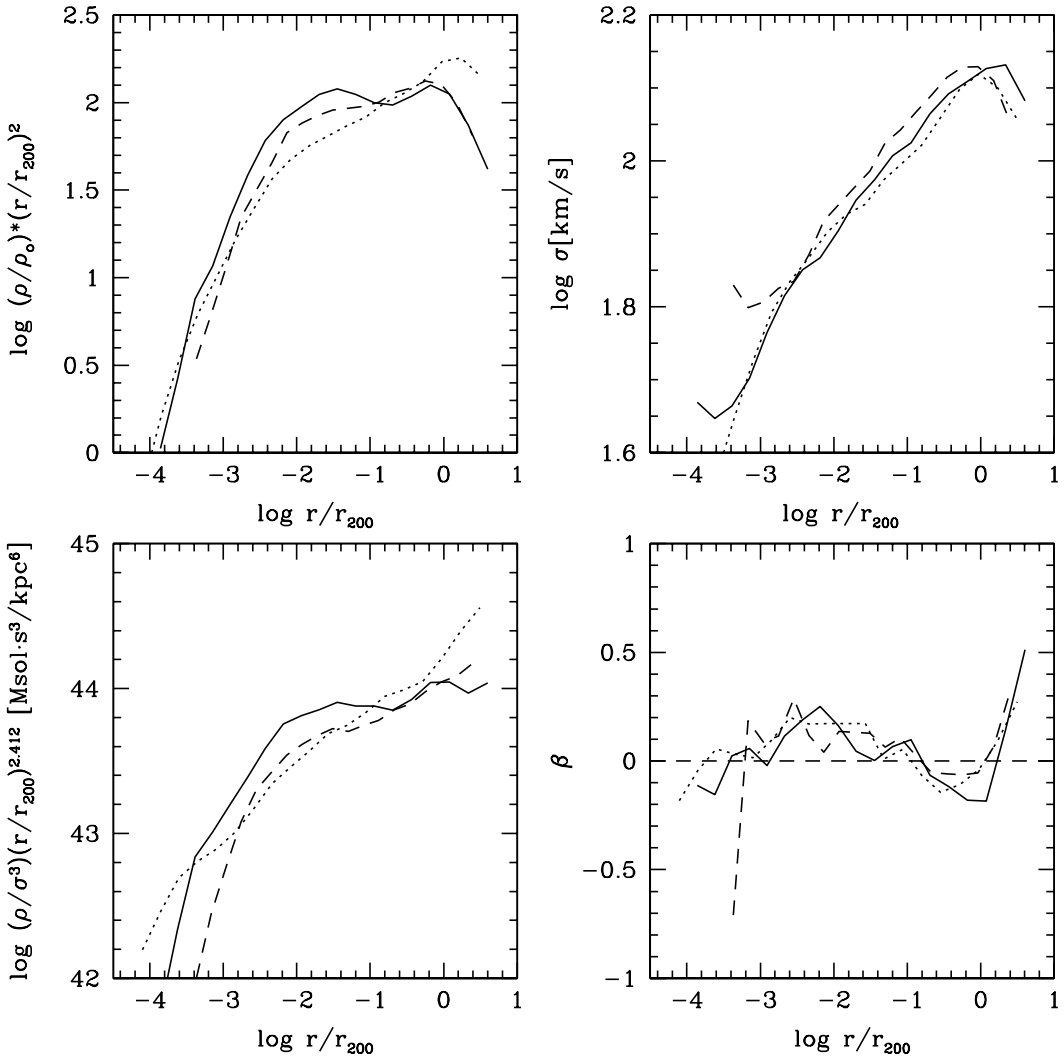

Figure 4.1: This figure shows the effect of varied initial seed masses. Simulation 0018/7117 (solid line) is the standard initial seed, 0018/7495 (dotted line) has a core 10 times smaller, and 0018/7695 (dashed line) has a core 10 times larger. The points were binned into groups of 100.

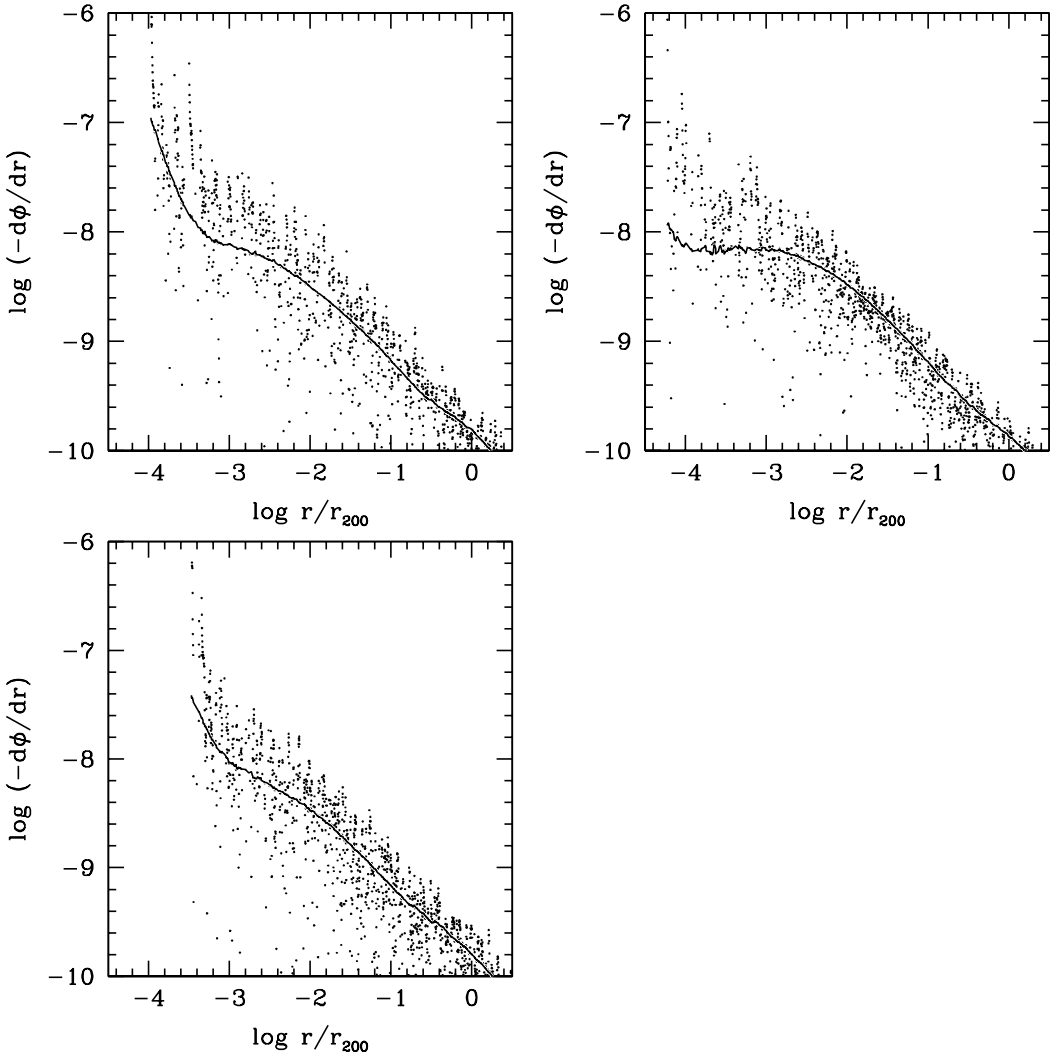

Figure 4.2: The hydrostatic equilibrium (HSE) condition: the LHS and RHS of equation 3.2 are shown as points and the smooth curve, respectively. Where the line traces the plotted points, the halo is in hydrostatic equilibrium. This figure shows the effect of varied initial seed masses. Simulation 0018/7117 (top-left) is the standard initial seed, 0018/7495 (top-right) has a core 10 times smaller, and 0018/7695 (bottom-left) has a core 10 times larger.

more shells than will actually collapse – as such, a point is defined where the simulation is truncated. The only effect of these shells is to deepen the potential inside of them. As the general potential is given by:

$$\Phi(r) = \frac{-4\pi G}{r}\int_0^r \rho(r')r'^2 dr' - 4\pi G\int_r^\infty \rho(r')r'dr'. \tag{4.1}$$

The potential inside a uniform shell of mass is:

$$\Phi_{inside\,shell} = \frac{-GM}{R}. \tag{4.2}$$

As is seen from Equation 4.2, the potential does not vary with the radius of the internal mass; therefore, there is no internal potential gradient from this shell. The gravitational force used to collapse the shells is only dependent on the potential's gradient; altering the normalization (i.e. depth) of the potential well should have no effect.

$$F = \nabla\Phi = 0 \tag{4.3}$$

In Figure 4.3, I show the effect of changing the spatial extent of these external, ever-expanding shells. Our standard simulation, 0018/7117, was defined by 669 shells: the inner most 520 collapsed, up to shell 564 turned around from the Hubble flow by $z = 0$, and shells out to 669 were used to calculate the potential. In simulation 0018/7184, 762 shells were used to calculate the potential, thus expanding the spatial extent of our simulation.

As is seen the figure, there are significant differences in the profiles. We believe that this is due to the time dependence of the potential. As the extra, outer shells expand, the inner potential drops via Equation 4.2. The depth of the potential well caused by these shells does not matter, but the time variations caused by these shells do.

Because of this, I have chosen to always use a constant proportion of external shells to that which reach turn-around at $z = 0$. An extra 18.96% of shells are considered (of the number of the shells that will turn-around); these will not turn-around by the present. Thus, all of our final halos are comparable.

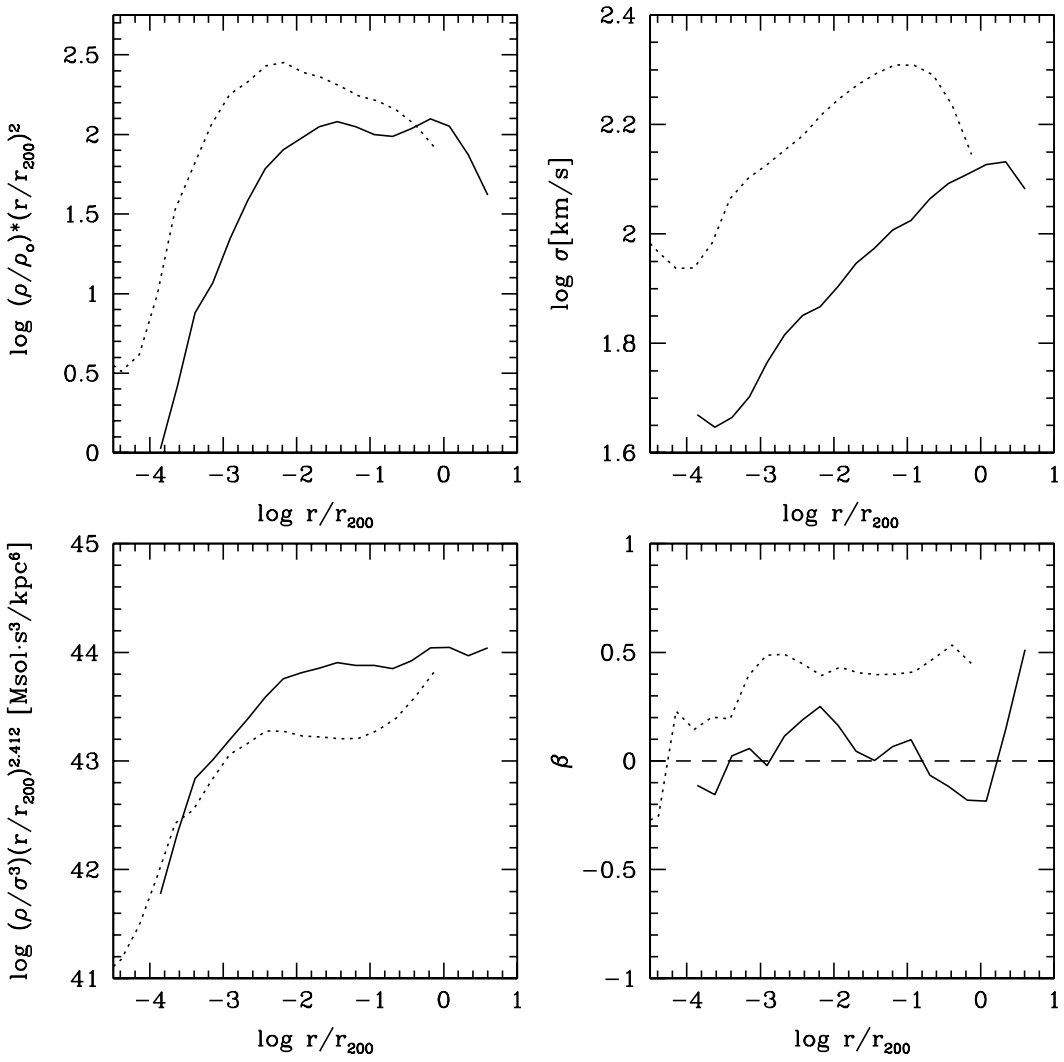

Figure 4.3: This figure shows the effect due to including more shells in our simulation. The standard simulation 0018/7117 (solid line) used 669 shells. Simulation 0018/7184 (dotted line) used 762 shells. The points were binned into groups of 100.

4.4 Cosmological Effects: Initial Power Spectra

One of the first inputs into creating an ESIM halo is the primordial power-spectra. This is dependent on the cosmology and affects the relative amount of structure at each physical scale.

$$P(k) \propto k^n \tag{4.4}$$

The typical choice for n is the scale-invariant, Harrison-Zeldovich form: $n = 1$. The variable k is the wave number and is inversely proportional to physical scale.

In all the simulations (sans the ones presented in this section) our power spectra are Harrison-Zeldovich. Here, I calculate the dependence of the final profiles on two additional power spectra: simulation 0041/1002 had $n = 1.5$ and 0042/1002 had $n = 0.5$.

Simulation 0041/1002, with $n = 1.5$, has suppressed power at small k (large physical scales), and increased power at large k (small physical scales). Simulation 0042/1002 is the reverse of this scenario. The other parameters were the same as our standard halo: simulation 0018/7117.

As can be seen in Figure 4.4, the density profile for 0041/1002 is nearly identical to the Harrison-Zeldovich power spectrum, with a deviation at $\log r/r_{200} = -2$. Adding additional power on large scales seems to have allowed a denser halo in 0042/1002. The velocity dispersion of 0042/1002 has also increased to balance this extra mass.

Despite the change of the velocity dispersion profiles, the velocity anisotropy profiles, β, of 0041/1002 and 0018/7117 are fairly consistent within the noise. Simulation 0042/1002 has a region that is more tangential at $\log r/r_{200} = -2.5$ to -0.5.

The coarse-grained phase-space density profiles have the following slope and RMS values: [-2.4, 0.09], [-2.2, 0.09], and [-2.3, 0.12]. The slopes for 0018/7117 and 0041/1002 are similar; this is not surprising, as their density and velocity profiles are similar. The similar RMS values indicate that even when the density profiles are altered, the velocity dispersion is altered in such a way to support the halo and keep the ρ/σ^3 profile a power-law.

Changing the initial power-spectra does have an effect on the mass distribution, velocity dispersion, and the ρ/σ^3 normalization. Therefore, collisionless relaxation does not wipe out all memory of the initial conditions.

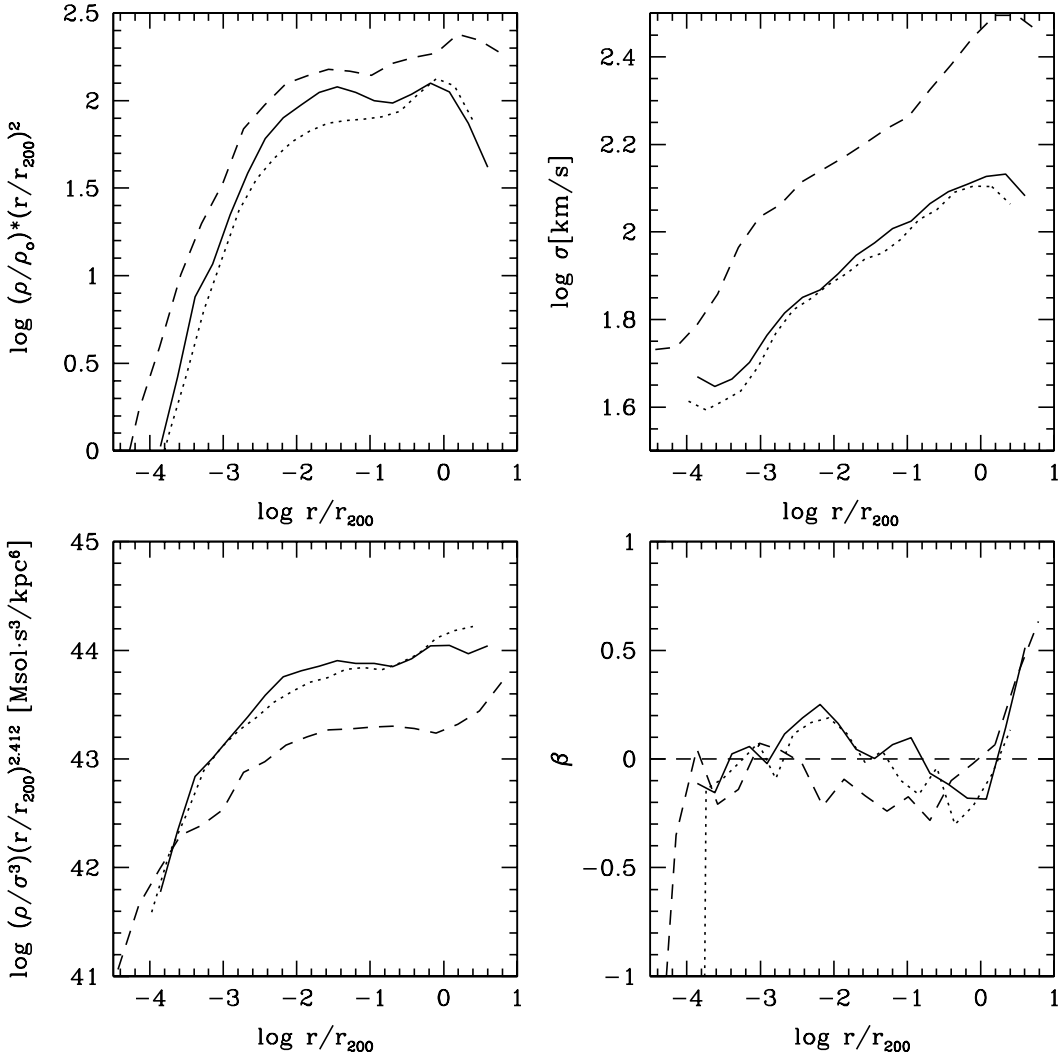

Figure 4.4: This figure shows the effect of tilted power spectra. Simulation 0018/7117 (solid line) is the standard power spectra, 0041/1002 (dotted line, $n = 1.5$) has more power on small scales, and 0042/1002 (dashed line, $n = 0.5$) has less power on small scales. The points were binned into groups of 100.

4.5 Cosmological Effects: Hubble constant

As will be seen in Chapter 5, our halo's profiles appear to be determined by accretion rate. An important factor in determining the accretion rate is the strength of the Hubble Flow. The stronger the flow, the more strongly the mass will be pulled away from the central overdensity, and it will take longer before collapsing. This would lower the accretion rate.

Additionally, changing the value of the Hubble Constant changes the normalization of the power spectrum, gives more power on large scales for smaller h, and alters the BBKS transfer function. Once the halo is collapsed, the Hubble constant is used to define the critical density and the virial radius at $200 \cdot \rho_{crit}$.

The strength of the current Hubble flow is described by the Hubble constant: $v_{expansion} = H \cdot r$. Though, as the Hubble Constant is not exactly determined, it is often parameterized by h:

$$H_o = h \cdot 100\,(km/s)/Mpc \tag{4.5}$$

Throughout this dissertation, $h = 0.5$ has been our default. Once I move onto Section 4.10, it will be altered to $h = 1.0$ so that the results can be compared with the N-body simulations. The default halo will also be changed from galactic-sized halos to group-sized halos.

The results of a stronger Hubble Flow are shown in Figure 4.5. The standard simulation and 0040/1002, which has $h = 1.0$, are shown.

The density profile is slightly more centrally concentrated, with a slightly different shape. The effects of an increased Hubble constant are obvious in the velocity dispersion; the larger Hubble flow increased the values by a factor of $\approx 10^{0.3}$. The velocity anisotropy again appears to be quite similar for both simulations.

The ρ/σ^3 profiles have different slopes and shapes, with the altered simulation no longer well described by a power-law fit. The standard simulation has slope and RMS values of [-2.4, 0.09]; the altered simulation has [-2.0, 0.08]. Altering the cosmology via the Hubble parameter results in significant changes to the velocity dispersion profiles.

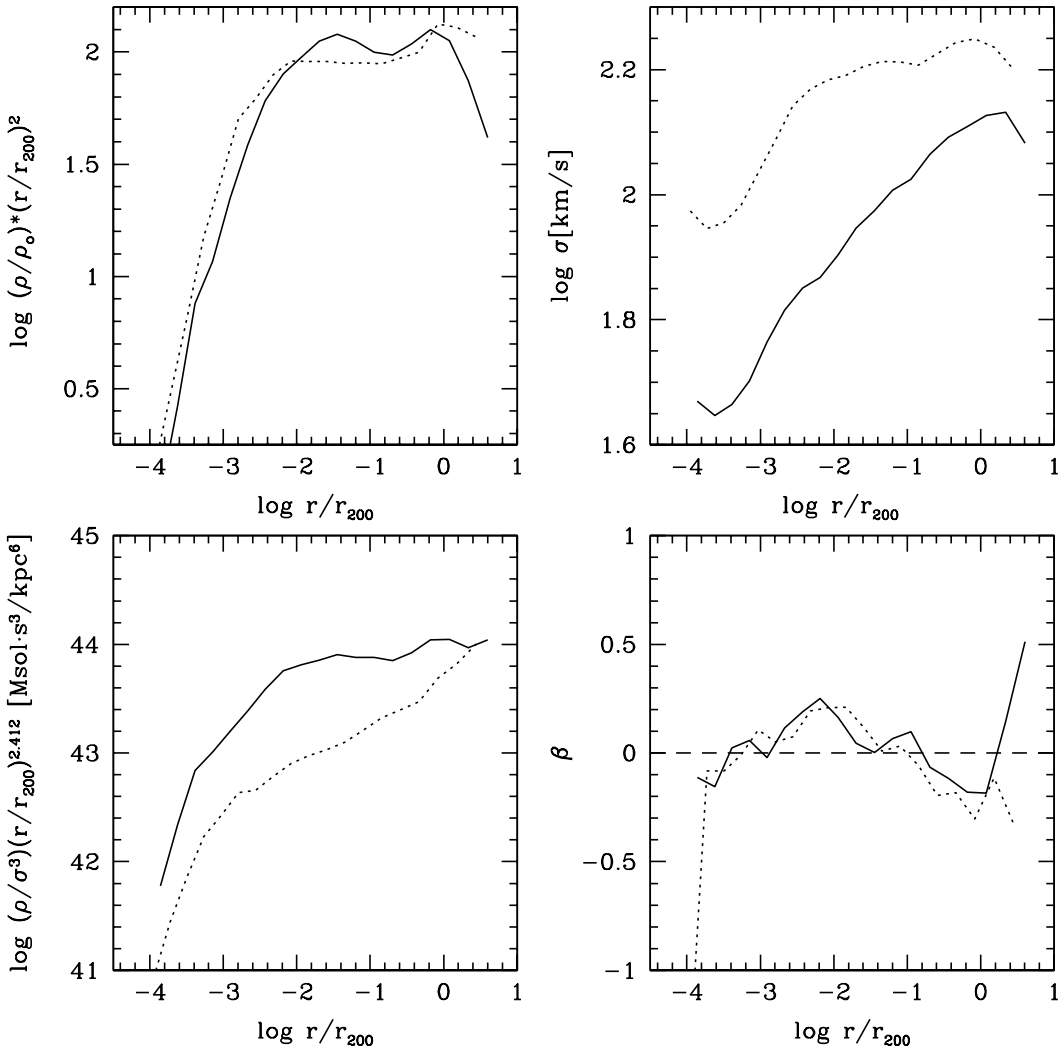

Figure 4.5: This figure shows the effect of a larger Hubble constant. Simulation 0018/7117 (solid line) is the standard h=0.5 used up to this point in the dissertation. Simulation 0040/1002 (dotted line) has $h = 1.0$. The points were binned into groups of 100.

4.6 Physical Effects: Momentum sharing shells

As has been discussed in Chapters 1 and 3, the semi-analytic collapse of ESIM halos is very limited in comparison with the more realistic *N*-body simulations. *N*-body particles are able to move independently and transfer energy via the global potential, local substructure, and effects such as the Radial Orbit Instability. This is not possible in ESIM halos: all mass is strictly collisionless, and energy is only altered due to global potential changes.

In this section I explore the effects of energy transfer between shells. This was primarily done to see if having more degrees of freedom would improve the ρ/σ^3 power-law feature.

The momentum transfer is taken into account in the following way. At each time step, I look for shells that overlap. For each pair of overlapping shells, the fraction of overlapping mass is calculated: δ_a and δ_b. Let shell a be the shell with the least mass and η be the efficiency of transfer. The amount of angular momentum to be transferred is given by:

$$J = \eta \cdot \delta_a \cdot M_a \cdot \frac{J_a - J_b}{M_a + M_b} \tag{4.6}$$

This scheme was chosen so that momentum is always moved from the shell with higher momentum per unit mass to the other. Thus, the halo should approach an equipartition where all shells have equal momentum per unit mass. In Figure 4.6, our momentum-transferring halo profiles can be seen. Simulation 0018/2989, with $\eta = 0.1$, does not produce a realistic halo. The density profile has several slope discontinuities, with corresponding irregularities in the other profiles. As such, this is an unphysical simulation.

Simulation 0018/9005 was created to make the routine more physical. Momentum was only allowed to be transferred if it approached the original (pre-secondary velocity) momentum profile. This simulation also had $\eta = 0.1$. Simulation 0018/9005 is much better well-behaved though the density profile is depressed, and the velocity dispersion and anisotropy profiles are significantly reduced. Despite this, the ρ/σ^3 profile is a slightly better power-law. The slope and RMS are [-2.1, 0.078] for 0018/9005 and [-2.41, 0.09] for the standard case.

The original, collisionless dark matter scenario provides the simplest solution with

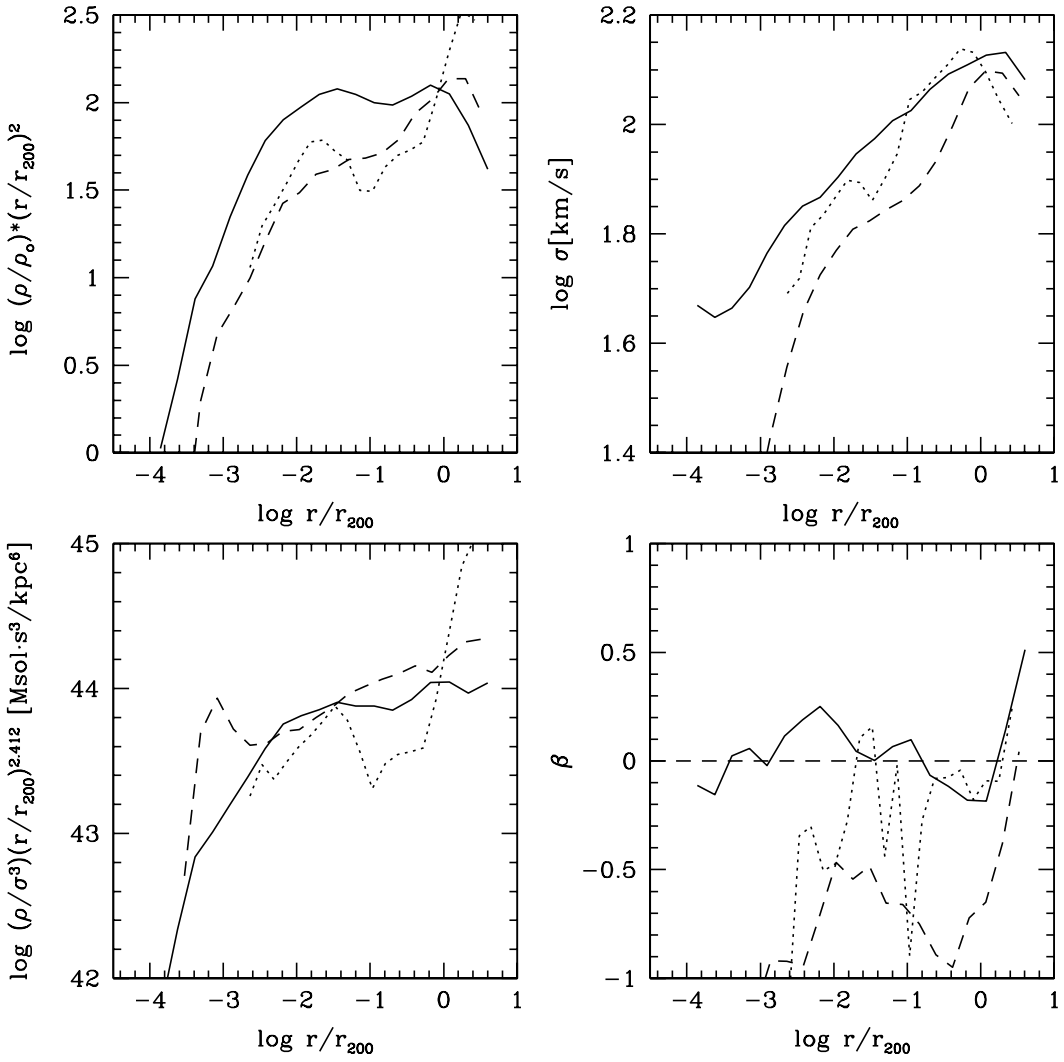

Figure 4.6: This figure shows the effect on a standard halo of allowing overlapping shells to transfer angular momentum. Simulation 0018/7117 is the standard halo (solid line). Simulation 0018/2989 (dotted line) is the same simulation, but with the overlapping shells able to move momentum at an efficiency of 0.1. Simulation 0018/9005 (dashed line) has the same efficiency, but is only allowed to transfer momentum if it approached the original (pre-secondary velocity) momentum profile.

a monotonic density profile. Altering the physics in ESIM to allow for momentum transfer only improved the ρ/σ^3 power-law when such transfer had to approach the initial angular momentum profile. However, this was done for a smoothly accreting, standard halo. Could momentum sharing improve the ρ/σ^3 profile for an already broken power-law?

To this end, the angular momentum sharing was applied to the 'broken power-law' halo presented in Section 3.14. This halo has a discontinuous jump in the scaling parameter: shells with the initial comoving radii between 0.59 and 0.79 Mpc were assigned a scaling parameter of 5.0, while the rest of the halo was assigned a scaling parameter of 0.9.

Figure 4.7 shows simulation 0018/7992: this is the perturbed halo with no momentum sharing allowed. 0018/9004, however, was allowed to share momentum with an efficiency $\eta = 0.1$, but only if it approached the original momentum profile. As can be seen, the momentum transfer did not help the density or velocity dispersion profiles return to their pre-perturbed state.

Our conclusion from this section is that momentum sharing between overlapping shells does not help the halo to collapse towards a preferred, physical, or stable state. It is unphysical and unpredictable. I now return to our regularly scheduled programming: exploring the physical effects due to local changes in the halo's environment.

4.7 Physical Effects: Limited Initial Velocities

In this Section, the dynamical effects of the collapse is isolated. This is done by limiting the initial radial velocity perturbations. If the halo can recover from this, during the collapse process, similar final profiles can be seen.

In figure 4.8 I present simulation 0018/7089. This simulation is the standard halo, but it has zero radial secondary velocity perturbations; the magnitude of the perturbations was unchanged. I find that simulation 0018/7089 is able to recover the standard density profile within 0.1 dex. Thus the density profile is not very dependent on the initial velocity anisotropy of the secondary velocities. As shown in Section 3.2.3, however, it is dependent on the magnitude of those velocities.

The halo is kinematically very different: it has much lower velocity dispersions, a

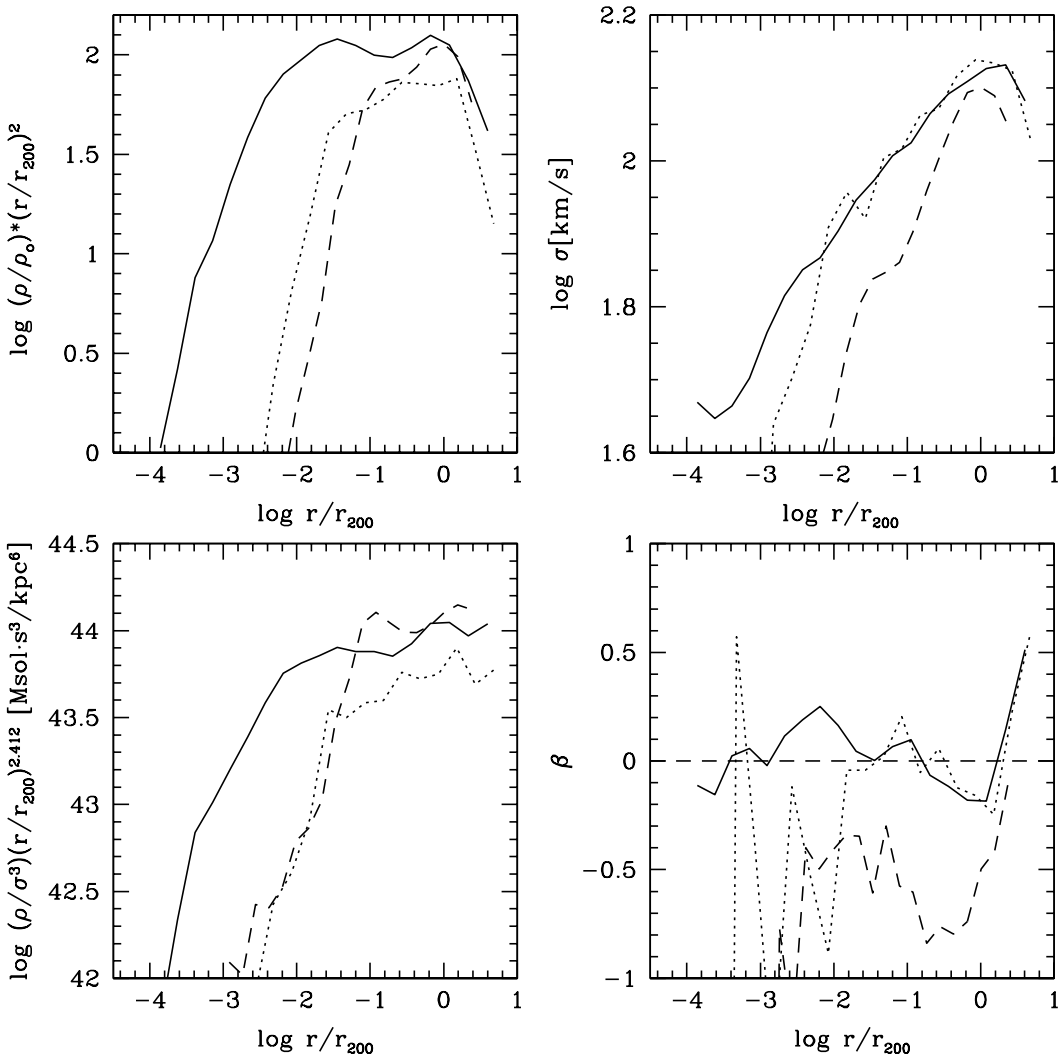

Figure 4.7: This figure shows simulations 0018/7992 (dotted line) and 0018/9004 (dashed line). Simulation 0018/7992 has a broken ρ/σ^3 due to an inner scaling parameter 5 times normal; 0018/9004 is the same simulation but with the ability to share angular momentum between overlapping shells. All profiles are binned into groups of 100 points. The fiducial 0018/7117 (solid line) simulation is also shown here for comparison.

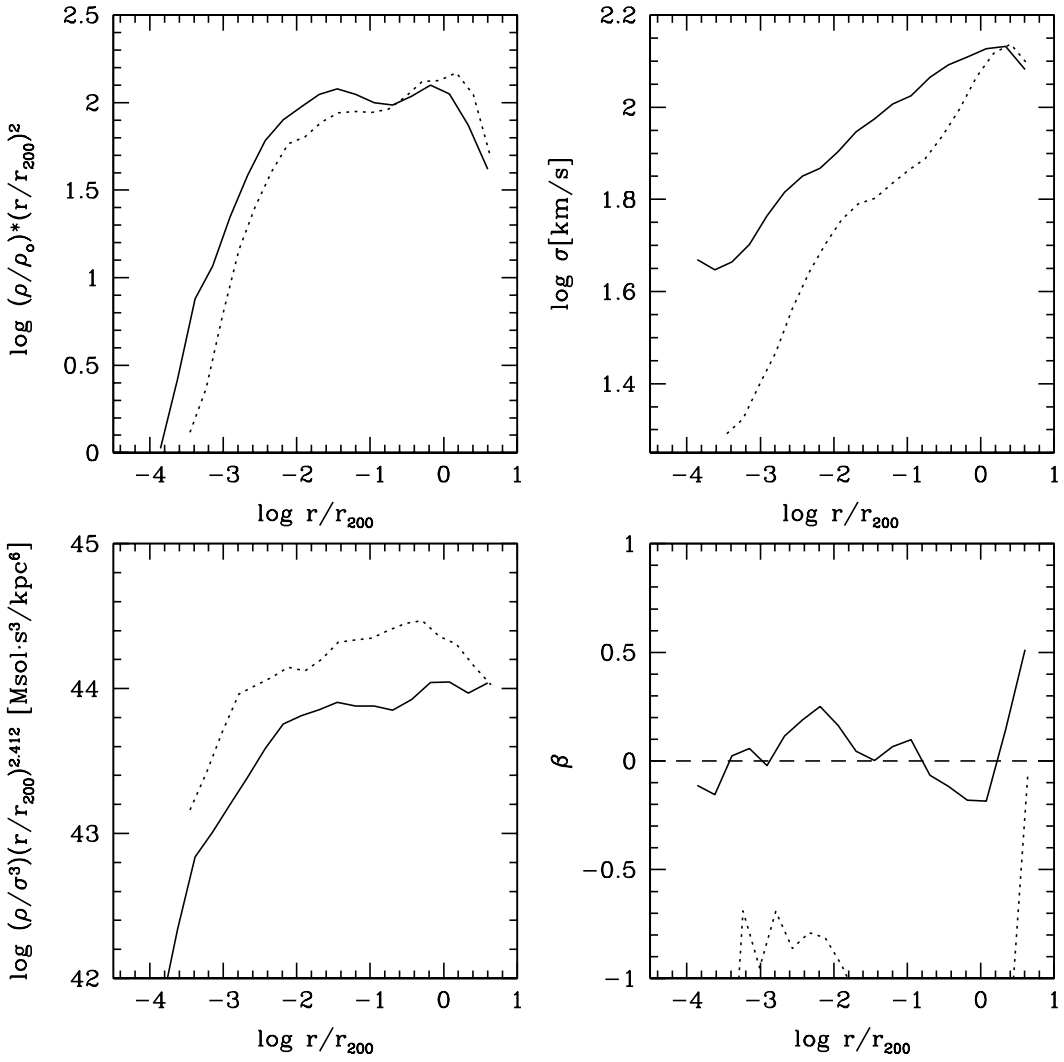

Figure 4.8: This figure shows the simulations with no radial secondary velocity perturbations, as compared with our standard halo (0018/7117, solid line). Simulation 0018/7089 has no initial radial perturbations (dotted line). The points have been binned into groups of 100.

shallow and bumpy ρ/σ^3 profile, and a tangential β profile. Despite this, the halo is in hydrostatic equilibrium (Figure 4.9).

From this section, I conclude that the dynamics of ESIM halo collapse is able to preserve the final density profile, despite having very different initial velocity anisotropies. All kinematic measures (velocity dispersion, velocity anisotropy, and phase-space density), however, are significantly altered in order to support this density profile.

4.8 Local Effects: Excited Bubbles

Up to this point, I have explored the effect of the initial conditions or cosmology on the final halos. However, our attention is now turned to studying the effect of local mass and velocity discontinuities. These are meant to simulate gaps in mass accretion, accreting satellites, and extra momentum or energy from mergers.

In this section, the physical properties of a short radial portion of the halo are changed, and the effects on the final equilibrium state are observed. This is important, as I do not yet understand how the final equilibrium is chosen by the initial conditions.

The previous section probed one part of this question; it determined that the collapse processes were able to convert purely initial tangential motions into a stable final state. But in this section, I only alter the kinematic properties of a section of the halo, after it has already collapsed. Thus I will be able to see if the virialized portions of the halo are able to recover.

In simulation 0018/2234, I altered the energy and velocity of shells that overlapped a specific radius ($R = 0.25 \cdot R_{shell\,400}$) at time step 400. For each of these shells, their energy and secondary velocities were replaced by that of shell 400. The radial range of all of these shells was (before readjusting) $5.28 \cdot 10^{20}$ to $1.40 \cdot 10^{23}$ cm. The result of this is a net energy increase of 2.07% and an increase in secondary velocities of 98.9%.

Simulation 0018/2235 is presented in Figure 4.10; the energy and secondary velocities of half of the overlapping shells at $R = 0.25 \cdot R_{400}$ were altered at time step 400. The energies and secondary velocities of these shells were multiplied by constant values derived from the respective differences between shells 319 and 400. The result of this is a net energy decrease of 1% and velocity gain of 3.89 times.

The hypothesis is that these altered shells would 'rise' in the pressure-supported

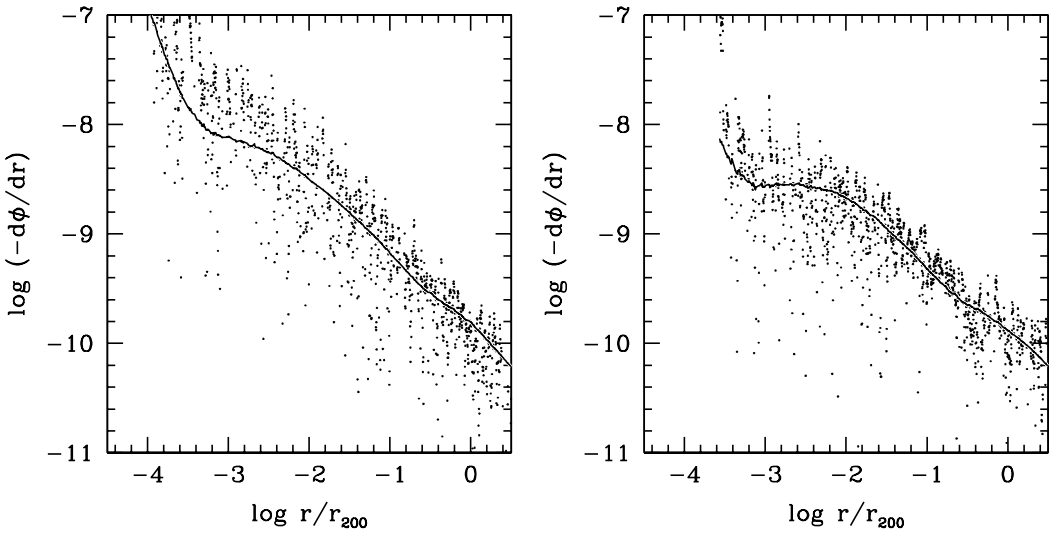

Figure 4.9: This figure shows the hydrostatic status of 0018/7089 as compared with our standard halo (0018/7117, solid line). Simulation 0018/7089 has no initial radial perturbations (dotted line). The points have been binned into groups of 100.

halo. I was also interested in seeing if the profiles would fix themselves (i.e. return to the standard simulation's final profiles). The final result did not show this; the entire radial range of the 'bubble' simulations is significantly different from the fiducial 0018/7117.

In Figure 4.10, the final density profiles vary by up to 0.4 dex, with the discrepancy increasing with radius. The density profile are altered much more than the velocity dispersion profiles. Simulation 0018/2234 has a mass excess at the virial radius (this may be where the excited mass has settled) and 0018/2235, surprisingly, has no mass excess – just a decrement at $\log r/r_{200} = -3to - 0.75$ These differences lead to a significantly different ρ/σ^3 profile beyond $\log r/r_{200} = -1$, even for 0018/2235 – whose mass profile deviated far interior to that. The ρ/σ^3 power-law fits' slopes and RMS are [-2.4, 0.09], [-2.4, 0.17], and [-2.3, 0.09].

The velocity anisotropy profile also shows deviations. For 0018/2234, is more radial beyond $\log r/r_{200} = -1.5$; this is interior to its density excess. 0018/2235, however, is more tangential at $\log r/r_{200}$=-1 which is exterior to its main density deviation. Here, the velocity dispersion normalization and the velocity anisotropy shapes were altered. These two effects seem to have balanced the ρ/σ^3 profile towards a power-law out to $\log r/r_{200}$=-1, where this breaks down for unknown reasons. These halos are are in HSE (Figure 4.11); they have managed to find equilibrium despite the altered shell properties (post-collapse). Thus, it seems that these halos have recovered to a point.

4.9 Local Effects: Shell-like Satellites

One of the most limiting aspects of ESIM is that it is purely spherical. Therefore, it does not have the ability to have substructure or realistic satellite accretion. One can test, however, the effect of non-astrophysical substructure, where a specific shell, or set of shells are make overdense compared to nearby shells.

This is done by altering the mass profile of the shells. The mass of several shells can be reduced (increased), which would reduce (increase) the accretion rate and simulate a gap in accretion (merger). These are not physical mergers, as an actual merger would happen along a conic-section orbit; thus, there is an asymmetry in which angular momentum is acquired and tidal forces applied.

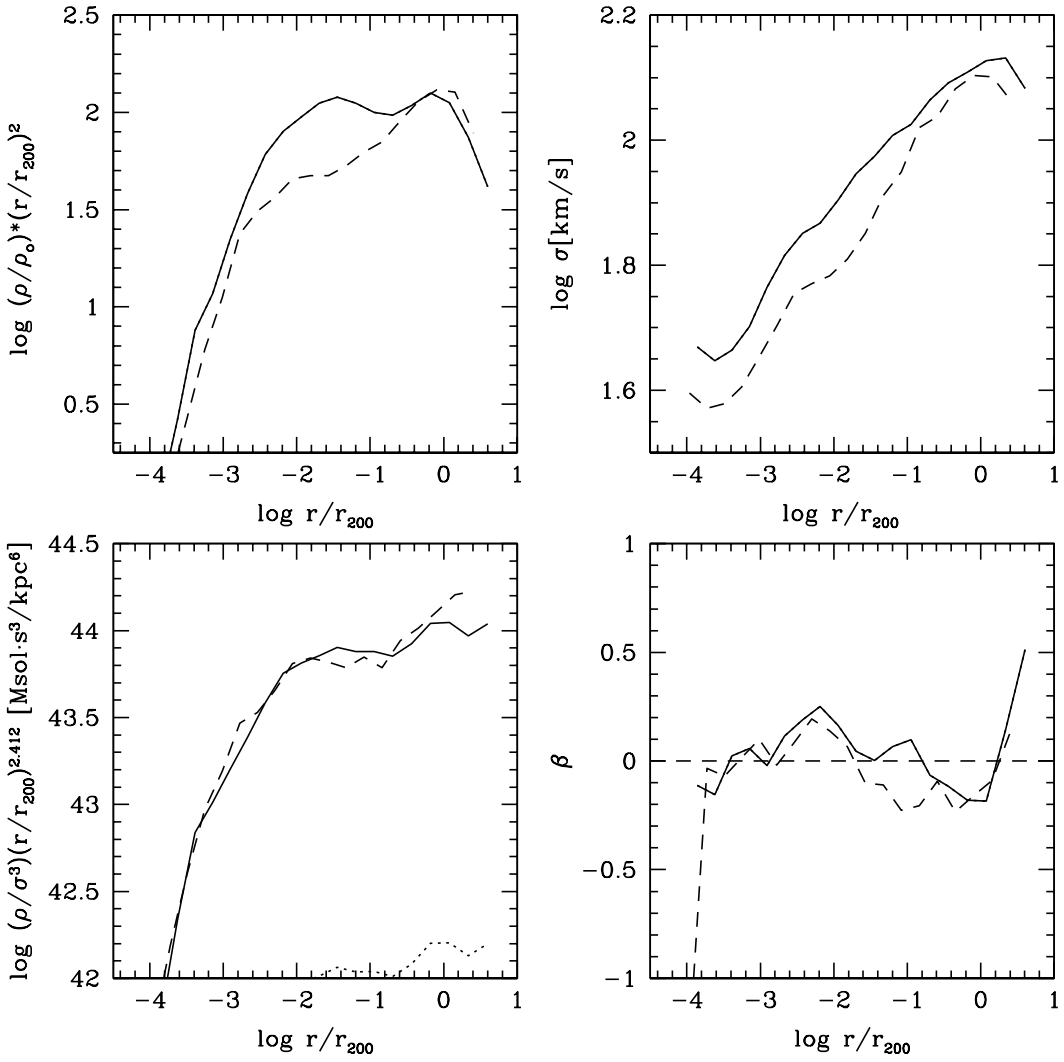

Figure 4.10: In this figure I show 3 simulations: the standard 0018/7117 (solid line), the first 'bubble' simulation (0018/2234, dotted line), and the second 'bubble' simulation (0018/2235, dashed line). The points were binned into groups of 100.

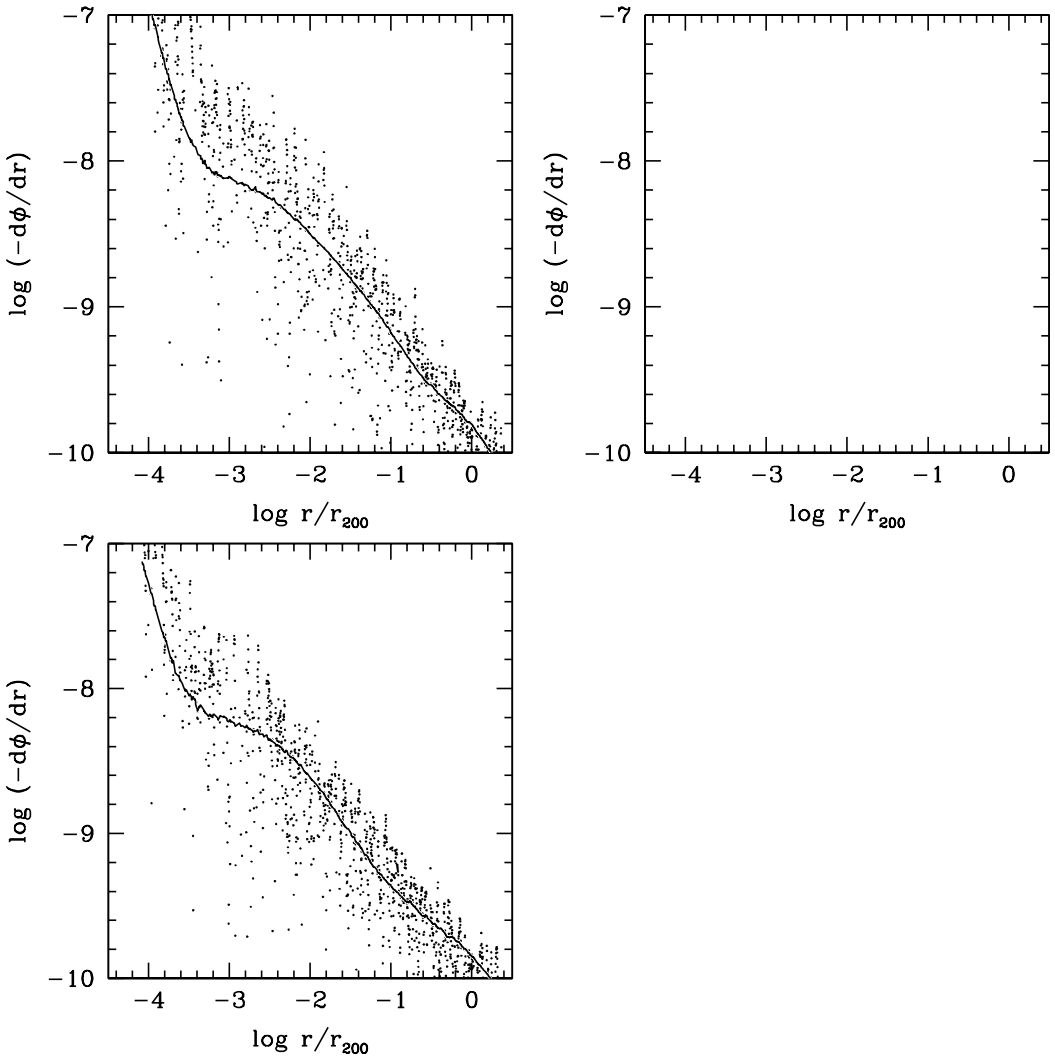

Figure 4.11: The hydrostatic equilibrium (HSE) condition: the LHS and RHS of equation 3.2 are shown as points and the smooth curve, respectively. Where the line traces the plotted points, the halo is in hydrostatic equilibrium. In this figure 3 simulations are shown: the standard 0018/7117 (top-left), the first 'bubble' simulation (0018/2234, top-right), the final 'bubble' simulation (0018/2235, bottom-left).

In this section, I will simulate these non-astrophysical situations and use them to judge how the equilibrium of the halo is altered due to the accretion/merger. Here 3 simulations are presented: the standard (0018/8001), the accretion of a gap (0018/8002), and a merger event (0018/8003). Unlike the other simulations presented to this point in the dissertation, these are not shown as an average of 10 simulations; each line is only 1 simulation.

To simulate the gap region, I deleted shells 280-300 and 310-320. This corresponds to a gap between the initial comoving radii of $1.77 \cdot 10^{-1}$ to $2.16 \cdot 10^{-1}$ Mpc and $2.38 \cdot 10^{-1}$ to $2.63 \cdot 10^{-1}$ Mpc. The mass removed was $2.57 \cdot 10^{9}$ $M_{\odot}$ and $2.60 \cdot 10^{9}$ $M_{\odot}$, respectively.

The merger was created by redistributing the mass from shells 280-300 and 310-320 into the intermediate shells in the following way: shells 301 to 309 received 5%, 7%, 10%, 15%, 26%, 15%, 10%, 7%, and 5%. This arrangement is used to emulate reality: real sub-structure accretes nearby mass, thereby clearing the inter-galactic space. Thus, there would be a lower-density region between the two objects (represented by shells 280-300) and another behind the sub-structure (represented by shells 310-320).

As seen in Figure 4.12, the deviations in the density profile were localized: $\log r/r_{200} = -3$ to -1. The gap simulation is under-dense in this region; the accretion event, surprisingly, is also slightly under-dense. The velocity dispersion's deviations are more visible further into the halo: $\log r/r_{200} = -3.5$ to -0.5. Again, the original simulation has larger velocity dispersions than the altered halos. The velocity anisotropy profiles, β, also have distinct differences in this range (-2.2 to -1.2): the low-density region and merger simulations are tangential rather than isotropic.

Surprisingly, with the deviations in the density and velocity dispersion values, the ρ/σ^3 profiles look very similar. They do vary in the region of -3.5 to -0.5, leading to slope and RMS values of [-2.14, 0.141], [-2.16, 0.167], and [-2.15, 0.180] for 0018/8001, 0018/8002, and 0018/8003. These are all similar, despite the dramatic difference in the mass distribution. Also, the normalizations are identical for all the simulations, which has not been the case for the previous sections. The velocity dispersion has altered itself to support the density and keep the ρ/σ^3 relatively constant.

As is shown in figure 4.13, all of these halos are in HSE. They have evolved and relaxed into a configuration that is stable. The surprising result is that the dispersion profile's deviations (and ρ/σ^3) is located inwards of the main density and β deviations:

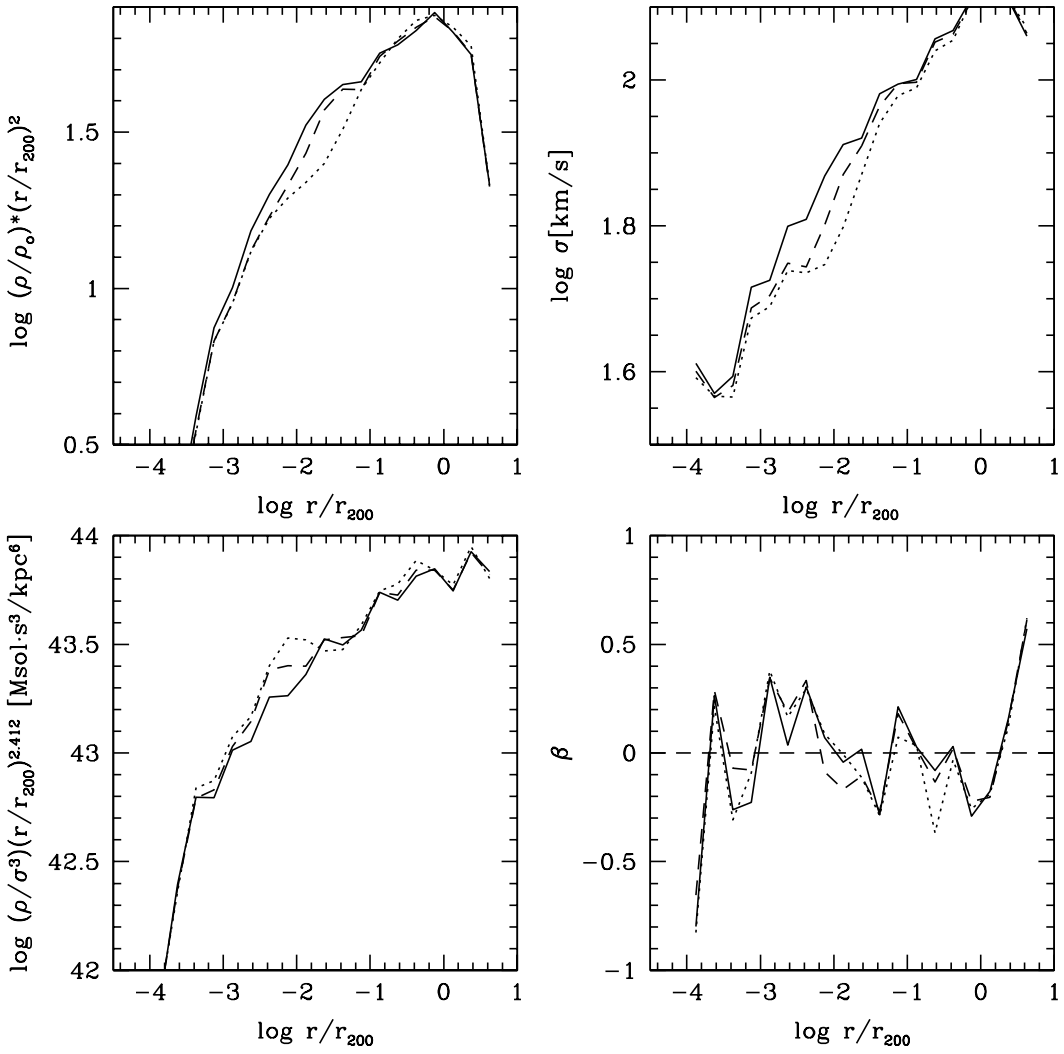

Figure 4.12: In this figure 3 simulations can be seen: the standard 0018/8001 (solid line), a gap (i.e. zero density region) (0018/8002, dotted line), and a merger event (0018/8003, dashed line). The points were binned into groups of 100.

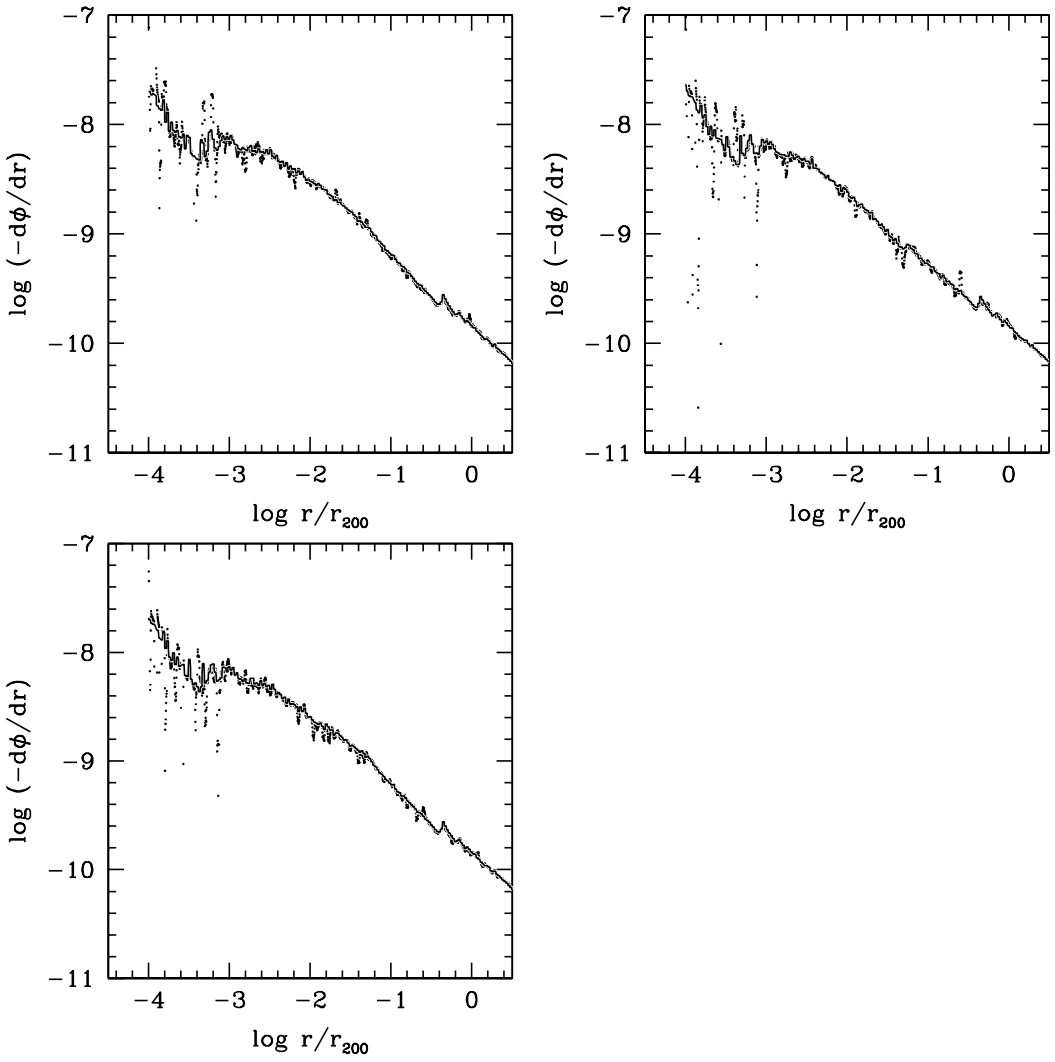

Figure 4.13: The hydrostatic equilibrium (HSE) condition: the LHS and RHS of equation 3.2 are shown as points and the smooth curve, respectively. Where the line traces the plotted points, the halo is in hydrostatic equilibrium. In this figure 3 simulations are shown: the standard 0018/8001 (top-left), the accretion of a low-density region (0018/8002, top-right), and a merger event (0018/8003, bottom-left).

$\log r/r_{200}$ = -1.5.

Also interesting is that all of the profiles are identical for regions that collapsed very early or late. At these times, the accretion rates were identical. This implies that the accretion rate is very important in determining the final profiles' shapes and normalizations.

4.10 Local Effects: Accretion Variations

Building on the previous section, here I explore the effect of accretion further. Four simulations have been designed specifically to examine the effects of the accretion rate on the final halo profiles. This work was done in collaboration with Dr. Eduard Salvador-Sole.

Simulation 0035/1001 is our fiducial halo for this section and the rest of the dissertation. It is a group-sized halo (using a mass power spectrum filter of r_h=0.35 Mpc, see section 3.2.2) Also, for the rest of the dissertation, the Hubble constant will have a value $h = 1$. This halo was described by 544 shells that collapse by $z = 0$ and 572 shells reaching turnaround.

The four altered simulations differ only in their initial mass profiles. They are not astrophysical; these were created to explore the processes involved in halo collapse. All of the initial density profiles are shown in Figure 4.14.

Simulation 0035/1002 has a flat mass profile (w.r.t. each shell) within shell 450 (ICR[1] $= 9.59 \cdot 10^{-1}\, Mpc$). The normalization of the mass plateau was such that the total halo mass was conserved; each shell's mass was $4.70 \cdot 10^9 M_\odot$.

Halo 0035/1003 was created by varying the density interior to shell 450. The density profile was prescribed by a sine wave; the normalization is such that the total mass is conserved. For a given shell, i, the mass prescription is:

$$m_{i,new} = \frac{1}{1.618} 10^{[\frac{1}{2} \cdot sin(i \cdot 0.05) + log(m_{i,old})]} \tag{4.7}$$

Simulation 0035/1005 also has a varied inner density, but this time has two altered regions separated by a large discontinuity. Here, the mass from shells 1-240 (ICR_{240} =

[1] ICR stands for the initial comoving radius.

$1.19 \cdot 10^{-1}\,Mpc$) was distributed into shells 1-300 ($ICR_{300} = 2.91 \cdot 10^{-1}\,Mpc$). Mass from shells 241-350 (to $ICR_{350} = 3.54 \cdot 10^{-1}\,Mpc$) was distributed into shells 301-350. The first section is under-dense, on average, and the second is over-dense. The first section has a flat mass profile (w.r.t. each shell); each shell has a mass of $1.81 \cdot 10^{7} M_{\odot}$. The second section has a flat density profile (w.r.t. radius). Once again, the total mass has been conserved.

The final profiles for these three altered halos are shown in Figures 4.14, 4.15, and 4.16. Also the HSE status of all four of these halos is shown in Figure 4.18. Similar to Section 4.9, these simulations are not averages of 10 halos. Each figure here only shows one simulation.

The hypothesis that I would like to test using these halos is the following: halos' density profiles are determined by the accretion rate. Specifically, I would like to test whether halos forget their past accretion rate; therefore, the profiles are only determined by the current accretion rate and the inner mean density. This last statement explains why all of our mass alterations have conserved mass; all halos have the same inner mean density at the end of the discontinuous regions.

Thus, these proto-halos have altered mass profiles, interior to a specific shell (shells 450, 450, and 350 respectively). These shells collapse well before the present. Therefore, the halos will have time to adjust their mass distributions by $z = 0$. If the hypothesis is correct, the $z = 0$ mass profiles should be evolving back to the fiducial profiles of 0035/1001.

A secondary goal is to look at the effect of discontinuities in the mass accretion rate. All of these altered halo profiles have discontinuities, but 0035/1005 has the strongest discontinuity. A halo without discontinuities is hypothesized by Salvadore-Sole et al. (2007) to grow from the inside out; this would be represented by our fiducial halo.

The accretion and density discontinuities in our altered halos will cause a more significant rearrangement of the energy and mass balance in the halo, as it finds its equilibrium. Therefore, these halos may not form "inside out".

The results from these simulations show that all of these halos are in HSE; 0035/1002 and 0035/1005 are in a very different equilibrium state.

These halos have not completely forgotten their initial conditions. This is obvious in 0035/1002 and 0035/1005, as the density profiles do not agree with the fiducial profile.

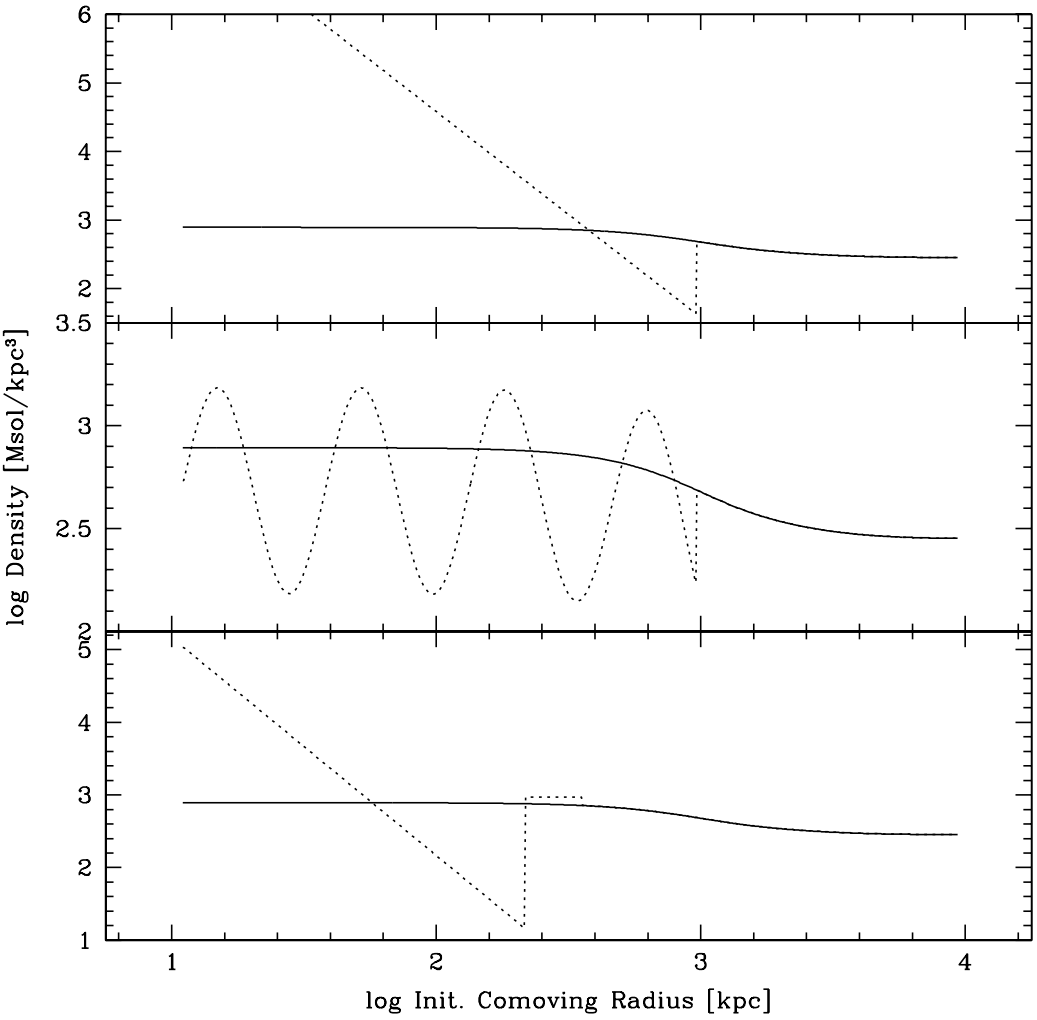

Figure 4.14: This is the initial density profile for simulations 0035/1002 (top panel), 0035/1003 (middle panel), and 0035/1005 (bottom panel). Each of these is compared with the fiducial halo 0035/1001 (solid lines).

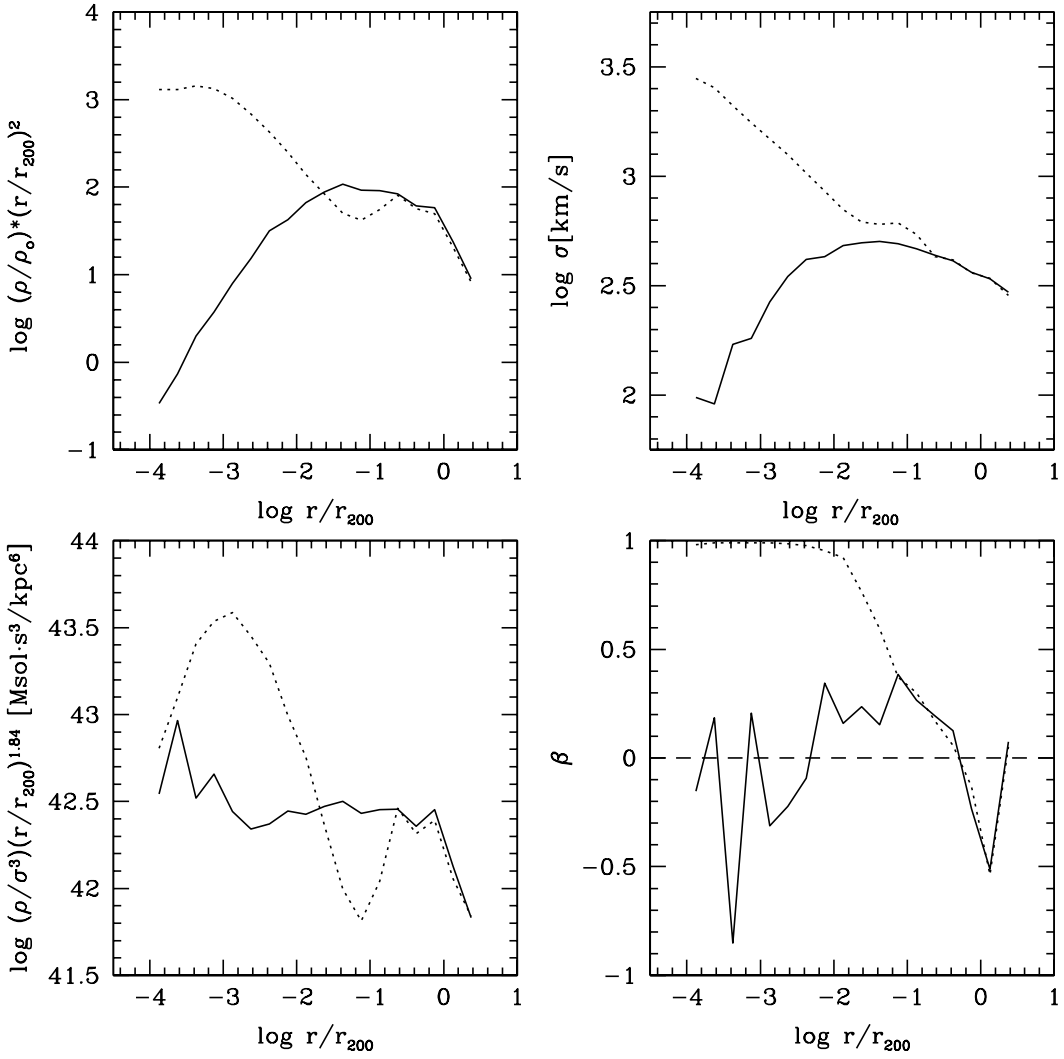

Figure 4.15: This figure compares the final profiles of simulation 0035/1001 (solid line) and 0035/1002 (dotted line).

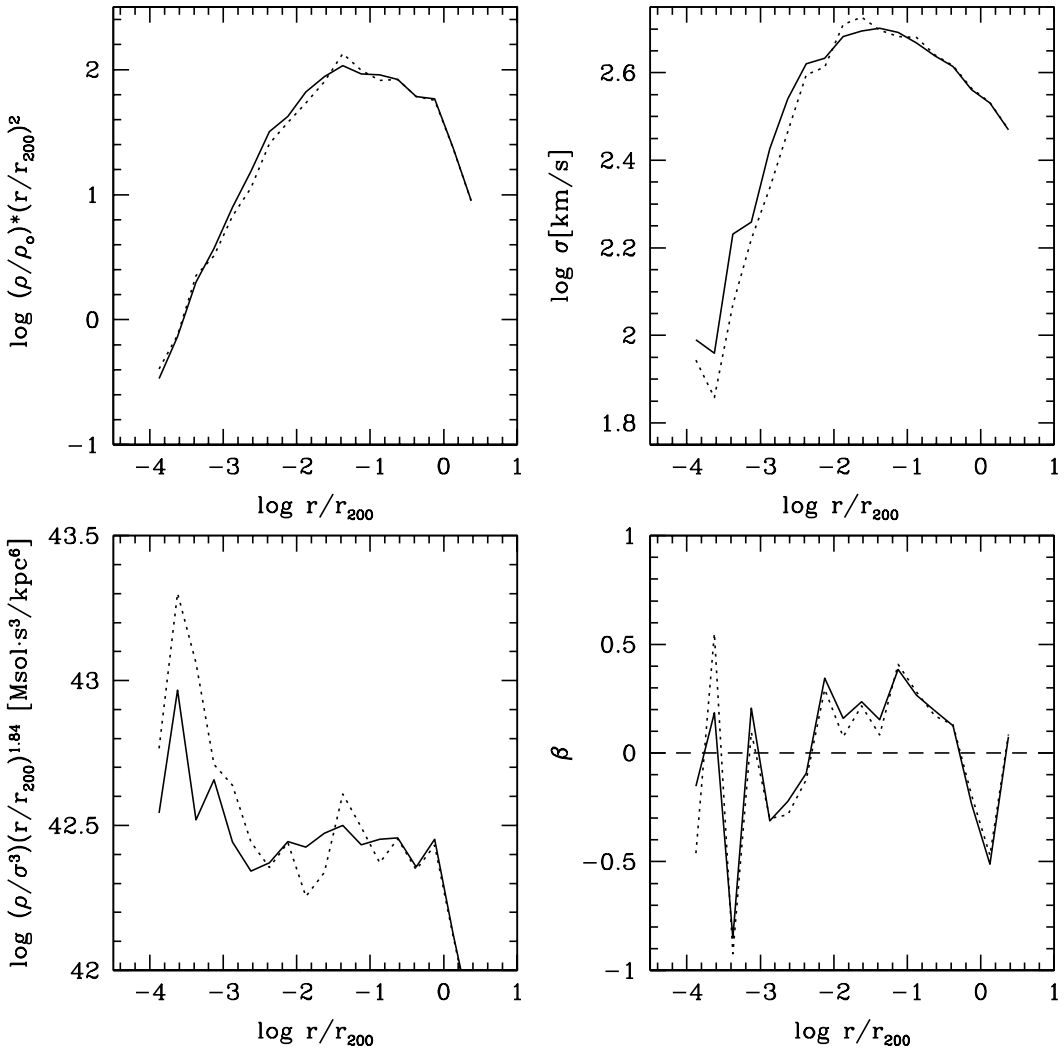

Figure 4.16: This figure compares the final profiles of simulation 0035/1001 (solid line) and 0035/1003 (dotted line).

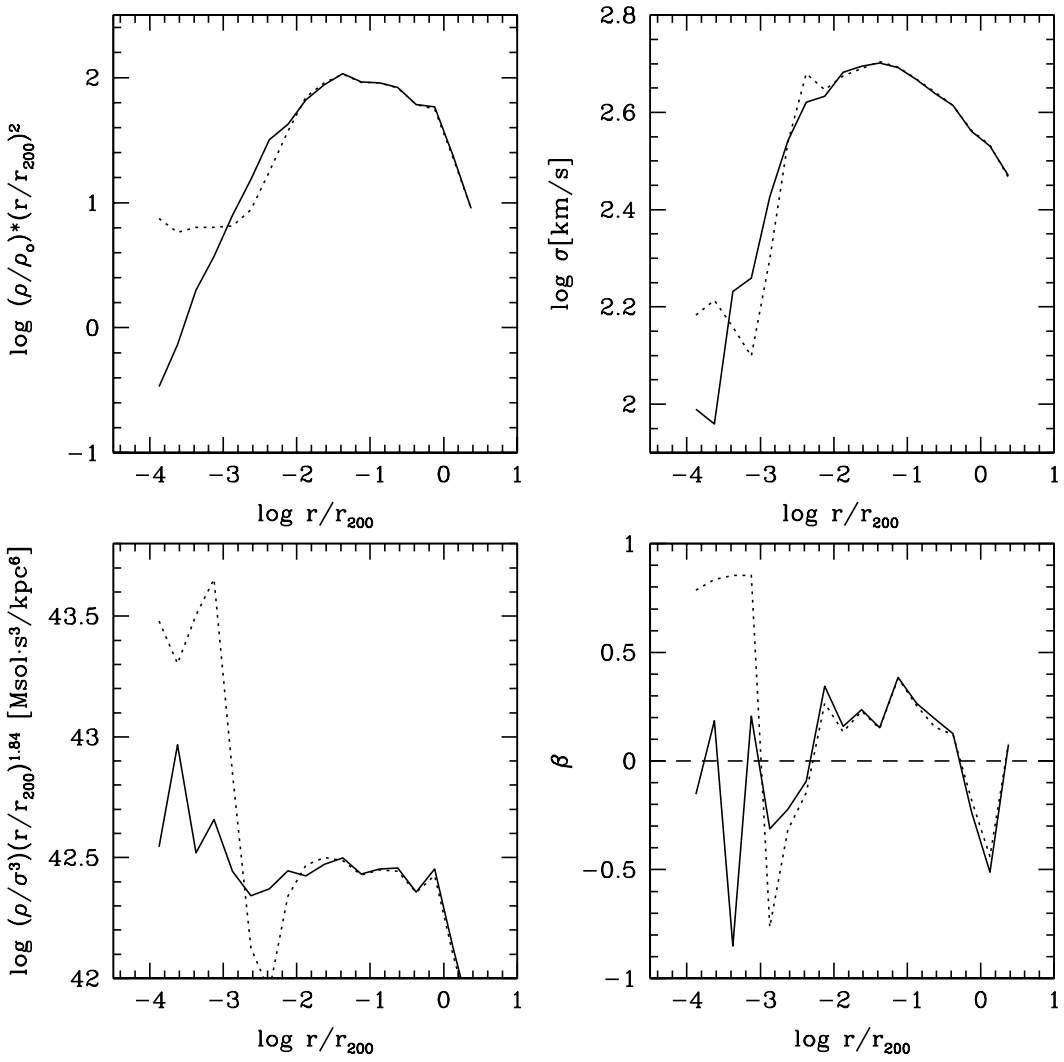

Figure 4.17: This figure compares the final profiles of simulation 0035/1001 (solid line) and 0035/1005 (dotted line).

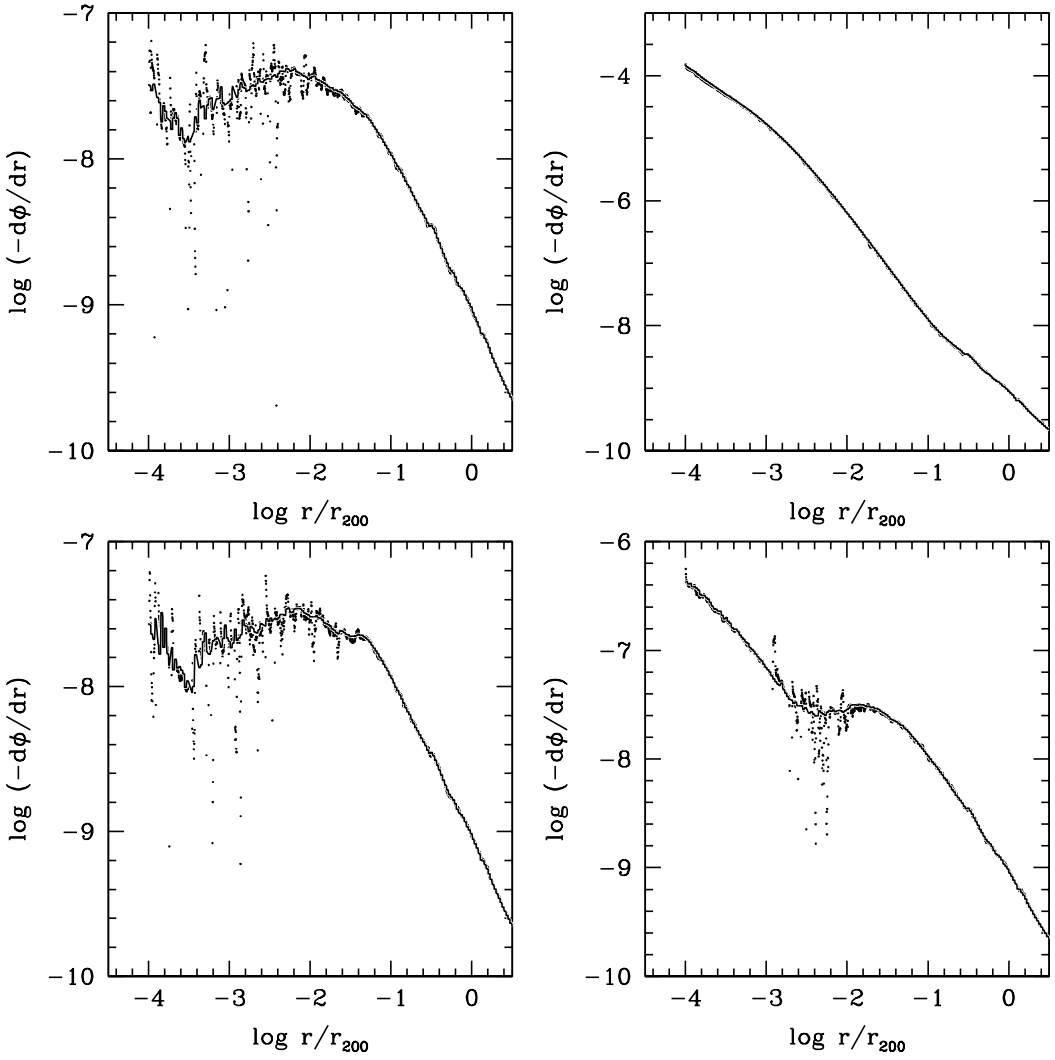

Figure 4.18: The hydrostatic equilibrium (HSE) condition: the LHS and RHS of equation 3.2 are shown as points and the smooth curve, respectively. Where the line traces the plotted points, the halo is in hydrostatic equilibrium. Panels top-left, top-right, bottom-left, and bottom-right represent 0035/1001, 0035/1002, 0035/1003, and 0035/1005.

In the density profile of 0035/1003, however, does agree with 0035/1001. We must instead look at Figure 4.19 to see that the initial conditions are not forgotten. This is evident because there is a sine wave pattern visible in the shells' apo-centers.

All of these ESIM halos appear to form from the inside out. The lower numbered shells are the first to collapse, and these are located closest to the center (see Figure 4.19).

While the inside-out collapse hypothesis was shown to hold (even in simulations with discontinuities), the hypothesis that the density profile only depends on the mass accretion rate has not. Once shell 450 has collapsed (at $z = 4.29$) and to $z = 0$, each of these halos have the same net accretion rate. Despite this, they have different density profiles, especially 0035/1002 and 0035/1005.

When 0035/1002 and 0035/1005 are compared, we discover an interesting result. The initial conditions for these two halos were identical except that 1) 0035/1005 had a small second discontinuity, 2) the discontinuity was located deeper in the halo (i.e. the accretion of the last altered shell happened at $z = 8.33$ instead of $z = 4.29$), and 3) the amount of redistributed mass was smaller.

When we look at the final profiles of these two simulations, it is clear that they are very different. At no radial point do the 0035/1002 profiles agree with the fiducial, non-perturbed halo. 0035/1005 is different; all profiles agree with the fiducial beyond $\log r/r_{200}$=-2.

The cause for this difference is either #2, #3, or combined effect. We put forth that #2 explains the profiles are returning to the fiducial state, and because of #3 it happens quicker (i.e. there is less discontinuity to erase). In other words, the halos profiles are dependent upon the net accretion rate, given that there is ample, subsequent smooth accretion to allow the halo to relax back to the fiducial state.

Therefore, it seems that halos do grow from the inside out and that their density and velocity profiles do depend on the net mass accretion rate – given enough time of quiescent accretion. Despite this, these halos have not completely forgotten their initial conditions.

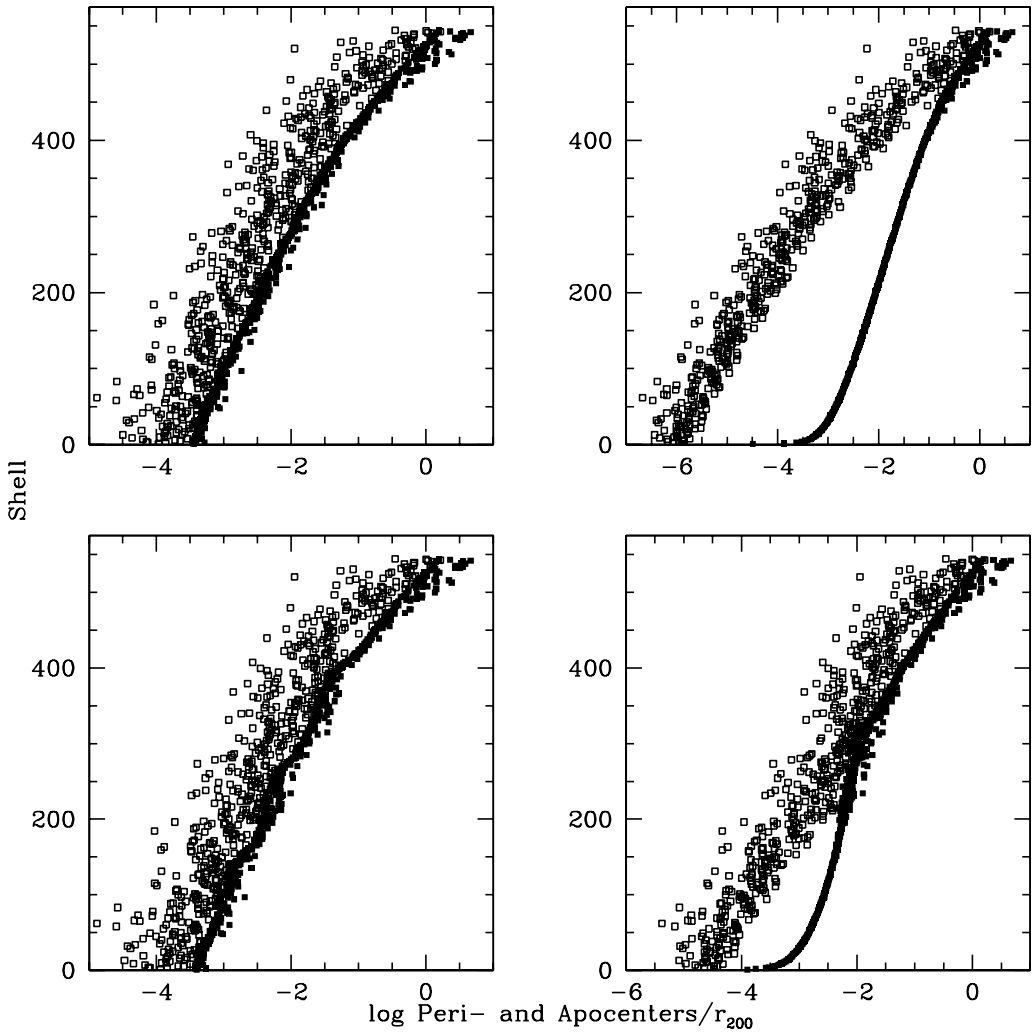

Figure 4.19: This figure shows the peri- and apo-centers for each shell. The peri-centers are open boxes; the apo-centers are filled boxes. Panels top-left, top-right, bottom-left, and bottom-right represent 0035/1001, 0035/1002, 0035/1003, and 0035/1005.

4.11 Conclusion

As has been discussed in Chapters 1 and 3, the semi-analytic collapse of ESIM halos is very limited as compared with the more realistic *N*-body simulations. *N*-body particles are able to move independently in three spatial dimensions and three velocity dimensions; ESIM is limited to the radial spatial dimension and two velocity dimensions (radial and tangential). We use this limitation to study the effect of mass accretion rate has on the final halos.

In ESIM we can alter the main accretion rate (to be non-monotonic) but keep other effects that would accompany accretion in *N*-body simulations, like tidal forces, addition of net rotation, etc., unaltered.

In this chapter I have studied the ESIM collapse technique further. The robustness of the ESIM method were tested, cosmology and physics were altered, and the effects of local discontinuities were observed.

I found that altering the initial seed mass (a test of code robustness) does not alter the density, velocity dispersion, or velocity anisotropy profiles much. The more massive core did increased the very central velocity dispersion. The least massive core seemed to have a less concentrated mass distribution. Despite these changes, all halos are in HSE and have power-law ρ/σ^3 profiles (with altered slopes). Our code is robust again alterations of the inert core: the only significant effect is the altered power-law slope.

Altering the spatial extent of the potential (a test of code robustness) creates significant differences in all of the final profiles. The density, velocity dispersion and anisotropy all have larger values; the ρ/σ^3 profile has a much steeper slope. We believe that is due to the time dependence of the potential. As the extra outer shells expand, the inner potential drops via Equation 4.2. As the code is dependent on this parameter, we make sure that in all ESIM halos have a constant proportion of external shells: 18.96%.

When the initial power spectrum (a cosmological effect) was altered, there was little difference in the final profiles with the steeper $n = 1.5$ spectrum. The shallower $n = 0.5$ spectrum had more power on large scales, which created a more dense halo and a larger velocity dispersion. This simulation also had a more tangential velocity anisotropy profile. The ρ/σ^3 profiles were all well described by power-laws; the altered halos had decreased normalizations and slightly shallower slopes.

I found that in altering the Hubble Constant (a cosmological effect) also created a larger velocity dispersion while not affecting the density profile significantly. The Hubble Constant is used to calculate the normalization of the power spectrum, the constants of the BBKS transfer function, and the location of the virial radius. The velocity anisotropy is unchanged. The phase-space density profiles are both decent power-laws, but the one with the larger Hubble Constant has a significantly steeper slope.

I found that altering the physics of dark matter to allow momentum transfer did not improve the power-law feature of the ρ/σ^3 profile. Momentum sharing between overlapping shells does not help the halo collapse towards a state with a monotonically declining density profile. It yields unphysical results. When the transfer routine was altered, so that it approached the original momentum profile, the final profiles were less erratic, but no more convincing than the fiducial simulation. This was then used to try to aid a broken power-law; it drove the velocity dispersion and anisotropy profiles further from the fiducial state, though the ρ/σ^3 profile was smoothed.

By altering the initial secondary velocity anisotropies (a physical effect), we learned that the dynamical processes involved during the halo collapse are able to preserve the final density profile. Despite this, all kinematic measures (velocity dispersion, velocity anisotropy, and phase-space density) have been significantly altered in order to support this density profile. Thus the halo collapse was not able to regain that radial dispersion hence the final equilibrium state is altered.

I found that altering the velocity and energy distribution of a short radial segment (a local test) significantly altered the final density and ρ/σ^3 profiles, but at different radial locations. The velocity dispersion's normalization and the velocity anisotropy's shape has changed. Earlier (with the altered Hubble constant), we noted that the velocity dispersion's normalization was greatly changed, but the anisotropy was unchanged. As such, these two properties seem uncoupled. It seems that the anisotropy profile's shape is more likely related to the density profile's shape.

When the shell-like satellite accretion (a local effect) was simulated, it was found that all of the profile deviations are limited to a specific radial range. This radial range was not consistent among the profiles: ρ and β at -1.6, σ and ρ/σ^3at -2.2.

Also interesting is that all of the shell-like satellite profiles are similar for regions that collapsed very early or late. At these times, the accretion rates were identical. This

implies that the accretion rate at the time of accretion is very important in determining the final profiles' shapes and normalizations. This effect was examined further in Section 4.10

In that section, we have demonstrate that ESIM halos form from the inside out, even when there are large discontinuities. We also found that these halos are in HSE, but have not yet completely forgotten their initial conditions. The density and velocity profiles depend on the net mass accretion rate only –unless there is not enough time of subsequent, quiescent accretion.

It is not sufficient for an 'instantaneous' change to a smooth accretion rate to change a halo density profile. As was shown, a halo with an altered net accretion rate up to $z \approx 4.5$ does not have time to relax. If the discontinuity is moved back to $z \approx 8.5$, the inner halo has sufficient time to relax and the density profile agrees with the fiducial up to a $\log r/r_{200} = -2$. We did not investigate whether this feature will be removed all together with $z < 0$ evolution or if it would become less dominant as the halo continued to accrete mass on top of the feature.

4.11.1 Summary of Conclusions

In this chapter, many simulations have been presented. Here, I will try to summarize some of the most important points.

- Halos reach a state of hydrostatic equilibrium easily by $z = 0$. Reaching HSE does not require the ρ/σ^3 to be a power-law. In other words, $\rho/\sigma^3 \sim r^\alpha$ is a more restrictive condition than HSE.

- ESIM halos remember their initial conditions to some extent. This is evident in the peri- and apo-centers of the shells. The mass-averaged profiles of density, velocity dispersion, ρ/σ^3, or velocity anisotropy may not show this effect.

- ESIM halos seem to be able to recover slightly from altered initial velocities. When h was changed, the density profile recovered at the cost of the velocity dispersion. When the initial β was purely tangential, the density profile was again similar, but the velocity dispersion and anisotropy were not.

- ESIM halos can also partially recover from altered initial mass distributions. During shell-like satellite accretion, the velocity dispersion's shape was recovered. The mass and and velocity anisotropy remained altered. Also simulation 0035/1005 (altered accretion rate) was able to recover all profiles beyond $\log r/r_{200}$=-2; all profiles were deviated within this location.

- As was seen in Section 4.9, not all of the profile deviations occur at the same radius. Here the density and anisotropy deviations occurred outwards of the dispersion's (and hence the ρ/σ^3's) deviation. In Section 4.8, the radii of the profiles' deviations were also not aligned. For simulation 0018/2234, the density and ρ/σ^3 deviations were located at $\log r/r_{200}$=0. The change in the β profile was most noticeable at -1.6; there were no large deviations in the velocity profile.

  This indicates that each of the measures of halo structure (ρ, σ, and β) are all able to deviate to support the halo's equilibrium. Also, each of these are able to change independently (i.e. which profile is altered and at which radius). This is suggested because the results for Section 4.9 were not able to be predicted from the results of Section 4.8. In the first case, the σ and ρ/σ^3 deviations occurred inwards of the ρ and β deviations. In the second case, the ρ and ρ/σ^3 deviations were located far outside of the β deviation; there was no σ deviation.

- Finally, altering the physics of dark matter so that overlapping shells were able to share momentum did not help the halo recover from a velocity discontinuity. It actually made the profiles worse. Momentum sharing is analogous to collisional dark matter, in the sense that neighboring particles can exchange momentum and energy directly. Our results suggest that introducing a type of collisional physics does not aid in establishing a scale-free ρ/σ^3. This supports the hypothesis that $\rho/\sigma^3 \propto r^\alpha$ is an outcome of collisionless relaxation.

Chapter 5

Cause and Effect in Dark Matter Halo Collapse

A slightly modified version of this chapter will be submitted to the Monthly Notices of the Royal Astronomical Society: Austin, C. G., Williams, L. L. R., Barnes, E. I., Bellovary, J. M. 2009. MNRAS.

Abstract

We use four pure dark matter collisionless simulations—an extended secondary infall model, a standard N-BODY, and two N-BODY runs with non-cosmological initial conditions—to collapse isolated halos and investigate their evolution and final density, velocity dispersions, anisotropy, phase-space density as measured by ρ/σ^3, and the density slope - anisotropy relation. We use the similarities and differences in the initial conditions and the physical processes operating during the collapse to determine how the final halo properties depend on these. We conclude that some final halo properties can be traced back to specific features of collapse; in other words, cause and effect are, to some degree, separable. Most importantly, the anisotropy profile is produced by processes largely independent of those that are responsible for scale-free ρ/σ^3. The rate of evolution and/or mass accretion determines whether ρ/σ^3 becomes scale-free or not, while the availability of three spatial dimensions, which allows for non-radial forces and hence instabilities, produces the typical anisotropy profile and a linear relation between anisotropy and density profile slope. Collapse restricted to one spatial and two

velocity dimensions (as in the secondary infall run) leads to isotropic velocity dispersion throughout the halo.

5.1 Introduction

Many separate collisionless, cosmological *N*-body simulations have found that a 'universal' density profile describes isolated virialized dark matter halos (Cole & Lacey, 1996; Moore et al., 1999; Bullock et al., 2001; van den Bosch et al., 2002; Navarro et al., 2004; Dubinski & Carlberg, 1991; Navarro et al., 1997; Huss et al., 1999; Macmillan, 2006). This 'universal' profile is characterized by an inner log-log slope of ≈ -1, which steepens to ≈ -3 in the outer halo. The whole profile is well described by the analytical fitting formula

$$\frac{\rho(r)}{\rho_{crit}} = \frac{\delta_c}{(r/r_s)(1+r/r_s)^2} \tag{5.1}$$

(Navarro et al., 1997). More recently, Navarro et al. (2004) have found that

$$\ln \frac{\rho_\alpha}{\rho_{-2}} = \frac{-2}{\alpha}[(r/r_{-2})^\alpha - 1] \tag{5.2}$$

fits the profiles better; ρ_{-2} and r_{-2} are the density and radius where the double logarithmic density slope is -2, and the typical value of $\alpha \sim 0.17$.

Another trend in *N*-body dark matter halos is that the velocity dispersion is isotropic in the core, and becomes radially biased as you approach the virial radius (Cole & Lacey, 1996; Carlberg, 1997; Fukushige & Makino, 2001). Barnes et al. (2005) postulated that the scale that marks the transition from isotropic to radially biased velocity dispersion is related to the break in the density profile slope, and that an instability, like a radial orbit instability is responsible for the anisotropy profile, and hence the change in the density profile slope. Using a spherical, semi-analytical collapse technique, they showed that by altering the anisotropy profile (to mimic the radial orbit instability), the density profile changed from a single power-law density profile to a dual power-law profile that mimics the *N*-body universal profile. Thus, Barnes et al. (2005) concluded that a mild radial orbit instability (ROI) gives rise to the characteristic bend in the density profile.

Using *N*-body simulations, Bellovary et al. (2008) confirmed that the ROI leads to a scalelength where the velocity dispersion changes rapidly from isotropic to radially

anisotropic. This scalelength was found to be proportional to the density scale length, thus it was hypothesized that ROI may be responsible for the NFW density profile.

Yet another property of dark matter halos,

$$\frac{\rho(r)}{\sigma^3(r)} \approx \frac{\rho_o}{\sigma_o^3}(\frac{r}{r_o})^\alpha \tag{5.3}$$

has been shown to have a robust scale-free profile shape. The quantity ρ/σ^3 is sometimes referred to as the coarse-grained distribution function, or as the phase-space density, though neither of these names properly describes it. As a short-hand, we will refer to it as the phase-space density. Taylor & Navarro (2001) found that all of their halos were well described by a single power-law with a slope of $\alpha = -1.875$ over 2 decades in radius (equation 5.3). This result has been confirmed by Ascasibar et al. (2004); Dehnen & McLaughlin (2005) with slope values ranging from -1.84 to -1.95. Additionally, Austin et al. (2005) found that semi-analytic halos based on secondary infall produce power-laws with slopes from -1.6 to -2.5, depending on initial conditions. Arad et al. (2004) showed that the profile is present in halos created through substructure accretion. Austin et al. (2005) and Bellovary et al. (2008) have shown that the power-law is present in smoothly accreting, isolated systems. These, taken together, imply that the type of accretion is not a specific condition in creating the power-law ρ/σ^3, as long as it reaches equilibrium. However, it has been shown by Barnes et al. (2006) that this power-law cannot be a generic consequence of equilibrium. Thus, there must be some other constraint or process that is important, but is yet to be quantified.

Finally, Hansen & Moore (2004); Hansen et al. (2005) have shown that there is a relation between the velocity anisotropy and the density profile's slope. They have quantified this relation for several scenarios of halo formation, and concluded that this relationship is linear and 'almost blind' to the specific initial conditions as long as the halo is significantly perturbed and subsequently relaxed.

Despite the considerable amount of research and significant insights into relationships between different properties of dark matter halos, we are only now beginning to understand the physics driving the formation of halos. How does the collisionless relaxation proceed? Are the 'violent' changes in the potential a necessary requirement of collisionless relaxation (Lynden-Bell, 1967), or is chaotic mixing the main mechanism

(Kandrup, 1998; Merritt, 2005). Violent relaxation can be defined as the redistribution of particles' energies due to large, global fluctuations in the potential. Chaotic phase mixing is defined as the 'exponential spreading of initially localized points in phase space' (Merritt, 2005). Alternatively, it has been suggested that halo formation is driven by the mass accretion, and that all the halo properties can be derived from accretion rate alone (Manrique et al., 2003; Gonzalez-Casado et al., 2007).

Ideally, one would want to know how the different processes taking place during collapse, including large changes in the potential (violent relaxation), the radial orbit instability, dynamical friction, chaotic mixing, phase mixing, mass accretion rate, and other processes contribute to the final properties of the halos. In this paper we take a step towards this goal.

We run four, pure dark matter simulations: one using the semi-analytical Extended Secondary Infall Model (ESIM) and three using the commonly-used PKDGRAV *N*-body method. One of our *N*-body models and our ESIM model have cosmological initial conditions (see Sections 5.2.1 and 5.2.2). The other two *N*-body models incorporate non-cosmological initial conditions (see Section 2.3). These proto-halos evolve through physical processes, some of which are common between the simulation methods, while others are different. Comparing and contrasting the evolutions of these models allows us to determine which initial conditions and/or physical processes affect the final halo. While it may seem unlikely to separate processes in such a non-linear situation, we find that some final halo properties can be attributed to specific originating causes.

For each of our four halos, we compare the final profiles of: density, velocity dispersion, velocity anisotropy, and the coarse-grained phase-space density profile. We also plot the velocity anisotropy versus density-profile slope, to compare to previous work. In addition to the final profiles, we also look at time evolution of these simulations' density profiles and phase-space plots.

In Section 5.2 we discuss the *N*-body and the semi-analytic, ESIM methodologies. In Section 5.3 we discuss the final simulation profiles. The discussion of the results and the conclusions are presented in Section 5.4.

5.2 Methods

We set the initial conditions of the semi-analytical Extended Secondary Infall Model (ESIM) and *N*-body (NBODY-S) models to be cosmologically standard and as similar to each other as possible. Our goal is to compare the effects the different evolution methods have on the final halos. We also use *N*-body methods to evolve two simulations that have non-cosmological initial conditions (NBODY-P and NBODY-P2). These four simulations represent very different approaches to equilibrium. Our goal is to determine what conditions or processes create specific features in the final halo profiles.

5.2.1 ESIM Simulation

The semi-analytical method that we used to create the collisionless dark matter halo was developed by Williams et al. (2004b), and is called the Extended Secondary Infall Model (ESIM). 'Extended' refers to modifications on the original Secondary Infall model of Ryden & Gunn (1987). It is important to note that the ESIM method is not meant to describe real dark matter halos; rather, this is a tool used to explore the physics of halo collapse.

The proto-halo is isolated and spherically symmetric. It is formed in a flat, matter-dominated, Einstein-de Sitter universe with $h = 1.0$. The proto-halo's density profile is related to the correlation function and the power spectrum, which is a standard CDM Harrison-Zeldovich modified using a transfer function and normalized such that $\Omega^{0.6}\sigma_8 = 0.5$. However, the specific cosmological model is not important, as long as it is the same for all four simulations.

The proto-halo is divided into shells and allowed to collapse. At the time when a shell detaches from the Hubble flow, a secondary velocity is added to its motion. These secondary velocities mimic real halos' random dark matter particle motions due to the effects of local substructure. The RMS of these velocities is derived from the same power spectrum used to create the proto-halo density profile; this is described in Ryden & Gunn (1987) and the appendix of Williams et al. (2004b). The actual velocity imparted to the shell is chosen from a Maxwell-Boltzmann distribution with a random direction; there is no net rotation, but shells do have tangential velocities.

Each shell is meant to describe the orbits of all particles initially at that radius.

	Particles	Resolution $[M_\odot]$	Softening	$r_{200}[kpc]$	$M_{200}[M_\odot]$
ESIM	572 shells	$1.28 \cdot 10^5$	N/A	499.08	$2.91 \cdot 10^{13}$
NBODY-S	10^5	$4.75 \cdot 10^8$	Optimal, 12.9 kpc	819.2	$3.16 \cdot 10^{13}$
NBODY-S2	10^5	$4.75 \cdot 10^8$	0.1 Optimal, 2.38 kpc	819.2	$2.91 \cdot 10^{13}$
NBODY-S3	10^6	$4.75 \cdot 10^7$	Optimal, 11.05 kpc	864.7	$3.36 \cdot 10^{13}$
NBODY-P	10^5	$4.75 \cdot 10^8$	Optimal, 23.8 kpc	4151.2	$3.72 \cdot 10^{15}$
NBODY-P2	10^5	$4.75 \cdot 10^8$	Optimal, 12.5 kpc	864.68	$3.71 \cdot 10^{13}$

Table 5.1: The parameters for each simulation, and the final virial radius and mass. The final virial radius is where the average interior density is 200 times the critical density. M_{200} is the mass enclosed by the virial radius. Optimal softening is defined by Equation 5.5.

At the time the secondary velocity is imparted, i.e. at turn-around, the shell becomes thick – it acquires a peri- and apo-center. If ESIM had individual particles, their orbits would be rosette-like. As more shells collapse, the shells' energies, apo-centers, and peri-centers are readjusted to be consistent with halo's evolving potential. This is done under the assumption that the collapse is adiabatic: each shell conserves radial and angular actions. Because the shells do not interact directly with each other, but instead respond to the changes in the global potential, the process driving ESIM halo collapse is collisionless relaxation.

The simulation presented in this paper used 572 shells to describe the halo. The first shell detaches from the Hubble Flow at a redshift of 14; its comoving radius at turn-around is $6.95 \cdot 10^{-2}$ Mpc. This is the lowest mass shell in ESIM; its mass, and ESIM's mass resolution, is $1.28 \cdot 10^5 M_\odot$. Shell 572 detaches from the Hubble flow at $z = 0$. This shell has a comoving turn-around radius of 1.831 Mpc, and its mass is $1.27 \cdot 10^{12} M_\odot$.

One of the differences that we exploit is that the ESIM simulation is purely spherical (the three phase-space dimensions are radius, radial velocity, and tangential velocity), whereas *N*-body halos evolve in the full 6-D phase-space, which allows them, for example, to have substructure and to undergo the radial orbit instability.

5.2.2 NBODY-S Simulation

We used the parallel KD tree gravity code PKDGRAV (Stadel, 2001; Wadsley, 2004) to evolve our *N*-body halos. The PKDGRAV time step criterion parameter was set

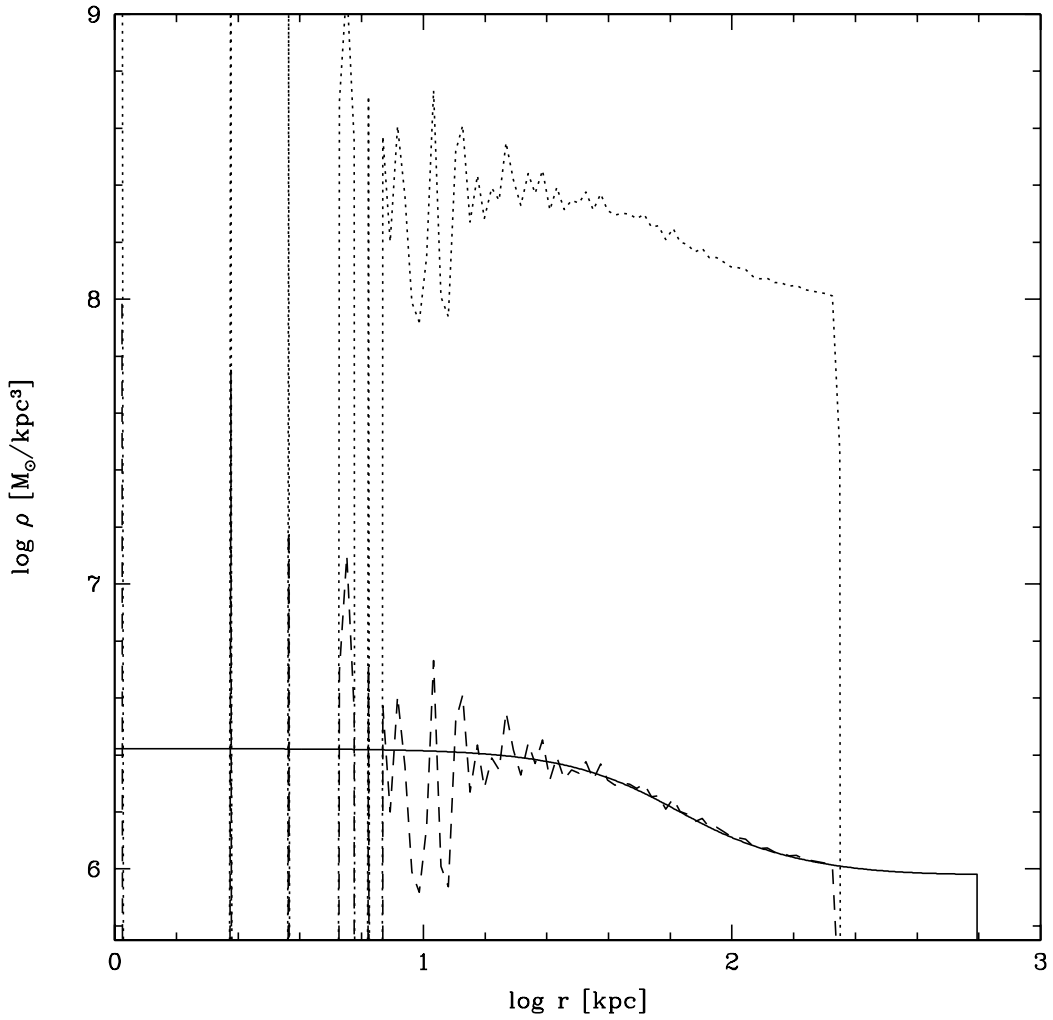

Figure 5.1: The initial density profile for the ESIM halo (solid line), the NBODY-S and NBODY-P2 halos (dashed line), and the NBODY-P halo (dotted line). This is shown in physical units, unlike the normalized quantities used in the rest of the figures. The noise in the central NBODY halos is due to the low particle resolution.

to $\eta = 0.2$ and a force accuracy criterion of 0.55, which are standard parameters for PKDGRAV. We used physical coordinates to evolve the halo from a redshift of 14 to $z = 0$. The initial density profile for the NBODY-S run was obtained from our ESIM proto-halo's density profile by placing particles onto thin, concentric spheres. These initial density profiles are compared in Figure 5.1. The inner discrepancy (within $10^{1.5}$ kpc) between the solid (ESIM) and the dashed (NBODY-S) curves is due to the limited resolution used in the *N*-body code. Aside from this difference, the density profiles are the same.

We start the simulation at a redshift of 14; by this time, all of the particles' Hubble Flow velocities have been retarded due to the interior over-density. The retardation velocity for a top-hat over-density, δ, is given by Bertschinger (1995). The total velocity is then given by:

$$v = (1 - \delta/3)H \cdot r. \tag{5.4}$$

Our proto-halo is not a top-hat over-density, but this approximation proves sufficient.

We cannot directly convert the ESIM velocity perturbations to *N*-body initial conditions. This is because the random velocity perturbations in ESIM are assigned at the turn-around, which is at different times for each shell; the *N*-body initial velocities are all assigned at a single time. Instead, we do not impart any secondary velocities to the *N*-body particles. This is reasonable as the ESIM secondary velocities were meant to mimic the effects of small scale density fluctuations (i.e. sub-structure), which will happen naturally in *N*-body simulations.

To check the reliability of the *N*-body profiles with resolution and softening, we ran a simulation with one-tenth the optimal softening value (NBODY-S2) and a second simulation with ten times the mass resolution (optimal softening, NBODY-S3). We use the optimal softening values as given by Power et al. (2003):

$$\epsilon_{optimal} = \frac{4 \cdot R_{200}}{N_{200}^{1/2}} \tag{5.5}$$

The results are shown in Figure 5.2. The standard resolution halo, NBODY-S, agrees with NBODY-S2 and NBODY-S3 profiles to $\log r/r_{200} = -1.9$, as indicated by the arrow. The NBODY-S profiles should not be trusted interior of this point.

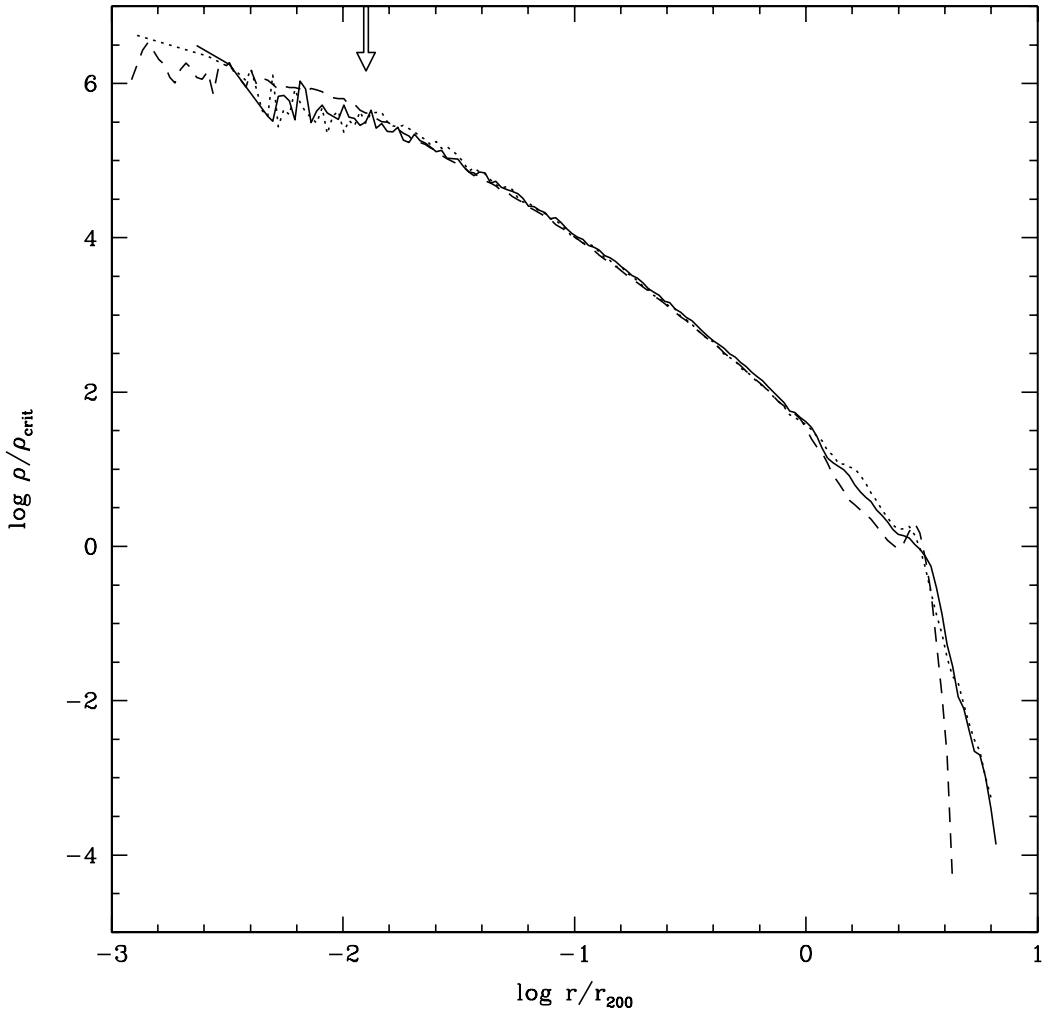

Figure 5.2: The effects of resolution and softening on our simulations at $z = 0$. NBODY-S2 (dotted line) has a softening one-tenth that of optimal. NBODY-S3 (dashed line) has a resolution ten times that of NBODY-S with optimal softening (solid line). These profiles begin to differ from NBODY-S (solid line) inwards of log $r/r_{200} = -1.9$; this is the resolution limit for NBODY-S halo.

Our *N*-body halos do not experience any significant two-body effects between particles. The time scale for the two-body effects in each of our *N*-body simulations is much longer than the Hubble time. Additionally, we confirmed that there are no two-body effects in either NBODY-P (see Section 5.2.3) or NBODY-S by rerunning the same simulations with two different particle masses: 5% and 95% of the original particle mass. Over the course of the evolution no mass segregation was observed.

We also argue that our *N*-body halos do not experience any significant dynamical friction. Dynamical friction can be thought of as a drag experienced by a particle, or a collection of particles (i.e. substructure), moving through a fluid (Binney & Tremaine, 1987). No long-lived substructures are seen in our simulations, hence there is no significant dynamical friction. Because there are no two-body effects, there is also no dynamical friction due to the individual particles.

5.2.3 NBODY-P Simulations

Our NBODY-P simulation was identical to the NBODY-S simulation, except that the mass of the particles was increased 100 times. This simulation develops dramatically different profiles due to the strong initial overdensity, rapid collapse, and therefore very different evolution. The NBODY-P2 simulation was also identical to NBODY-S but with the initial Hubble expansion velocities reduced artificially by a factor of 0.09. As a result, it also collapsed rapidly and gave similar results to NBODY-P despite the very different initial particle mass.

The NBODY-P halo is not cosmologically plausible, as a large, 100x over-dense region would not start collapsing at z =14. Likewise, the region of typical overdensity in model NBODY-P2 would not have negligible Hubble flow at the beginning of its evolution. We use these simulations as tests of extreme initial conditions. In fact, these models are expected to behave more like systems forming in monolithic collapses in a non-expanding background (van Albada, 1982; Merritt & Aguilar, 1985).

5.3 Simulation Results

In this section, we will discuss the following radial profiles for each of the four types of halo collapse: density, velocity dispersion, velocity anisotropy, and the coarse-grained

phase-space density. We also present our results for the velocity anisotropy vs. density slope relationship. The three N-body simulations generate somewhat non-spherically symmetric halos. Since we are interested in radial profiles only, we spherically average the density and velocity dispersion profiles. We would like to remind the reader that these profiles are expected to differ, and these differences will be used to help disentangle the cause-effect relationship in halo formation.

5.3.1 Density

Our ESIM and NBODY-S simulations are shown in Figure 5.3; an NFW profile was fit in the radial range of $\log r/r_{200} = -2$ to 0. These final profiles look very similar: both are well described by NFW profiles with similar concentrations. It is important to note that ESIM halos do not generally produce an NFW density profile (Williams et al., 2004b; Austin et al., 2005), so the similarity between our ESIM and NBODY-S profiles is partly the result of choosing these specific initial conditions. An NFW type profile can also be produced using ESIM and any initial density profile if the initial anisotropy profile is altered to mimic mild ROI effects (Barnes et al., 2005).

ESIM and NBODY-S simulation results differ somewhat in their central profile. The NBODY-S halo, up to the resolution limit, appears to have the NFW cusp with an inner slope ≈ -1. As the ESIM halo's resolution is 3700 times better (in mass), the profile describes the halo accurately to the center. The ESIM's inner profile deviates from an NFW profile–becoming more core-like; this behavior is more like that of Navarro et al. (2004). The core was fit with a power-law interior of $\log r/r_{200} = -3$ with a slope of -0.57.

The NBODY-P and NBODY-P2 halos evolved differently than the other two halos. Due to the huge initial over-density or low initial velocities, the particles' expansion was abruptly halted, they quickly collapsed into a small central volume and then re-emerged on the opposite side of the halo. Many particles' outgoing velocities were high enough so that they were still expanding by $z = 0$. These particles make up the density profile that is visible outwards of the virial radius in Figure 5.3. We fit the NBODY-P and NBODY-P2 halos with a Plummer profile to emphasize the density core:

$$\rho \propto (1/a^3)(1 + (r^2/a^2))^{(-5/2)}. \tag{5.6}$$

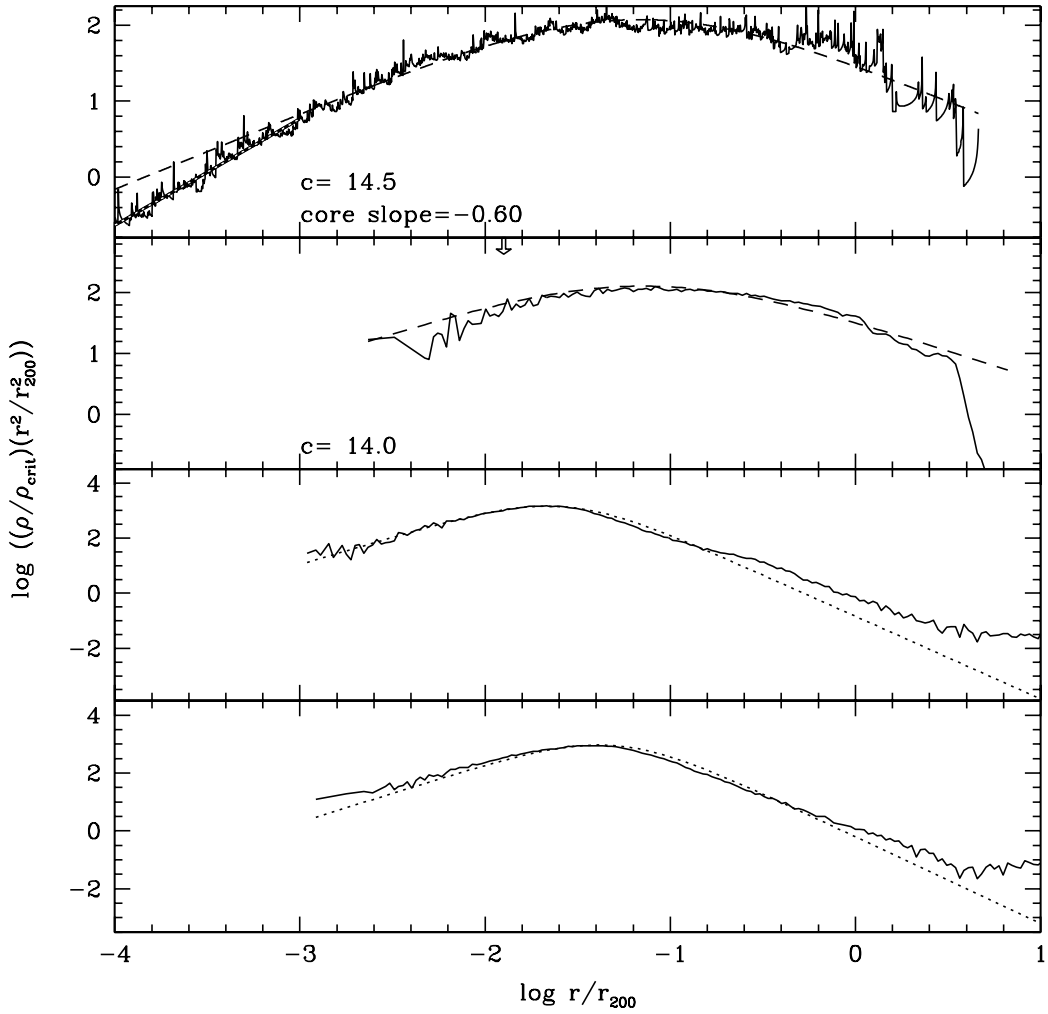

Figure 5.3: The profiles of density multiplied by radius squared at $z = 0$. They are shown this way to emphasize the deviations from the fits. The top panel shows the ESIM halo with an NFW fit (dashed line) as well as a core power-law fit (white dashed line, $\log r/r_{200} < -3$). The second plot shows the NBODY-S halo with an NFW fit; the arrow indicates the resolution limit. The next plots show the NBODY-P and NBODY-P2 halos with Plummer profiles (dotted lines). The fitting range for the NFW and Plummer fits was $\log r/r_{200} = -2$ to 0.

Even though the fit is not very good at large radii, the exact fitting function is not of consequence; what is important is that these profiles have flat density cores and steeply falling density in the outer regions, and that they are very different from those of ESIM and NBODY-S.

It is interesting that NBODY-P and NBODY-P2 reproduced the results of van Albada (1982). Here, dissipationless collapse of a cold, uniform halo resulted in a small central core, with several particles thrown into extended, radial orbits. The velocity structures (as discussed is Section 5.3.4) are also similar: isotropic cores and radial motions in the outer halo.

5.3.2 Velocity Dispersion

The velocity dispersion profiles, $\sigma(r)$, for the ESIM and NBODY-S halos are shown in Figure 5.4. They both peak in the region of $\log r/r_{200} = -1.5$ to -1.0. The velocity dispersion structures of NBODY-P and NBODY-P2 are significantly different: their velocity dispersion peaks in the inner halo and decreases steadily.

These simulations also differ in the dominant velocity dispersion component. As can be seen in Figure 5.4, ESIM has equal amounts of radial and 1-D tangential velocity dispersions throughout the halo, and so is approximately isotropic. NBODY-S, NBODY-P and NBODY-P2 are isotropic near the core and become radially anisotropic towards the virial radius. This is more pronounced in NBODY-P and NBODY-P2 where, once outside the core, particle velocities become quite radial. The radial motions are due to the rapid nature of the collapse.

5.3.3 Phase-Space Density

Our ρ/σ^3 plots, a measure of the coarse-grained phase-space density, are shown in Figure 5.5. Each panel of the plot contains two values in the lower left corner. The first one is the slope of the fitted power-law, the second quantifies the deviations of the profile from the fitted power-law. We chose the RMS of the somewhat smoothed (top hat running average) profile as the measure of the deviation from the pure power-law. The deviations we are interested in are not the random, short-scale 'shot noise', but the longer scale coherent deviations. As can be seen by examining the figure and the calculated RMS

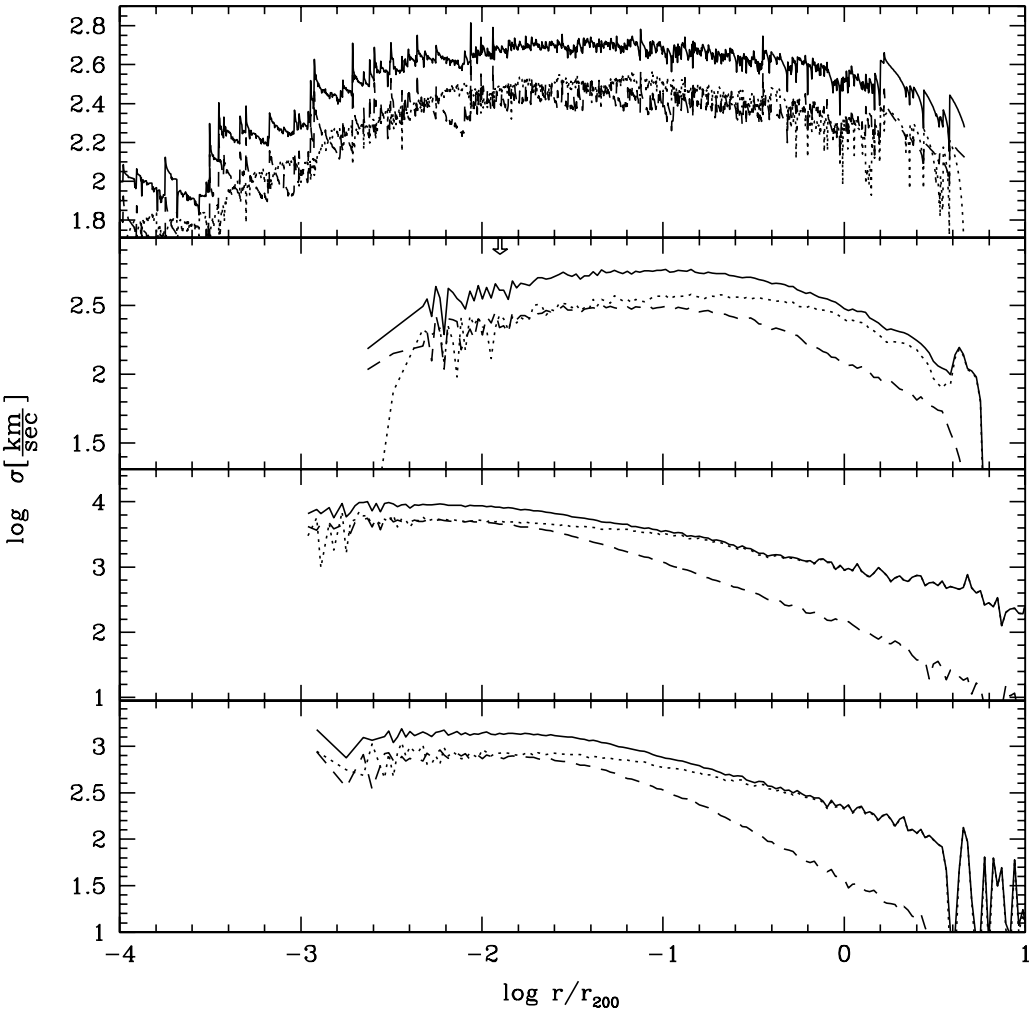

Figure 5.4: The velocity dispersions at $z = 0$: ESIM (top), NBODY-S (second), NBODY-P (third panel), and NBODY-P2 (bottom). The solid, dotted, and dashed lines are the total, radial, and 1-D tangential velocity dispersions. Note that ESIM remains isotropic throughout, unlike the NBODY simulations.

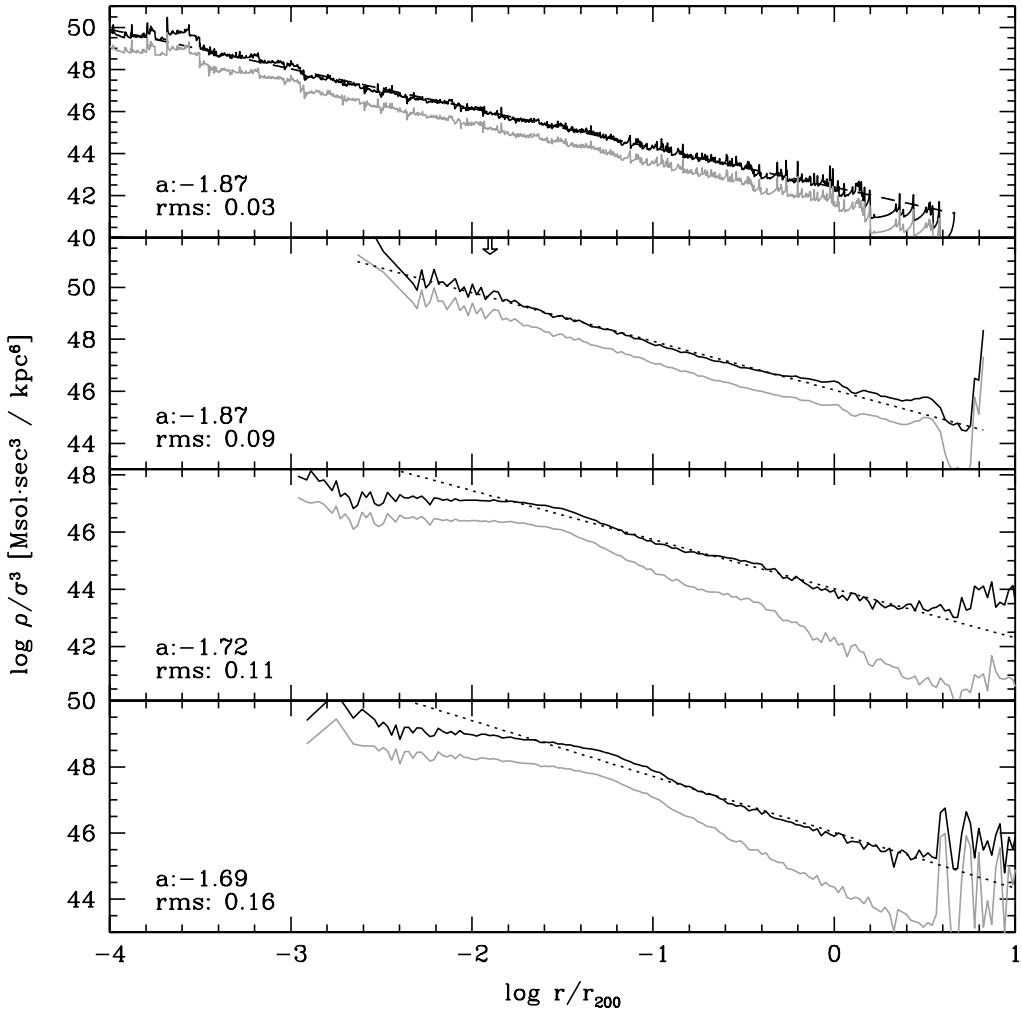

Figure 5.5: These panels respectively show the ESIM, NBODY-S, NBODY-P, and NBODY-P2 coarse-grained phase-space density profiles at $z = 0$. Each profile is fit with a power-law (dotted line) in the region of $\log r/r_{200} = -2$ to 0. The slope and RMS are shown; the RMS is calculated after smoothing as we were interested in the main features and not the noise. The smoothing bin is ≈ 0.3 in units of $\log r/r_{200}$. The gray lines are the phase-space density calculated as in Austin et al. (2005), using $\sigma^3 = (\sigma_\theta^2 + \sigma_\phi^2 + \sigma_r^2)^{3/2}$ instead of the current $\sigma^3 = \sigma_\theta \cdot \sigma_\phi \cdot \sigma_r$.

values, the RMS is not the perfect way to quantify these deviations. Despite that, we will use this measure because it is adequate for the purposes of Section 5.3.5.

The key radial range is where the corresponding density profile changes slope. In NBODY-S, the density changes slope at $\log(r/r_{200}) \approx -1.0$, but the phase-space density profile stays scale-free at that radius. ESIM halo shows similar behavior; its density profile turns over near $\log(r/r_{200}) \approx -1.5$, but the ρ/σ^3 profile is well described by a power-law at this point, as well as over 3 radial decades. This means that in both of these halos the velocity dispersion profiles 'respond' so as to compensate for the slope change in the density profile, keeping ρ/σ^3 a power-law.

Compared to ESIM and NBODY-S's ρ/σ^3 profiles, NBODY-P and NBODY-P2 show qualitatively different behavior: they are not scale-free. In NBODY-P, the density profile changes slope at $\log(r/r_{200}) \approx -1.6$ and -0.5, and there are corresponding phase-space 'bumps' at these radii, because the velocity dispersion profiles do not compensate for the density slope changes. The same is true of NBODY-P2 at $\log(r/r_{200}) \approx -1.4$ and -0.8. These seem to align with the location of phase-space bumps as well as the transition from core isotropy to radial orbits.

In this paper, we calculate the phase-space density using the formula $\rho/\sigma^3 = \rho/(\sigma_r \cdot \sigma_\theta \cdot \sigma_\phi)$. This is the intuitive version, as the phase-space density refers to the volume of velocity space. In Austin et al. (2005), we defined ρ/σ^3 as $\rho/(\sigma_r^2 + \sigma_\theta^2 + \sigma_\phi^2)^{3/2}$. This can be related to the current definition in terms of the velocity anisotropy, β, assuming $\sigma_\theta = \sigma_\phi$. In the current definition, $\sigma^3 = \sigma_r^3(1-\beta)$, while in the previous paper, $\sigma^3 = \sigma_r^3(3-2\beta)^{3/2}$. If $\beta \neq 0$, the two definitions will produce different radial dependencies of $\sigma(r)$ for the same data. For comparison, we show the plots for the previous definition as gray lines in Figure 5.5, and the current definition as black lines.

5.3.4 Velocity Anisotropy and the β - γ Relationship

The velocity anisotropy is a parameter that describes the velocity structure of halos. Anisotropy, β, is defined as

$$\beta = 1 - \frac{\sigma_\theta^2}{\sigma_r^2}. \tag{5.7}$$

Negative β indicates mostly tangential orbits at that radius, while $\beta \approx 1$ indicates the dominance of radial orbits.

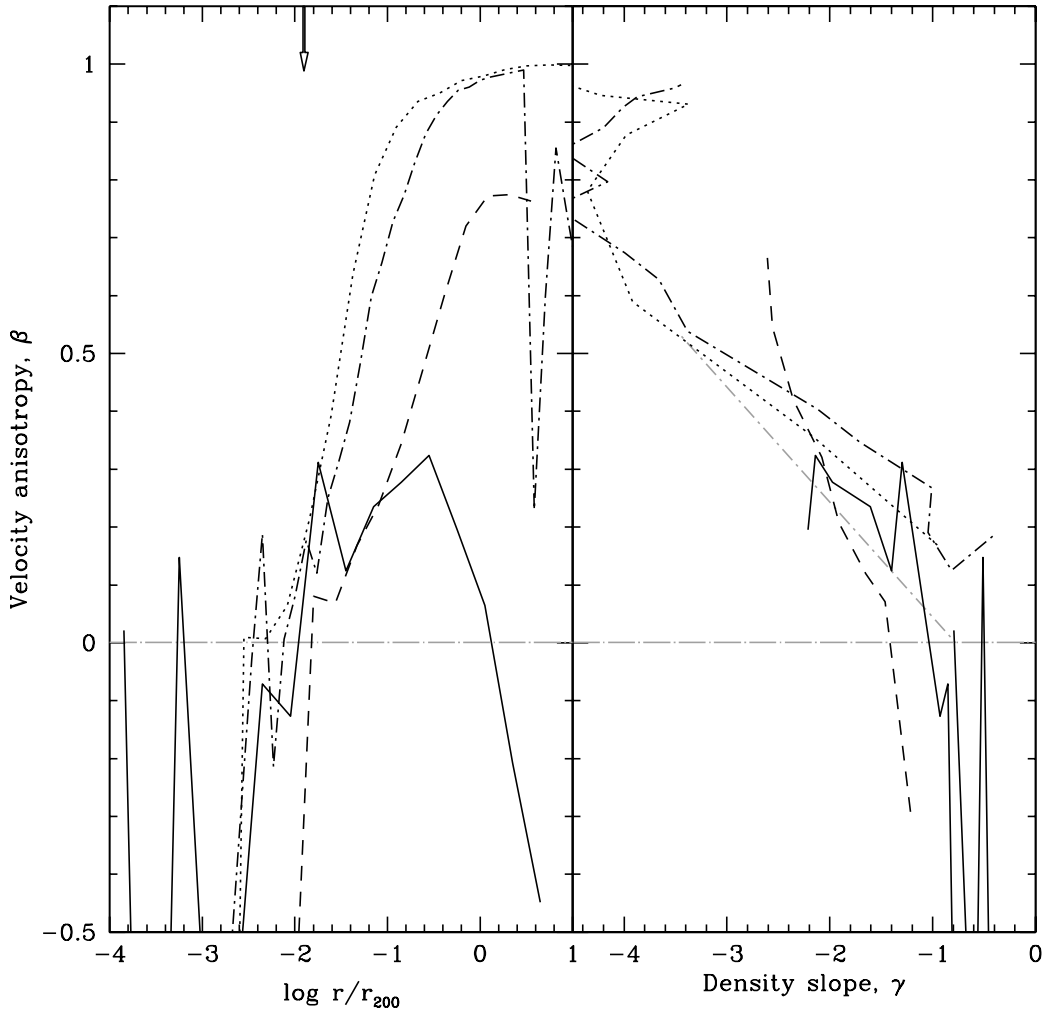

Figure 5.6: The velocity anisotropy (left), as well as the relationship between the velocity anisotropy and the logarithmic density slope (right). The right plot shows the data for points internal to the virial radius (and external to the resolution limit for *N*-body data). The solid, dash, dotted, and dot-dashed lines correspond to the ESIM, NBODY-S, NBODY-P, and NBODY-P2 halos, respectively. The points are binned into groups of 120, 10, 10, and 5. The gray dot-dash line shows the relationship found by Hansen & Stadel (2006).

Despite the similar density profiles in the ESIM and NBODY-S simulations, they are not dynamically identical: the ESIM halo is mostly isotropic, even in the outer halo (see Figure 5.4), while NBODY-S is not. We interpret this difference as a consequence of the process of collapse: in NBODY-S, the three spatial dimensions allow non-radial forces which can cause instabilities. Based on our experiments with ESIM, we claim that in the absence of non-radial forces collisionless collapse would produce an isotropic velocity dispersion profile throughout the halo.

Our NBODY-S, NBODY-P, and NBODY-P2 halos show the $\beta(r)$ behavior characteristic of halos forming in NBODY simulations: isotropic centers and radially anisotropic outer regions, near the virial radius. The transition from isotropic to radial is rapid; this is, possibly, an indication that the radial orbit instability has taken place (Barnes et al., 2005).

To see if the ROI is responsible, we calculate the global anisotropy evolution for the *N*-body halos in Figure 5.7. The global anisotropy is defined as

$$\mathcal{G} \equiv 2T_r/T_\theta \equiv < \sigma_r^2 > / < \sigma_\theta^2 > . \tag{5.8}$$

Based on the arguments of Bellovary et al. (2008), NBODY-S does not undergo ROI processing. This is because there is no large increase in the amount of radial orbits during the early evolution, which would have been represented by a large increase $\mathcal{G}$. This increase in $\mathcal{G}$ is seen in NBODY-P and NBODY-P2. With radial orbits dominating, the likelihood of ROI processing is increased. Previous studies by Barnes et al. (1986), Merritt & Aguilar (1985), and Bellovary et al. (2008) have found that ROI processing has a threshold at $\mathcal{G} \approx 1.4$, 2.5, and $2.0 < \mathcal{G} < 2.97$ respectively. Thus, it appears that NBODY-P and NBODY-P2 do undergo ROI processing as their global anisotropy values exceed these thresholds.

Hansen et al. (2005) have shown that there is a linear relationship between *N*-body halos' β and the slope of the logarithmic density profile, γ. They concluded that this relationship is 'almost blind' to the specific initial conditions as long as the halo is significantly perturbed and subsequently relaxed. The relationship is linear, moving from the central halo at $[\gamma,\ \beta] = [-0.77,\ 0]$ to $[-3.44,\ 0.53]$ in the outer halo. Our data is shown in the right plot of Figure 5.6 with the density slope and velocity anisotropy

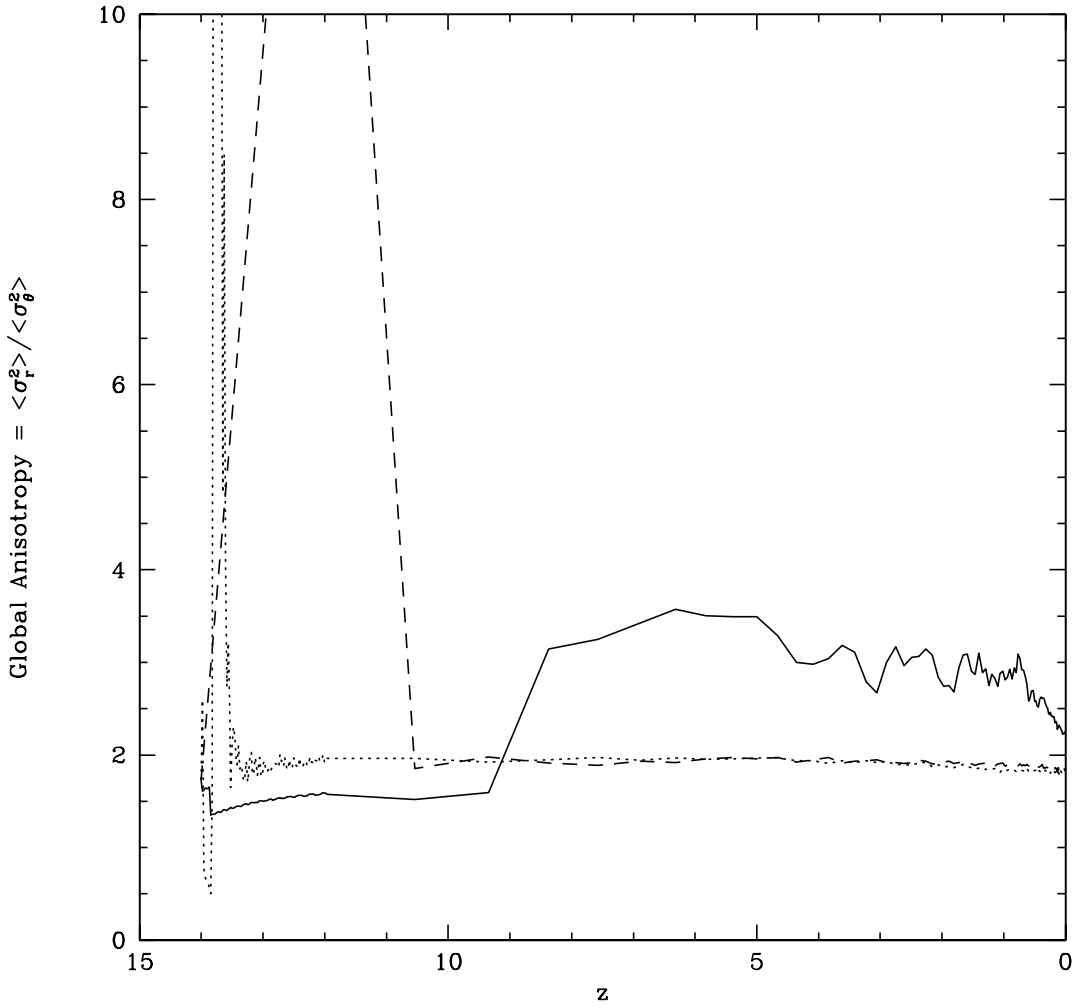

Figure 5.7: This figure shows the evolution of the mass-weighted global anisotropy as is measured by $< \sigma_r^2 > / < \sigma_\theta^2 >$ for the entire system. The solid, dotted, and dashed lines are the NBODY-S, NBODY-P, and NBODY-P2, respectively. This is similar to Figure 7 by Bellovary et al. (2008). NBODY-S does not undergo the ROI effect; NBODY-P and NBODY-P2 may experience ROI as they peak well above $\mathcal{G} = 10$.

value calculated for each radial bin. At the center of the halo, the density profile is shallow and thus represented by the right portion of the profile. All three *N*-body halos reproduce the basic qualitative results of Hansen et al. (2005): as the density slope becomes steeper, the orbits become more radial. Our non-cosmological models reproduce this relationship best; perhaps this is due to the significant relaxation induced by the fast collapse. Our ESIM halo is consistent with being isotropic throughout, but does show a slight trend.

5.3.5 Halo Evolution

Evolution of ρ/σ^3

In Figure 5.8, we show the evolution of the phase-space density power-law fit: the top panel depicts the slope evolution and the bottom panel depicts the evolution of the RMS measure introduced in Section 5.3.3. Since we are mainly interested in how the RMS changes with time, its absolute value and how it compares between different simulations is of lesser importance. The ESIM forms a stable power-law by $z \approx 2$. As it evolves, the slope of the power-law changes slope slowly, staying near the value from Taylor & Navarro (2001), -1.875. During this time ($z = 2$ to 0), the RMS steadily decreases; the halo is evolving, improving the power-law feature. The NBODY-S halo also has a ρ/σ^3 power-law by $z \approx 2$. This also steadily improves (i.e. the RMS decreases) as it approaches $z = 0$. As it evolves, the slope's value approaches ~ -1.9.

NBODY-P and NBODY-P2 show qualitatively different behavior. As these halos evolve, their density core flattens but the velocity dispersion does not compensate for this. This causes the NBODY-P and NBODY-P2's ρ/σ^3 to evolve away from a power-law (i.e. the RMS is increasing). Additionally, this break in ρ/σ^3 moves further into the fitting range with time (as the density core expands slightly). This also causes the RMS to increase near $z = 0$.

Evolution of velocity vs. radius, and density profiles

Figure 5.9 shows the logarithm of the magnitude of the total velocity of particles at four epochs, for the four simulations. In the first column, $z \approx 14$, most of the particles

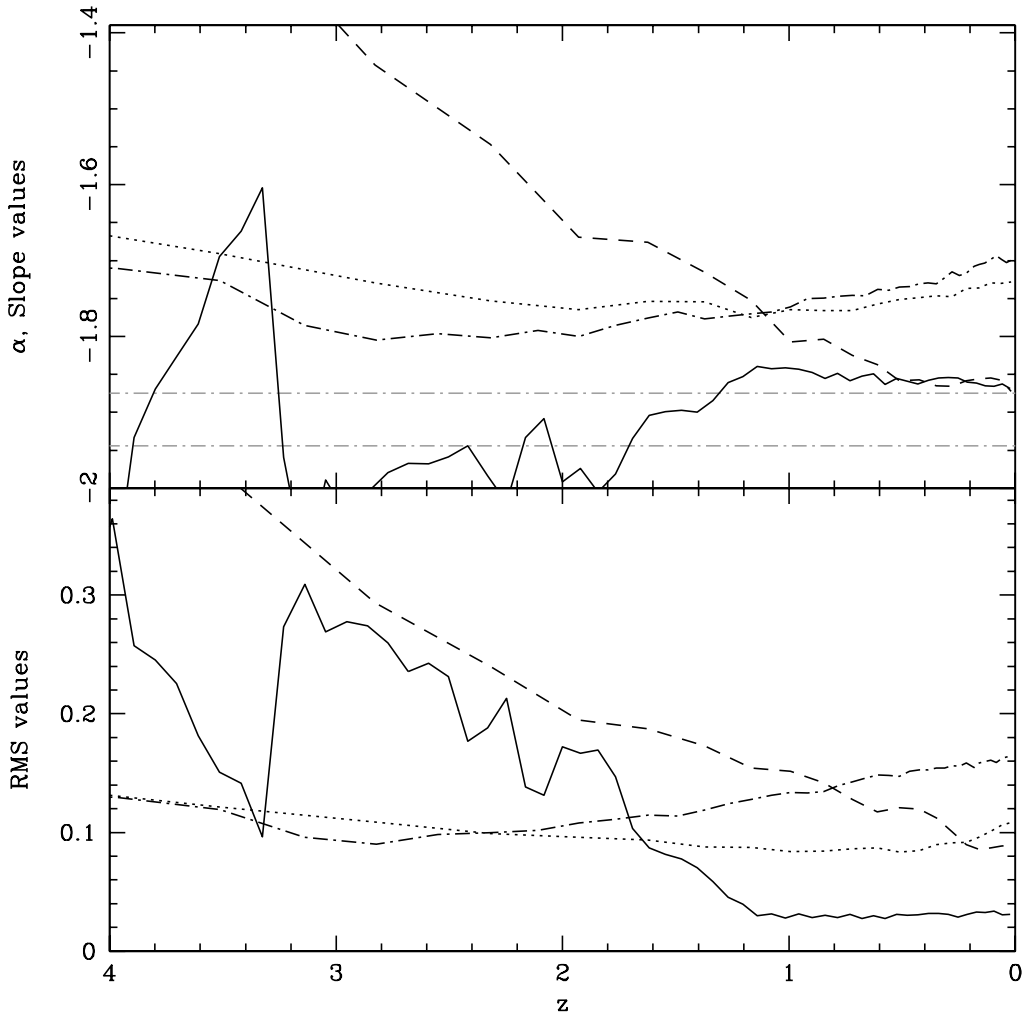

Figure 5.8: The top panel demonstrates how the slope of the power-law fit changes with halo evolution. The special values of -1.875 (Taylor & Navarro, 2001) and -1.9444 (Austin et al., 2005) are indicated as gray dash-dot lines. The bottom panel shows the RMS error (as calculated after smoothing to remove the shot noise) in the power-law fit. The ESIM (solid), NBODY-S (dashed), NBODY-P (dotted), and NBODY-P2 (dot-dashed) data are binned to make the trends evident (bins of 2, 4, 4, and 2).

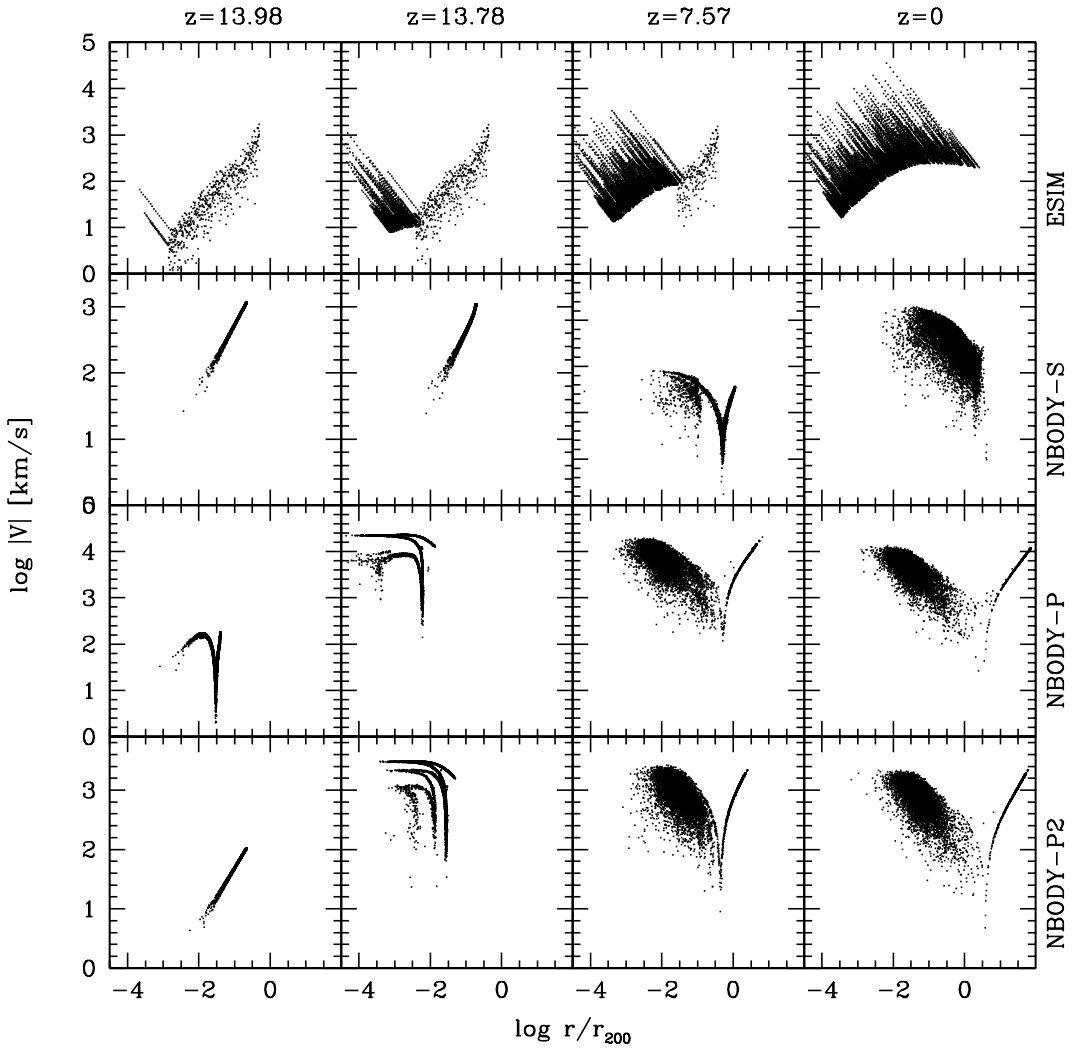

Figure 5.9: These plots show how the phase-space distributions for ESIM (top row), NBODY-S (second row), NBODY-P (third row), and NBODY-P2 (bottom row) change with evolution. The columns correspond to $z = 13.98$, 13.78, 7.57, and 0.0, respectively. Only one-tenth of the N-body particles were plotted, so that the structures are visible. The "V" shape apparent in the N-body halos is due to the various phases of collapse. The right side of the "V" is matter still expanding with the Hubble flow. The bottom of the "V" is turn-around. The left side is more complicated; the particles fall into the halo and re-expand several times until they relax. For the ESIM halos, non-collapsed shells are shown as a single point. Collapsed shells appear as a diagonal line moving from peri-center to apo-center. The x-axis is the final virial radius in physical coordinates: no correction for redshift was made.

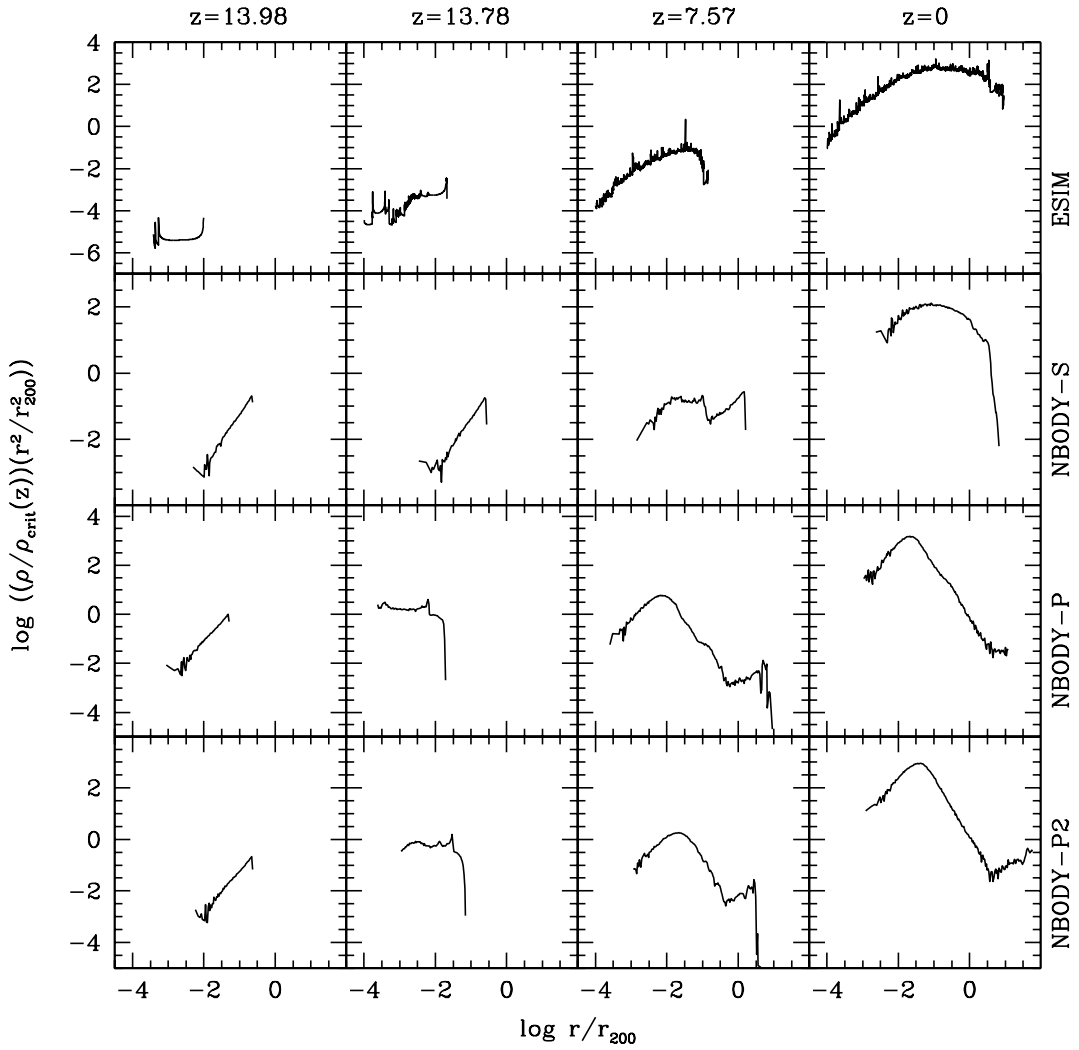

Figure 5.10: These plots show how the density profiles for ESIM (top row), NBODY-S (second row), NBODY-P (third row), and NBODY-P2 (bottom row) change with evolution. The columns correspond to $z = 13.98$, 13.78, 7.57, and 0.0, respectively. The x-axis is the final virial radius in physical coordinates: no correction for redshift was made. The y-axis is dependent on the redshift via the critical density.

show a monotonic decrease in velocity with smaller radius; this is infall following turn-around and decoupling from the Hubble flow. The last two columns are snapshots taken at $z = 7.6$ and $z = 0$. ESIM and NBODY-S have changed during this period, whereas NBODY-P and NBODY-P2 have not, again showing the difference in the rate of evolution between two different types of halos: ESIM and NBODY-S evolve slower compared to NBODY-P and NBODY-P2.

Figure 5.10 shows the density profiles for the same epochs as above. Again we see that the density profiles of NBODY-P and NBODY-P2 have changed little since $z \approx 7$, whereas ESIM and NBODY-S continue to evolve, illustrating the different rates of evolution of the two types of halos.

Evolution of mass accretion or outflow

We also plotted the accretion evolution for our halos. In figure 5.11, we show the net amount of mass inflow (filled symbols) and mass outflow (empty symbols) crossing the spherical shell defined by the final r_{200}. Here we see similarities between NBODY-S and ESIM, and an opposite trend with NBODY-P and NBODY-P2. Both the NFW-like halos are accreting mass interior to that radius, while both the Plummer-like halos are experiencing a mild net mass outflow.

The difference of net mass inflow (seen in ESIM and NBODY-S) vs. outflow (seen in NBODY-P and NBODY-P2) is closely related to the difference in the rate of evolution discussed in 5.3.5 and 5.3.5. Rapid evolution is caused by the large initial overdensity in NBODY-P or the small initial Hubble flow in NBODY-P2. This leads to a very rapid collapse because the free-fall times for most particles are very similar (this is because the initial density profile is nearly a top-hat distribution, see Figure 5.1). As the majority of the mass collapses almost simultaneously, it deepens the potential well considerably. This mass will then re-expand, shallowing the potential well. For the particles that collapse slightly later, they gain energy falling into this deep potential well. By the time these tardy particles are re-expanding, they leave from a shallow potential well. Thus these particles have gained energy and escape the system.

In contrast, the slow evolution experienced by ESIM and NBODY-S apparently gives all in-falling mass enough time to 'thermalize', allowing none of it to leave the halo. Since mass inflow and rate of evolution are the only major evolutionary differences

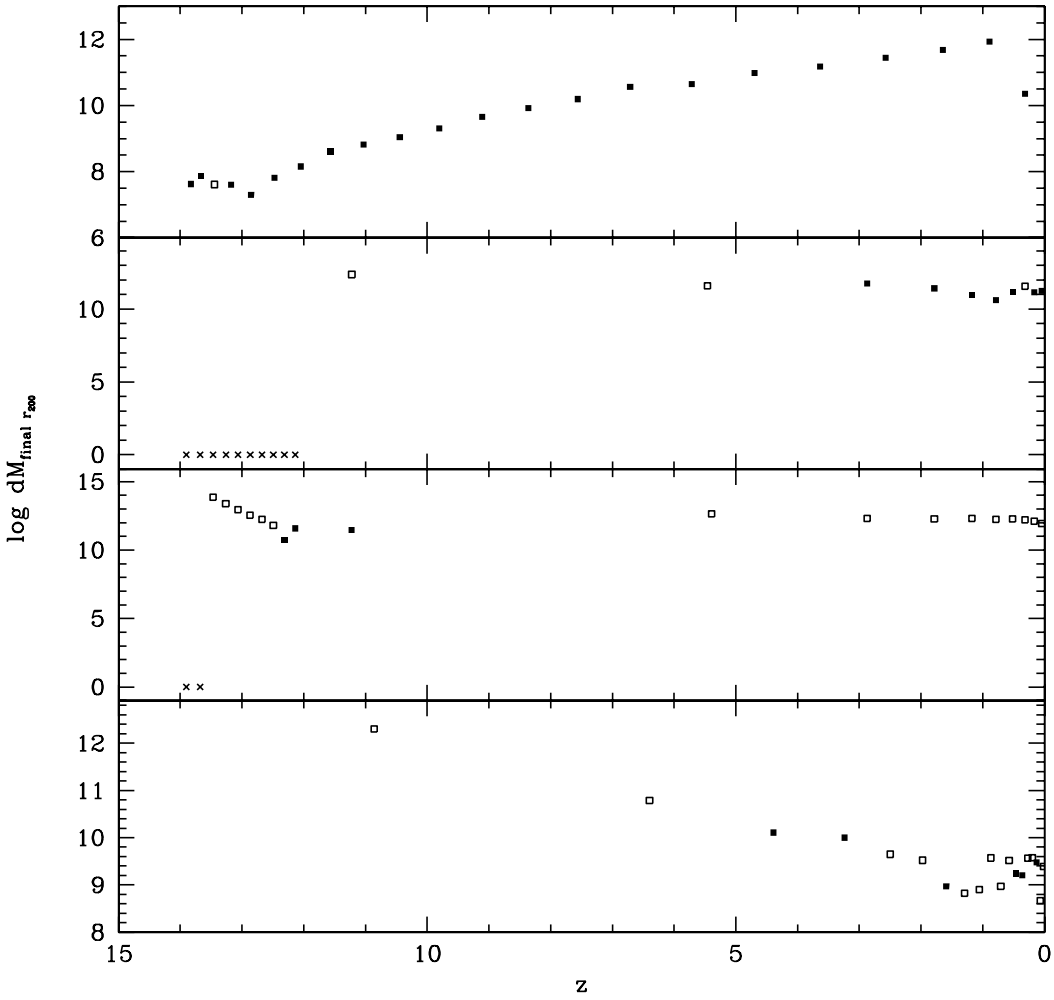

Figure 5.11: The accretion trends for our four halos: ESIM, NBODY-S, NBODY-P, and NBODY-P2 (top to bottom, respectively). The open dots represent mass loss, the filled points represent net mass gain, and the crosses are no change. The data are binned (by 23, 10, 10, and 5 points, respectively) to show general trends. The volume of calculation is defined by the final r_{200} in physical coordinates: no correction for redshift was made.

	Initial Overdensity	Initial Expansion Velocities	# Spatial Dimensions	Collisionless Relaxation	Radial Orbit Instability
ESIM	**Standard**	**Standard**	1	**Yes**	No
NBODY-S	**Standard**	**Standard**	**3**	**Yes**	Maybe
NBODY-P	10x Standard	**Standard**	**3**	**Yes**	**Probable**
NBODY-P2	**Standard**	0.09 Standard	**3**	**Yes**	**Probable**

Table 5.2: The relevant initial conditions, as well as the available processes for each halo. Initial conditions and processes that are similar to our fiducial simulation, NBODY-S, are shown as bold. 'Standard' refers to the values given by a CDM cosmology.

	Accretion	$\alpha(z)$	αRMS(z)	$\rho(z)$, $\|\vec{v}\|(z)$
ESIM	**Positive**	**Decreasing**	**Decreasing**	**Slow**
NBODY-S	**Positive**	**Decreasing**	**Decreasing**	**Slow**
NBODY-P	Negative	Increasing/flat	Increasing/flat	Fast
NBODY-P2	Negative	Increasing/flat	Increasing/flat	Fast

Table 5.3: This shows the behavior of certain halo properties with redshift. Quantities that are similar to our fiducial simulation, NBODY-S, are shown as bold. The accretion column describes the near-present accretion trends: M_{200} is either increasing or decreasing. Columns 2 and 3 refer to Figure 5.8 and describe the values' trends as they approach $z = 0$. Column 4 refers to Figures 5.9 and 5.10; fast indicates that the halo reached equilibrium quickly (i.e. $z \approx 8$).

between the two types of halos, we suggest that these related effects are responsible for the difference in the final halo properties of ESIM and NBODY-S vs. NBODY-P and NBODY-P2 simulations. This is in agreement with Gonzalez-Casado et al. (2007), who find that the density and velocity dispersion profiles depend on the mass accretion history.

5.4 Discussion and Conclusions

The four halos used in our work had similarities and differences in the initial conditions and the dynamical processes available to them. The semi-analytical simulation, ESIM, is strictly spherical and does not allow any processes that require three spatial dimensions or non-radial forces, for example, radial orbit instability (ROI). Our three NBODY simulations allow for evolution in all three spatial dimensions, and hence can have ROI and other instabilities. NBODY-S was our standard simulation, with the initial

	ρ	σ	$\rho/\sigma^3 \sim r^\alpha$	β	γ vs β
ESIM	**NFW w/ c=14.5**	**Peaked**	**α=-1.86**	Isotropic	**Increasing**/Flat
NBODY-S	**NFW w/ c=14**	**Peaked**	**α=-1.87**	**Typical**	**Increasing**
NBODY-P	Plummer	Cored	Broken power-law	**Typical**	**Increasing**
NBODY-P2	Plummer	Cored	Broken power-law	**Typical**	**Increasing**

Table 5.4: These are the final profile properties that we use as diagnostic tools. Final profiles that are similar to our fiducial simulation, NBODY-S, are shown as bold. Column 1 describes which fit, from Equations 5.1 or 5.6, describe the density profile better. Column 2 indicates whether the velocity dispersion profile has a non-centrally located maximum or a cored profile. Column 3 shows that 2 of our 4 halos show a power-law in ρ/σ^3. Column 4 shows that our *N*-body halos are isotropic in the core and become radially dominated at the virial radius; this is the typical behavior. The last column shows that the *N*-body halos show the trend found by Hansen et al. (2005): β increases while γ decreases.

conditions as similar to ESIM as possible. NBODY-P differs from NBODY-S only in its initial density profile: it is 100 times more over-dense, and the halo collapse happens very quickly. NBODY-P2 also collapses quickly due to its artificially small expansion velocities.

Our goal was to use these to our advantage to determine which processes are necessary for the formation of scale-free phase-space density, the NFW-type density profile and the $\beta - \gamma$ relation. To do this, we looked for similarities between the inputs and processes (Table 5.2), the evolutionary trends (Table 5.3), and the final results (Table 5.4). To facilitate comparison we have highlighted in boldface all the instances of initial conditions, dynamical processes and final halo properties that were the same as in our fiducial run, the NBODY-S simulation. Not every entry in these three Tables is in boldface; the similarities and differences is what we will exploit to isolate cause and effect in halo collapse.

We conclude that at least to some degree, the various final properties of halos are the result of different initial conditions or processes that operate during collapse. In other words, effects can be traced to separate causes. Most importantly, the $\beta(r)$ profile is produced by processes largely independent of those that produce scale-free ρ/σ^3. Below we show that, (1) the rate of evolution and/or mass accretion determines whether ρ/σ^3 becomes scale-free or not, and (2) the availability of the full three spatial dimensions dictates the radial shape of the anisotropy $\beta(r)$ profile and allows for a relation between

β and γ.

(1) To find the necessary element in creating the phase-space power-law, we looked for inputs or processes that were the same for NBODY-S and ESIM (as these are the two halos that end up having $\rho/\sigma^3 \sim r^\alpha$), but different for NBODY-P and NBODY-P2. As already mentioned in the previous section, of all of the listed processes, only the accretion rate and the rate of evolution 'correlated' with the scale-free ρ/σ^3 of the final halos. NBODY-S and ESIM evolve slowly and undergo mass inflow at their virial radii in the latter stages of evolution, and end up with scale-free ρ/σ^3. In contrast, NBODY-P and NBODY-P2 evolve fast, undergo mass outflow, and end up having breaks in their ρ/σ^3 power-law. It is also worth noting that even though NBODY-P and NBODY-P2 had very different initial conditions, they ended up with very similar density and anisotropy profiles. This leads us to conclude that the actual initial conditions are irrelevant in creating the density, velocity dispersion, and ρ/σ^3 profile shapes, so long as the resulting rate of evolution and the mass accretion rates are the same. This supports the findings of Gonzalez-Casado et al. (2007): the halo profiles are determined by the mass accretion rates.

We conclude that slow vs. fast collapse, which can be induced by changing initial conditions, result in halos either having a scale-free ρ/σ^3, or not. Thus, not all collisionless collapses lead to scale-free ρ/σ^3. We have not quantified what exactly we mean by "fast", or "slow"; this is left for a future work.

(2) While the character of ρ/σ^3 seems to be governed by the rate of collapse, something else is responsible for the $\beta(r)$ profile and the existence of the linear $\beta-\gamma$ relation. Because all three NBODY halos have roughly similar $\beta(r)$ and $\beta-\gamma$ relationships, while the ESIM halo is approximately isotropic, we conclude that the three spatial dimensions are a necessary condition for the formation of the anisotropic $\beta(r)$ profile and the linear $\beta-\gamma$ relation. We speculate that three spatial dimensions are important because they allow non-radial forces to operate, and lead to instabilities, such as the radial orbit instability, even though ROI itself may not operate in all of our NBODY collapses (Bellovary et al.). These instabilities in turn lead to non-spherically symmetric shapes of the whole halo or its inner region. In fact, the halos of all three of our NBODY simulations develop elongated bar-like or triaxial shapes. On the other hand, our ESIM simulation presented in this paper, as well as other ESIM simulations with

different initial conditions produce halos with nearly isotropic final velocity dispersions. It is not obvious why this should be the case because in addition to one spatial dimension ESIM simulations have two velocity dimensions, so anisotropy could, in principle, develop. In fact, some ESIM halos start out being anisotropic, but then evolve towards isotropy. Whatever the exact mechanism that makes final ESIM halos isotropic while NBODY halos anisotropic, it must be sensitive to the number of spatial dimensions and non-radial forces.

In addition to the main results presented above, we also describe more tentative conclusions.

Aside from determining the nature of the radial profile of ρ/σ^3, the rate of evolution also has an effect on the density and velocity anisotropy profiles. Fast collapse appears to result in halos with flat density cores, and steeply declining outer envelopes, like those of NBODY-P and NBODY-P2. Comparing the three halos that evolve in 3D, the two that evolve fast develop anisotropy profiles that transition from isotropic to radially anisotropic very rapidly, while NBODY-S shows a more gradual transition. Thus slow collapses in the full 6D phase-space appear to lead to density and anisotropy profiles that exhibit gentler radial changes in slope. Fast collapses produce halos with more dramatic slope changes in both the density and anisotropy profiles. This conclusion can also be reached by comparing the well-known early numerical results of van Albada (1982) and Merritt & Aguilar (1985) who formed galaxies with de Vaucouleurs profiles and Osipkov-Merritt type anisotropies, with the results of halo formation in cosmological setting, such as NFW.

Our ESIM simulation, which exhibits no fast, or large changes in the potential, demonstrates that rapid changes in the potential, as implied by 'violent' relaxation are not a necessary ingredient of collisionless collapse and virialization. To a lesser degree the same statement is true of the NBODY-S simulation, so there is no evidence that violent relaxation is necessary process in the formation of dark matter halos.

Finally, we note that because all of our halos retain at least some memory of the initial conditions and the process of collapse, the collisionless relaxation which leads to the final equilibrium state in never complete.

e thank Tom Quinn for giving us access to PKDGRAV and for useful discussions. We would like to thank Eduard Salvador-Sole for dialog that took place during this research

and the Niels Bohr Institute for hosting the Dark Matter Workshop in 2007. This work was supported in part by NSF grant AST 03-07604 and the NASA Astrophysics Theory Program grant NNX07AG86G. CA received support from the U of MN doctoral dissertation fellowship. JMB thanks the NSF Graduate Research Fellowship Program. Computing resources were made possible through a grant from the Student Technology Fee of the University of Washington.

Chapter 6

Summary of Conclusions

Currently, observations of clusters of galaxies give us indirect limits on the mass and energy distributions of dark matter. These current techniques for deriving the dark matter distribution will be improved and will give better information and elucidate additional dark matter proprieties. An example of this is the recent study by Hansen & Piffaretti (2008). They have provided the first observational limits on the velocity dispersion and anisotropy. This was done with X-ray cluster observations and the assumption of HSE. Directly observing the dark matter density and velocity profiles (via WIMP annihilation in our galaxy (Host & Hansen, 2007)) is not possible yet.

While astronomers work to improve their observational limits and techniques, simulations are able to explore the process of non-linear dark matter collapse. The simulation results generally agree with the current observations and will predict future observations.

In this work, I have focused on two type of simulation techniques – ESIM and N-body – which evolve under different physical processes. Each of these techniques were used to construct the collapse of a single dark matter halo with varying initial conditions. There are no baryons in these simulations.

In this study, we have concentrated on isolating and characterizing the cause-and-effect of dark matter halo collapse. The dynamical processes we investigated involved are violent relaxation, the radial orbit instability, dynamical friction, and phase-mixing. We specifically address the source of the scale-free nature of ρ/σ^3, density profile, and the $\beta - \gamma$ relationship.

6.1 Conclusions from Chapter 3

N-body dark matter halos have a coarse-grained phase-space density, ρ/σ^3, that is a power-law in radius, even though the density profile is not (Taylor & Navarro, 2001). To determine if the scale-free nature of ρ/σ^3 is peculiar to *N*-body halos or is a more generic outcome of collisionless gravitational collapse, we turned to a different method of generating equilibrium halos: the Extended Secondary Infall Model (ESIM).

Despite the differences between *N*-body and ESIM methods and the differing final density profiles, both types of halos are characterized by a scale-free ρ/σ^3 profile. We speculate that this feature is an outcome of the one piece of physics shared by the two methods: violent relaxation. At the very least violent relaxation is a sufficient, if not the necessary condition needed to produce $\rho/\sigma^3 \propto r^\alpha$. We tested this hypothesis in subsequent chapters.

This topic is important because if this is a generic feature of collisionless halos, it is an additional constraint on the halo structure.

We have also shown that the ESIM ρ/σ^3 feature is very resilient, and one must concoct rather extreme cases in order to end up with ρ/σ^3 that shows deviations from a single power-law (Section 3.2.8).

Unlike the *N*-body halos, the slopes of the ESIM ρ/σ^3 power-law features are not constant. We find a range of values from -1.6 to -2.2, while TN01 find that the same $\alpha = -1.875$ described all three of their *N*-body halos. In our study, α_{fit} was not uniquely determined by any single property of halos, such as mass, epoch of formation, or amplitude of random velocities.

This advances us slightly further in our understanding of the collisionless collapse of dark matter halos. We show that the ρ/σ^3 power-law is a robust feature in an independent test. The properties (i.e. slope) of the ρ/σ^3 are dependent on the initial conditions.

Additionally, it was shown that the ESIM density profiles are not the universal NFW profile. For galactic-sized halos, the density profile is better fit by a power-law. For group and cluster-sized halos, the density profiles were more curved. Despite these two different density regimes, all halos had a ρ/σ^3 power-law profile.

6.2 Conclusions from Chapter 4

In this chapter we expanded on the studies of Chapter 3. We altered many different initial conditions as well as the physics of collapse. The goal of this was to a) test the robustness of the ESIM code, b) identify the effects of different cosmologies on the final halo, c) determine the effects of collisional dark matter, and d) determine the effect of local disturbances (altered accretion rates, shell-like satellites, etc.).

From this agglomeration of simulations, there are several conclusions. First, halos reach a state of hydrostatic equilibrium easily by $z = 0$. Despite this, not all halos displayed a ρ/σ^3 power-law. Thus reaching HSE does not require the ρ/σ^3 to be a power-law. The $\rho/\sigma^3 \sim r^\alpha$ result is a more restrictive condition than HSE.

Second, ESIM halos remember their initial conditions to some extent. This is evident in the mass-averaged profiles of density, velocity dispersion, the ρ/σ^3slope, and the peri- and apo-centers of the shells. The velocity anisotropy seems the least susceptible to the initial conditions.

While the initial conditions are partly retained, there is some evidence that ESIM halo relaxation erases some initial conditions. When the initial velocities were changed by altering h, the density profile was mostly unaltered at the cost of the velocity dispersion. The density profile was again similar but the velocity dispersion and anisotropy were not when the initial β was purely tangential.

This trend is also evident for altered mass distributions. Simulation 0035/1005 demonstrates this. It had an extremely altered accretion rate and was able to recover all profiles outside of $\log r/r_{200}$=-2. Simulation 0035/1002 was similar but the profiles were unable to recover. The primary difference between these two simulations was that the former simulation had more time to recover after its last altered shell. This indicates that, given enough time of quiescent accretion, the halo profiles will mend.

Third, as was seen in Section 4.9, not all of the profile deviations occur at the same radius. Here the density and anisotropy deviations occurred outwards of the velocity dispersion and ρ/σ^3deviations. In simulation 0018/2234, the density and ρ/σ^3 deviations were aligned at $\log r/r_{200}$=0. The change in the β profile was most noticeable at -1.6; there were no large deviations in the velocity profile.

This indicates that each of the independent measures of halo structure (ρ, σ, and

β) are all able to deviate to support the halo's equilibrium. The deviations are not limited to a specific radius or a specific recipe (i.e. if the density deviation is interior, the anisotropy deviation should be exterior. This latter result is suggested as the results for Section 4.9 were not able to be predicted from the results of simulation 0018/2234.

Finally, I altered the physics of dark matter so that overlapping shells were able to share momentum. This is analogous to collisional dark matter and our results suggest that introducing collisional physics does not aid in establishing a scale-free ρ/σ^3. This supports the hypothesis that $\rho/\sigma^3 \propto r^\alpha$ is an outcome of collisionless relaxation.

6.3 Conclusions from Chapter 5

In this chapter I expand on the previous chapters: I now compare the ESIM collapse technique directly with the *N*-body method. The four halos used in our work had similarities and differences in the initial conditions and the dynamical processes available to them. The ESIM halo is strictly spherical and does not have any processes that require three spatial dimensions, for example, radial orbit instability (ROI). Our three *N*-body simulations allow for evolution in all three spatial dimensions, and hence can have substructure and ROI. NBODY-S was our standard simulation, with the initial conditions as similar to ESIM as possible. NBODY-P varies from NBODY-S only in its initial density profile: it is 100 times more over-dense, and the halo collapse happens very quickly. NBODY-P2 also collapses quickly due to its artificially small expansion velocities.

We use these differences to our advantage. We are able to identify causes for some of the final halo properties. This was done by looking for similarities between the inputs and processes, the evolutionary trends, and the final results.

It was found that the rate of evolution and/or mass accretion determines whether or not ρ/σ^3 is a power-law. It also affects the shape of the density profile. This was determined as only these two processes correlated with the ESIM and NBODY-S, while being anti-correlated with NBODY-P and NBODY-P2. Our ESIM halo and NBODY-S underwent slow evolution and positive accretion at $z = 0$. The NBODY-P and NBODY-P2 experienced fast evolution with M_{200} decreasing at $z = 0$. Slow evolution created a scale-free ρ/σ^3 profile and an NFW density profile. The rapid-collapse scenario created

Plummer-like density profiles and a non-power-law ρ/σ^3 profile.

We conclude that slow vs. fast collapse, which can be induced by changing initial conditions, result in halos either having a scale-free ρ/σ^3, or not. Thus, not all collisionless collapses lead to scale-free ρ/σ^3. We have not quantified what exactly we mean by "fast", or "slow"; this is left for a future work; CDM cosmology naturally leads to a "slow" accretion rate.

We also found that the $\beta(r)$ profile requires three dimensional evolution in order to produce the typical profile (isotropic center, radial outer halo). This then allows for the relationship between β and γ. This conclusion is derived from all three N-body halos having roughly similar $\beta(r)$ and $\beta - \gamma$ relationships, while the ESIM halo is approximately isotropic.

The physical processes available to the three N-body halos, but not ESIM, are the radial orbit instability and more efficient chaotic and/or phase mixing. This suggests that one or both of these is responsible for $\beta(r)$ and hence the $\beta - \gamma$ relation. ROI is known for creating the dramatic shift in anisotropy from the inner to the outer halo (Barnes et al., 2005; Bellovary et al., 2008). As such, it seems likely that the ROI is responsible for the difference. ESIM, which has only the radial spatial dimension available, has no means to undergo ROI or any similar instability, therefore it ends up with an isotropic $\beta(r)$. It is possible that chaotic mixing, which is also accessible to the three N-body halos also plays a role.

6.4 Fin

Dark matter is an elusive quarry. In order to triumph, we must persevere with the current work while creatively finding new ways to observe, simulate, and quantify.

References

van Albada, T. S. 1982 MNRAS, 201, 939

Allen, S. W. 1998 MNRAS, 296, 392

Arad, I., Dekel, A., Klypin, A. 2004 MNRAS, 353, 15

Ascasibar, Y., Yepes, G., Gottlöber, S., Müller, V. 2004 MNRAS, 352, 1109

Austin, C. G., Williams, L. L. R., Barnes, E. I., Babul, A., Dalcanton, J. J. 2005 ApJ, 634, 756

Avila-Reese, V., Firmani, C. & Hernandez, X. 1998, ApJ, 505, 37

Bardeen, J.M., Bond,J.R., Kaiser, N. & Szalay, A.S. 1986, ApJ, 304, 15

Barnes, J., Hut, P., & Goodman, J. 1986, ApJ, 300, 112

Barnes, E.I., Williams, L.L.R., Babul, A. & Dalcanton, J.J. 2005, ApJ, 634, 775

Barnes, E. I., Williams, L. L. R., Babul, A., Dalcanton, J. J. 2006, ApJ, 643, 797

Barnes, E. I., Williams, L. L. R., Babul, A., Dalcanton, J. J. 2007, ApJ, 654, 814

Bellovary, J. M., Dalcanton, J. J., Babul, A., Quinn, T. R., Maas, R. W., Austin, C. G., Williams, L. L. R., & Barnes, E. I. 2008, ApJ, 685, 739

Bennett, C. L., Hlapern, M., Hinshaw, G., Jarosik, N., Kogut, A., Limon, M. 2003, ApJS, 148, 1

Bertschinger, E. 1985, ApJS, 58, 39

Binney, J. 2004, MNRAS, 350, 939

Binney, J. & Tremaine, S. 1987, Galactic Dynamics (Princeton: Princeton University Press)

Birkinshaw, M. 2004, in Carnegie Observatories Astrophysics Series, Vol.3: Clusters of Galaxies: Probes of Cosmological Structure and Galaxy evolution, ed. J. S. Mulchaey, A. Dressler, & A. Oemler (Cambridge: Cambridge University Press), 161

Blandford, R. D., Narayan, R. 1992, ARA&A 30, 311

Bower, R. G., Balogh, M. L. 2004, in Carnegie Observatories Astrophysics Series, Vol.3: Clusters of Galaxies: Probes of Cosmological Structure and Galaxy evolution, ed. J. S. Mulchaey, A. Dressler, & A. Oemler (Cambridge: Cambridge University Press), 325

Bullock, J. S., Dekel, A., Kolatt, T. S., Kravtsov, A. V., Klypin, A. A., Porciani, C., & Primack, J. R. 2001, ApJ, 555, 240

Carilli, C. L., Taylor, G. B. 2002, Annu. Rev. Astron. Astrophys, 40, 319.

Carlberg, R. G., Yee, H. K. C., Ellingson, E., Morris, S., Abraham, R., Grabel, P., Pritchet, C. J., Smecker-Hane, T., Hartwick, F. D. A., Hesser, J. E., Hutchings, J. B., & Oke, J. B. 1997, ApJ, 485, L13

Carlberg, R. G. 2004, in Carnegie Observatories Astrophysics Series, Vol.3: Clusters of Galaxies: Probes of Cosmological Structure and Galaxy evolution, ed. J. S. Mulchaey, A. Dressler, & A. Oemler (Cambridge: Cambridge University Press), 343

http : *//chandra.harvard.edu/*

Cole, S. & Lacey, C. 1996, MNRAS, 281, 716

Couch, W. J., Colless, M. M., & De Propris, R. 2004, in Carnegie Observatories Astrophysics Series, Vol.3: Clusters of Galaxies: Probes of Cosmological Structure and Galaxy evolution, ed. J. S. Mulchaey, A. Dressler, & A. Oemler (Cambridge: Cambridge University Press), 42

Davies, R. L. 2004, in Carnegie Observatories Astrophysics Series, Vol.3: Clusters of Galaxies: Probes of Cosmological Structure and Galaxy evolution, ed. J. S. Mulchaey, A. Dressler, & A. Oemler (Cambridge: Cambridge University Press), 227

De Lucia, G., Kauffman, G., & White, S. D. M. 2004, MNRAS, 349, 1101

Dehnen, W. 2005, preprint, astro-ph/0504246

Dehnen, W. & McLaughlin, D. 2005, MNRAS, 363, 1057

Dejonghe, H., & Merritt, D. 1988, ApJ, 328, 93

Diemand, J., Zemp, M., Moore, B., Stadel, J. & Carollo, M. preprint, astro-ph/0504215

Donahue, M., & Voit, G. M. 2004, in Carnegie Observatories Astrophysics Series, Vol.3: Clusters of Galaxies: Probes of Cosmological Structure and Galaxy evolution, ed. J. S. Mulchaey, A. Dressler, & A. Oemler (Cambridge: Cambridge University Press), 143

Dressler, A. 1980, ApJ 236, 351

Dressler, A. 2004, in Carnegie Observatories Astrophysics Series, Vol.3: Clusters of Galaxies: Probes of Cosmological Structure and Galaxy evolution, ed. J. S. Mulchaey, A. Dressler, & A. Oemler (Cambridge: Cambridge University Press), 206

Dubinski, J. Carlberg, R. G. 1991, ApJ, 378, 496

Edge, A. C. 2004, in Carnegie Observatories Astrophysics Series, Vol.3: Clusters of Galaxies: Probes of Cosmological Structure and Galaxy evolution, ed. J. S. Mulchaey, A. Dressler, & A. Oemler (Cambridge: Cambridge University Press), 58

Evrard, A. E. 2004, in Carnegie Observatories Astrophysics Series, Vol.3: Clusters of Galaxies: Probes of Cosmological Structure and Galaxy evolution, ed. J. S. Mulchaey, A. Dressler, & A. Oemler (Cambridge: Cambridge University Press), 1

Franx, M. 2004, in Carnegie Observatories Astrophysics Series, Vol.3: Clusters of Galaxies: Probes of Cosmological Structure and Galaxy evolution, ed. J. S. Mulchaey, A. Dressler, & A. Oemler (Cambridge: Cambridge University Press), 196

Fukushige, T., & Makino, J. 2001, ApJ, 557, 533

Giovannini, G. & Feretti, L. 2004, Journal of the Korean Astornomical Society, 37, 323

Gladders, M. D. 2004, in Carnegie Observatories Astrophysics Series, Vol.3: Clusters of Galaxies: Probes of Cosmological Structure and Galaxy evolution, ed. J. S. Mulchaey, A. Dressler, & A. Oemler (Cambridge: Cambridge University Press), 89

Gonzalez-Casado, G., Salvador-Sole, E., Manrique, A., Hansen, S. 2007 arXiv:astro-ph/0702368

Gott, J.R. 1975, ApJ, 201, 296

Grego, L., Carlstrom, J. E., Reese, E. D., Holder, G. P., Holzapfel, W. L., Joy, M. K., Mohr, J. J., Patel, S. 2001. Astrophys J. 552, 2

Gunn, J.E. & Gott, J.R. 1972, ApJ, 176, 1

Hallman, E. J. 2004. University of Minnesota. Major: Astrophysics.

Hansen, S. H. 2004, MNRAS, 352, L41

Hansen, S.H., Egli, D., Hollenstein, L. & Salzmann, C. 2005, New Astron., 10, 379

Hansen, S. H. & Moore, B. 2005, New Astronomy, 11, 5, 333

Hansen, S. H., Moore, B. & Stadel, J. 2005. XXIst IAP Colloquium "Mass Profiles and Shapes of Cosmological Structures", Paris 4-9 July 2005, France, Eds: G. Mamon, F. Combes, C. Deffayet, B. Fort, EAS Publications Series

Hansen, S. H., Piffaretti, R. 2008, Astro-ph/0705.4680

Hansen, S. H., Stadel, J. 2006, JCAP, 605, 14

Host, O., Hansen, S. H, 2007, Astro-ph/0704.2909

Huss, A., Jain, B. Steinmetz, M. 1999, ApJ, 517, 64

Kandrup, H. E. 1998. Collisionless relaxation in galactic dynamics and the evolution of long-range order. In Long-Range Correlations in Astrophysical Systems. J. R. Buchler, J. W. Dufty & H. E. Kandrup, Eds. Ann. N. Y. Acad. Sci. 848: 28-47

Kazantzidis, S., Magorrian, J., Moore, B. 2004, ApJ, 601, 37

Lewis, I. J., et al. 2002, MNRAS, 334, 673

Lynden-Bell, D. 1967, MNRAS, 136, 101

MacMillan, J. D., Widrow, L. M., & Henriksen, R. N. 2006, ApJ, 653, 43

Madau, P., Pozzetti, L, Dickinson, M. 1998, ApJ, 498, 106

Manrique, A., Raig, A., Salvador-Sole, E., Sanchis, T., & Solanes, J. M. 2003, Astrophys.J., 593, 26

McNamara, B. R. 2001, in: "Proceedings of XXI Moriond conference: Galaxy Clusters and the High Redshift Universe Observed in X-rays", Edited by D.M. Neumann, F. Durret, & J.T.T. Van.

Merritt, D. 2005. Henry Kandrup's Ideas About Relaxation of Stellar Systems. In: Gottesman, S. T., editor. Annals of the New York Academy of Sciences, Volume 1045, Nonlinear Dynamics in Astronomy and Physics: In Memory of Henry Kandrup. p 3-12.

Merritt, D. & Aguilar, L. A. 1985, MNRAS, 217, 787

Merritt, D., Navarro, J.F., Ludlow, A. & Jenkins, A. preprint, astro-ph/0502515

Mihos, J. C. 2004, in Carnegie Observatories Astrophysics Series, Vol.3: Clusters of Galaxies: Probes of Cosmological Structure and Galaxy evolution, ed. J. S. Mulchaey, A. Dressler, & A. Oemler (Cambridge: Cambridge University Press), 277

Moore, B. 2004, in Carnegie Observatories Astrophysics Series, Vol.3: Clusters of Galaxies: Probes of Cosmological Structure and Galaxy evolution, ed. J. S. Mulchaey, A. Dressler, & A. Oemler (Cambridge: Cambridge University Press), 295

Moore, B., Governato F., Quinn, T., Stadel, J. & Lake, G. 1998, ApJ, 499, L5

Moore, B., Quinn, T., Governato F., Stadel, J. & Lake, G. 1999, MNRAS, 310, 1147

Mulchaey, J. S. 2004, in Carnegie Observatories Astrophysics Series, Vol.3: Clusters of Galaxies: Probes of Cosmological Structure and Galaxy evolution, ed. J. S. Mulchaey, A. Dressler, & A. Oemler (Cambridge: Cambridge University Press), 353

Mushotzky, R. F. 2004, in Carnegie Observatories Astrophysics Series, Vol.3: Clusters of Galaxies: Probes of Cosmological Structure and Galaxy evolution, ed. J. S. Mulchaey, A. Dressler, & A. Oemler (Cambridge: Cambridge University Press), 123

$http://bepposax.gsfc.nasa.gov/$

$http://heasarc.gsfc.nasa.gov/docs/asca/science/science_clusters.html$

Navarro, J. F., Frenk, C. S., White, S., D., M. 1996, ApJ, 462, 563

Navarro, J.F., Frenk, C.S. & White, S.D.M. 1997, ApJ, 490, 493

Navarro, J. F., Hayashi, E., Power, C., Jenkins, A., Frenk, C. S., White, S. D. M., Springel, V., Stadel, J., Quinn, T. R. 2004, MNRAS, 349, 1039

Nichol, R. C. 2004, in Carnegie Observatories Astrophysics Series, Vol.3: Clusters of Galaxies: Probes of Cosmological Structure and Galaxy evolution, ed. J. S. Mulchaey, A. Dressler, & A. Oemler (Cambridge: Cambridge University Press), 24

Ostriker, J. P. 2004, in Carnegie Observatories Astrophysics Series, Vol.3: Clusters of Galaxies: Probes of Cosmological Structure and Galaxy evolution, ed. J. S. Mulchaey, A. Dressler, & A. Oemler (Cambridge: Cambridge University Press), 371

Papovich, C. Moustakas, L. A., et al. 2005, astro-ph/0511289

Poggianti, B. M. 2004, in Carnegie Observatories Astrophysics Series, Vol.3: Clusters of Galaxies: Probes of Cosmological Structure and Galaxy evolution, ed. J. S. Mulchaey, A. Dressler, & A. Oemler (Cambridge: Cambridge University Press), 245

Power, C., Navarro, J.F., Jenkins, A., Frenk, C. S., White, S. D. M., Springel, V. Stadel, J., Quinn, T. 2003, MNRAS, 338, 14

Raisa et al.(2004)

Renzini, A. 2004, in Carnegie Observatories Astrophysics Series, Vol.3: Clusters of Galaxies: Probes of Cosmological Structure and Galaxy evolution, ed. J. S. Mulchaey, A. Dressler, & A. Oemler (Cambridge: Cambridge University Press), 260

Rephaeli, Y. 1995. Annu. Rev. Astron. Astrophys. 33, 541

Rosati, P. 2004, in Carnegie Observatories Astrophysics Series, Vol.3: Clusters of Galaxies: Probes of Cosmological Structure and Galaxy evolution, ed. J. S. Mulchaey, A. Dressler, & A. Oemler (Cambridge: Cambridge University Press), 72

Rosati, P., Borgani, S., Norman, C. 2002, Annu. Rev. Aston. Astophys., 40, 539

Ryden, B. S., Gunn, J. E. 1987, ApJ, 318, 15

Salvador-Sole, E., Manrique, A., Gonzalez-Casado, G., & Hansen, S. H. 2007, Astro-ph/0701134.

$http://sci.esa.int/science-e/www/object/index.cfm?fobjectid=31281\&fbodylongid=797$

$http://www.seds.org/messier/more/vir\_hist.html$

Shapiro, P.R., Iliev, I.T., Martel, H., Ahn, K. & Alvarez, M.A. In Progress in Dark Matter Research, eds. Blain, J.V., (Nova Science Publishers, Inc, 2004)

Shapiro, P. R., Iliev, I. T., Martel, H., Ahn, K., Alvarez, A. 2004, Astro-ph/0409173

Shore, S. 2003, The tapestry of modern astrophysics. John Wiley & Sons, New Jersey.

Smail, I. 2004, in Carnegie Observatories Astrophysics Series, Vol.3: Clusters of Galaxies: Probes of Cosmological Structure and Galaxy evolution, ed. J. S. Mulchaey, A. Dressler, & A. Oemler (Cambridge: Cambridge University Press), 108

Stadel, J. G. 2001, "Cosmological N-body Simulations and Their Analysis," Ph.D. thesis, University of Washington, Pullman.

Syer, D. & White S. D. M. 1998, MNRAS, 293, 337

Taylor, J. E., Babul, A. 2005, Mon. Not. R. Astron. Soc. 364, 515

Taylor, J.E. & Navarro, J.F. 2001, ApJ, 563, 483

Tremaine, S., Richstone, D. O., Byun, Y.-I., Dressler, A., Faber, S. M.,Grillmair, C., Kormendy, J. & Lauer, T. R. 1994, AJ, 107, 634

Treu, T. 2004, in Carnegie Observatories Astrophysics Series, Vol.3: Clusters of Galaxies: Probes of Cosmological Structure and Galaxy evolution, ed. J. S. Mulchaey, A. Dressler, & A. Oemler (Cambridge: Cambridge University Press), 177

van den Bosch, F. C. 2002, MNRAS, 331, 98

van Gorkom, J. H. 2004, in Carnegie Observatories Astrophysics Series, Vol.3: Clusters of Galaxies: Probes of Cosmological Structure and Galaxy evolution, ed. J. S. Mulchaey, A. Dressler, & A. Oemler (Cambridge: Cambridge University Press), 305

Wadsley, J. W., Stadel, J., & Quinn, T. 2004, New Astronomy, 9, 137

Wambsganss, J. 1998, Living Reviews in Relativity, Max-Planck-Institute, Potsdam.

Weinberg, M. D. 1991, ApJ, 368, 66

Williams, L. L. R. 2003, Class notes.

Williams, L.L.R., Austin, C., Barnes, E., Babul, A. & Dalcanton, J.J. Proceedings of "Baryons in Dark Matter Halos". Novigrad, Croatia, 5-9 Oct 2004, eds: R. Dettmar, U. Klein, P. Salucci. Published by SISSA, Proceedings of Science, http://pos.sissa.it, p.20.1

Williams, L.L.R., Babul, A. & Dalcanton, J.J. 2004, ApJ, 604, 18

Wu, X. 2005, Astro-ph/9512110